Thermal Analysis of a Dense Dipole Array for the SKA Mid-Frequency Aperture Array

Corey Smale

Thesis presented in partial fulfilment of the requirements for the degree of
Master of (Electronic) Engineering
in the Faculty of Engineering at Stellenbosch University

Supervisor: Dr Jacki Gilmore

April 2019

Declaration

By submitting this thesis electronically, I declare that the entirety of the work contained therein is my own, original work, that I am the sole author thereof (save to the extent explicitly otherwise stated), that reproduction and publication thereof by Stellenbosch University will not infringe any third party rights and that I have not previously in its entirety or in part submitted it for obtaining any qualification.

Date: April 2019

Abstract

Thermal Analysis of a Dense Dipole Array for the SKA Mid-Frequency Aperture Array

C.J. Smale

Department of Electrical and Electronic Engineering,
University of Stellenbosch,
Private Bag X1, Matieland 7602, South Africa.

Thesis: MEng (Electronic)
April 2019

The Dense Dipole Array (DDA) has been designed as a candidate element for the Mid-Frequency Aperture Array that forms part of the SKA project. This is being developed to realise the aperture array concept in the mid-frequency range, which covers a band form roughly 400 to 1450 Mhz. The MFAA is highly anticipated with its incredible survey speed and is intended to be deployed in the Karoo of South Africa. The semi-desert region provides adequate spacing with the perfect radio quiet backdrop, but exposes the arrays to harsh climates. As the system noise temperature is dominated by the receiver noise in this frequency band, the environmental temperature can greatly influence the quality of received signals. This creates a challenge as the arrays will have to operate at ambient temperature as forced cooling cannot be implemented within reasonable cost and complexity, due to the large number of antennas.

A thermal analysis is performed on the DDA to determine its suitability in the climate of the Karoo. This is done by developing and testing a finite element model that incorporates computational fluid dynamics to simulate the resulting temperatures of the DDA when in the extreme conditions of the Karoo. The primary component limiting the operating temperature of the DDA and the main consideration during the analysis is the integrated low-noise amplifier. Two operating parameters of the LNA, being the maximum temperature and change in temperature are evaluated to ensure the desired performance of the DDA is achieved and will therefore meet the requirements of the MFAA.

It is found that a thermal solution is necessary to bring the DDA within acceptable operating conditions. An open enclosure is designed and optimised for this purpose that utilises a polypropylene cover to mitigate the effects of the environment while considering the impact on the electromagnetic performance. Further simulations are then performed to assess the degradation of antenna performance. In conclusion, the enclosure successfully reduces the operating parameters to an acceptable level, and the cover does have a minor impact on the electromagnetic performance although with foreseeable benefits in stabilization with further optimisation.

Uittreksel

Thermal Analysis of a Dense Dipole Array for the SKA Mid-Frequency Aperture Array

C.J. Smale

Department of Electrical and Electronic Engineering,
University of Stellenbosch,
Private Bag X1, Matieland 7602, South Africa.

Thesis: MEng (Electronic)
April 2019

Die Digte Dipool Samestelling (DDA) is ontwerp as 'n kandidaatelement vir die Midfrekwensie Apertuur Samestelling (MFAA) van die SKA. Dit word ontwikkel om die apertuur samestelling konsep, wat 'n frekwensiebereik van ongeveer 400 - 1450 MHz dek, te realiseer. Die MFAA word verwag om baie hoë opname spoed te kan lewer en is bedoel om die Karoo van Suid-Afrika gebou te word. Die semi-woestyn gebied verskaf genoeg ruimte met 'n stil radio agtergrond, maar stel die samestelling bloot aan die harde woestynklimaat. Aangesien die stelsel se sensitiwiteit gedomineer word deur die ontvanger se ruistemperatuur in hierdie frekwensieband, kan die omgewingstemperatuur 'n groot invloed hê op die kwaliteit van die seine wat ontvang word. As gevolg van die groot hoeveelheid antennas word 'n uitdaging dus geskep aangesien die antennas by omgewingstemperatuur moet werk omdat dit nie prakties of koste-effektief is om die stelsel aktief te verkoel nie.

'n Termiese analise word dus uitgevoer om die geskiktheid van die DDA in die woestynklimaat te evalueer. Dit word vermag deur 'n eindige-element model wat berekeningsvloeistofdinamika gebruik om die termperature wat die DDA aan blootgestel sal word in die Karoo te ontwikkel en te toets. Die primêre component wat die toelaatbare werkstemperatuur van die DDA beperk, en dus die hoofoorweging van die analise is, is die geïntegreerde laeruis versterker (LNA). Twee werkstemperatuurkondisies van die LNA word ondersoek om die prestasie van die DDA te evalueer en om te bevestig of die vereistes van die MFAA nagekom word - die maksimum temperatuur, en die tempo van verandering in temperatuur.

Daar is gevind dat 'n toepaslike termiese oplossing nodig is om die DDA binne aanvaarbare werkskondisies te hou. 'n Oop omhulsel is ontwerp en geoptimeer hiervoor, en maak gebruik van 'n polipropileen deksel om die effek van die omgewing te versag. Die effek van die deksel om die elektromagnetiese prestasie is ook ge-evalueer om moontlike negatiewe effekte te identifiseer. Resulate toon dat die omhulsel die werkstemperatuur suksesvol verlaag het na aanvaarbare vlakke terwyl die effek op die samestelling se elektromagnetiese prestasie minimal was of selfs moontlik kan lei to verbetering in die stabiliteit van die impedansieaanpassing met verder optimering van die ontwerp van die samestelling.

Acknowledgements

The author wishes to acknowledge the following people and institutions for their various contributions towards the completion of this work:

- My supervisor, Dr Jacki Gilmore, for her knowledge and guidance throughout this project and for giving me this opportunity.
- My parents, for their continuous love and support and always believing in me.
- My roommate, Shane van Heerden, for his encouragement and motivating attitude.
- Fahmi Mokhupuki, for his few words of wisdom and making the lab more than just a workplace.
- Dr Danie Ludick, for his understanding and providing of the measurement equipment.
- Nelis Wilke, for his assistance and support during this project.
- This research was supported by the South African Radio Astronomy Observatory, which is a facility of the National Research Foundation, an agency of the Department of Science and Technology.

Table of Contents

Nomenclature

Constants

$c_o = 299792458\ m/s$
$\sigma = 5.67 \times 10^{-8}\ W/m^2 \cdot K^4$
$h = 6.0626 \times 10^{-34}\ J \cdot s$
$k = 1.380 \times 10^{-23}\ J/K$
$g = 9.8066\ m/s^2$

Acronyms

AA: Aperture Array
ABS: Acrylonitrile Butadiene Styrene
ADC: Analog to Digital Converter
AIP: Advanced Instrumentation Programme
CFD: Computational Fluid Dynamics
DDA: Dense Dipole Array
EM: Electromagnetic
FEA: Finite Element Analysis
FEM: Finite Element Model
FoV: Field of View
HBA: High Band Antenna
LBA: Low Band Antenna
LNA: Low-Noise Amplifier
MeerKat: Meer-Karoo Array Telescope
MFAA: Mid-Frequency Aperture Array
MM: Mixed Mode
NF: Noise Figure
ORA: Octagonal Ring Antenna
PCB: Printed Circuit Board
PDE: Partial Differential Equation
PP: Polypropylene
PVC: Polyvinyl Chloride

RF: Radio Frequency

RFI: Radio Frequency Interference

RTC: Real-Time Clock

SKA: Square Kilometre Array

SNR: Signal to Noise Ratio

List of Figures

List of Tables

CHAPTER 1

Introduction

Contents

1.1 The Square Kilometre Array Project

Science and technology has taken mankind's knowledge and understanding of the world and that of its surroundings to incredible heights. With the past few decades of continuous research and the scientific discoveries that followed, the once blurry picture of how the universe works has become a lot clearer. Even so, there is still a large distance between what is known and what is still to be determined. The Square Kilometre Array (SKA) is proposed to bridge this gap and bring mankind to a closer understanding of the universe than anything before it.

The Square Kilometre Array is a collaborative effort between countries from all over the world to develop the next generation radio telescope. The project's shear scale pushes the boundary in both engineering and research to deliver what will be one of the greatest technologies in scientific history. The SKA will provide astronomers with the capability of surveying the skies in unprecedented detail at a much faster rate than what is currently possible with existing systems. To achieve this, the SKA will comprise thousands of radio telescopes and upto a million antennas that will eventually cover over a million square metres of collecting area [1].

The project has been divided into two phases of development and is being built in two separate locations in the Southern Hemisphere. Both South Africa's Karoo region and Western Australia's Murchison Shire were chosen as co-hosting locations for the SKA as they met the site selection criteria. This primarily consisted of providing minimal radio frequency interference, low development and maintenance costs and having long term sustainability as a radio quiet zone [2], [3]. The first phase of development for the project will constitute towards 10% of the final telescope and will involve testing the full system in a "proof of concept" manner. The second phase will complete the telescope arrays at both sites with the addition of many more stations and initiate construction of the mid and high frequency elements of the array [4].

1.2 The Mid-Frequency Aperture Array

The SKA is comprised of a combination of multiple elements with separate objectives to achieve the full operation of the final telescope. The Mid-Frequency Aperture Array (MFAA) forms part of the SKA Advanced Instrumentation Programme (AIP) to develop the technology required to realise the aperture array concept in the mid-frequency range. This range is intended to cover a frequency band from roughly 400 to 1450 MHz [5]. Many of the science cases of the SKA require very high sensitivities in the appropriate frequency range with the ability to detect very small variations in the observed signal. An aperture array concept has therefore been chosen for the mid-frequency range as it is believed that it can better achieve the SKA's science requirements over other antennas [2], [6], [7].

The MFAA will consist of a large quantity of $1m^2$ tiles each with a repeating pattern of antennas including Low-Noise Amplifiers (LNA's) and receivers. The signals from each tile will be combined to form a radio telescope with a collecting area of $500m^2$. Advantages of aperture arrays over conventional reflector antennas are the wide Field of View (FoV), electronic beam steering and the ability to observe with a large number of beams simultaneously [8], [9]. With a large FoV and high flexibility, the MFAA will enable astronomers to perform high speed surveys for pulsars and other radio transient events and possibly even measure the effects of dark energy on the universe [1], [10].

To meet the scheduled deployment of the MFAA in the second phase of the project, multiple design concepts are currently being developed. The Karoo has been chosen as the location for the MFAA as it provides adequate spacing and little radio interference.

1.3 Problem Description

The Dense Dipole Array (DDA) has been designed as a candidate element for the SKA Mid-Frequency Aperture Array. The primary research aim of this project is to determine the suitability of the DDA tile in the climate of the Karoo through thermal analysis; and develop an appropriate thermal solution if necessary to maintain the DDA within an acceptable operating temperature range. The Karoo provides the perfect radio quiet backdrop for the MFAA with the minimal terrestrial RFI sources, but is exposed to harsh desert temperatures. This creates a challenge as the arrays will have to operate at ambient temperature as forced cooling cannot be implemented within reasonable cost and complexity, due to the amount of antennas to be deployed [9]. As a result, this can negatively influence the sensitivity of the array as it is determined by the ratio of effective area A_{eff} and system noise temperature T_{sys} as follows [5]

$$Sensitivity = \frac{A_{eff}}{T_{sys}} \tag{1.1}$$

The large collecting area is the main reason for the aperture array's greatly enhanced sensitivity, but requires that the system noise temperature remains at an acceptable level. This is important as the sensitivity of the array also has an effect on other performance characteristics such as survey speed [11], [12]. The parameters that have the greatest influence on system temperature change as a function of frequency with the receiver noise temperature having the biggest contribution in the mid-frequency range [5], [13]. It is therefore imperative that this is kept to a minimum to achieve the best performance of the DDA.

1.4 Scope and Objectives

The following objectives will be pursued in this thesis:

I To *conduct* a thorough survey of the literature related to:

(a) thermal analysis methodology and the types of heat transfer,

(b) the critical parameters of the DDA susceptible to thermal influence,

(c) methods of thermal protection.

II To *develop* a thermal model of the Dense Dipole Array capable of accurately predicting the temperatures experienced under specified climate conditions.

III To *verify* the accuracy of the thermal model developed in Objective II by conducting an experiment, to compare the temperatures recorded on the DDA prototype (in the climate conditions of Stellenbosch), to those determined from the thermal model under the same conditions.

IV To *determine* the most extreme hot and cold environments the DDA might experience during operation in the Karoo.

V To *perform* a finite element analysis using the thermal model developed in Objective II to determine the thermal patterns experienced under the extreme cases from Objective IV.

VI To *analyse* the results obtained from the previous objective and determine if a thermal solution will be necessary for the successful operation of the DDA in the Karoo.

VII To *design* an appropriate thermal solution to maintain the DDA within an acceptable temperature range throughout operation.

VIII To *evaluate* the effectiveness of the thermal solution designed in Objective VII through thermal analysis and determine if it successfully brings the operating temperatures of the DDA to within an acceptable range.

IX To *assess* the effect the thermal solution might have on the electromagnetic performance of the DDA and analyse any negative impacts.

X To *recommend* sensible follow-up work related to this project which may be pursued in future.

1.5 Thesis Organisation

Apart from this introductory chapter this thesis consists of a further six chapters. Chapter 2 contains a literature review of material which is of relevance to this project and provides an understanding of the methodologies used throughout. Chapter 3 is devoted to the establishment of an accurate thermal model to predict temperature results of the DDA in the Karoo. The focus in Chapter 4 falls on creating the most extreme cases the DDA might experience during operation and determining the corresponding temperature profiles. The design procedure and simulated results of an enclosure are documented in Chapter 5. The effect the enclosure will have on the electromagnetic performance of the DDA is assessed in Chapter 6. Finally, the project closes in Chapter 7 with a summary and appraisal of what this thesis has contributed followed by recommendations of work related to this project that may be pursued in the future.

CHAPTER 2

Literature Review

Contents

As stated in the previous chapter, maintaining the MFAA within acceptable operating temperatures without forced cooling whilst still achieving the set out performance requirements creates a significant challenge. This chapter is devoted to a thorough review of the literature related to the DDA and the corresponding thermal management. In §2.1, an overview of aperture arrays is provided followed by a description of the DDA in §2.2. The focus shifts in §2.3 to thermal analysis methodology with the forms of heat transfer and proposed approach of analysis. The effects of temperature on noise is then discussed in §2.4. §2.5 is devoted to the components influenced by temperature and the corresponding affects. The chapter closes in §2.6 with a discussion of a similar case of thermal management to this project, and a conclusion in §2.7 of the material included in this chapter.

2.1 Aperture Arrays

An aperture array (AA) is a telescope that utilises many phased array stations each with a large number of small antenna elements coupled to receiver systems to detect radio signals. The

receiver systems incorporate a Low-Noise Amplifier (LNA) and filter to extract and amplify the desired signal; thereafter the signals from groups of elements are beamformed using either analogue or digital techniques or a combination of both [5], [14]. The process of beamforming entails aligning the arrival time of signals from individual elements with appropriate time delays to form a coherent beam in a specified direction[15]. A *station beam* is generated when each of the beamformed signals from the many tiles comprising an AA station are combined with further beamforming.

AA's have the characteristics necessary to achieve excellent dynamic range due to the high level of control over each receiver element. Since the array is comprised of no moving parts, altering the focus of the antennae is reduced to a matter of seconds as this is primarily dependent on processing speed. This makes the technology extremely suitable for rapid follow-up of transient events [16]. By simultaneously creating multiple independent beams using different sets of time delays and configuring each beam to analyse specific portions of the sky an enormous total FoV can be attained. AA's are also inherently flexible as it is possible to adjust survey speed as a function of frequency by varying the number of beams across the desired bandwidth [15].

In Equation 1.1, it is shown that the sensitivity of a telescope is dependent on the effective area and system noise temperature, which change as a function of frequency. As a result different design concepts are favoured for the different frequency bands of the SKA [5]. For the low-frequency range, the sparse array has been utilised by both the LOFAR Low Band (LBA) and High Band Antenna (HBA) as this configuration can provide twenty times the effective aperture at low frequencies [13], [17]. In the mid-frequency range, above about 400 MHz, the sky noise becomes relatively low and constant; and in [17], it is explained that when the element spacing of an array across a frequency band is of order $\lambda_{min}/2$, an effectively fixed aperture area is attained. This implies that a dense configuration will provide the best conditions for the lowest possible front-end noise to achieve a high and near constant sensitivity over the mid-frequency range. Although this does require that the receiver noise is maintained within an acceptable level as it dominates the system noise temperature and is highly sensitive to the physical operating temperature. In Figure 2.1 an artists conception of the MFAA can be seen to grasp an idea of the size of the stations and the dense arrangement of the area.

FIGURE 2.1: *Artist conception of the SKA dense Mid-Frequency Aperture Array [18].*

2.2 The Dense Dipole Array

A dense AA compared to other AA topologies has elements spaced a distance less than $\lambda_{min}/2$ apart. This provides great performance benefits as the incoming electromagnetic (EM) signal for each polarization is fully sampled [17]. By digitizing each polarization for every element the dense AA can be fully calibrated spatially for phase, gain and polarization as a function of frequency providing an advantage over other topologies [15]. The technology also has relatively low cost fabrication as it is composed of a large number of small components that can be shipped and assembled on site with little difficulty. The SKA built using dense aperture array technology will be the most rapid astronomical survey machine in the world [14].

As mentioned in the previous chapter, §1.2, multiple aperture array topologies are currently being researched and developed as candidates for the MFAA. These include the *Vivaldi Array* [7] and the *Octagonal Ring Antenna* (ORA) [19]. Recently another dense AA approach has been realised with the design of a dual-polarised Dense Dipole Array. The design is a planar structure consisting of an array element layer of overlapping dipoles placed above a ground plane with specially designed common-mode filter feed-boards [5]. This takes inspiration from work by Munk and is a version of Wheeler's current sheet array that improves the overall bandwidth of the array by exploiting the capacitive coupling between elements and their close proximity. The specially designed feed structure contributes to the improved bandwidth by suppressing the EM-fields induced by the common-mode currents while still allowing the EM-fields induced by the differential-mode currents to propagate [20]. A strength of the DDA is its planar structure as this will aid in mass production, maintenance and deployment while the performance is still comparable to that of other MFAA front-end concepts.

Multiple prototypes of the DDA have been manufactured for performance testing although each of which follow the same structural design shown in the computer rendered images in Figures 2.2, 2.3 and 2.4. This design is what will be modelled in the thermal simulation and is comprised of four main components. The top plane of the array is the antenna layer and is made up of sixteen square tiles of an FR4 substrate with a thickness of 0.8 mm and a combined area of 1.08 m^2. These tiles contain the dipoles of the DDA with the array elements corresponding to each polarisation printed on either side. The antenna layer rests above an aluminium ground plane of the same area with a gap of 75 mm that provides the base support of the array. The previously mentioned specially designed connecting feed is achieved with multiple feed-boards of an *RO4003C* material placed in a specific configuration between the two planes. Each of the feed-boards is soldered to two SMA connectors that protrude through drilled holes in the ground plane. Lastly, structural integrity is attained with plastic support standoffs at each corner of a tile.

2.3 Thermal Analysis Methodology

Thermal analysis is the process of measuring the flow of thermal energy and determining the effects of temperature in any given system. This is often performed in product development and testing by means of a thermal simulation to validate desired performance in the intended environment. The various techniques of thermal simulation analysis can be executed to find temperature distribution, temperature gradient, and heat flowing in a model as well as heat exchanged between a model and its surroundings. To perform an accurate thermal analysis a proper understanding of heat transfer is required such that the appropriate thermal properties and boundary conditions are applied.

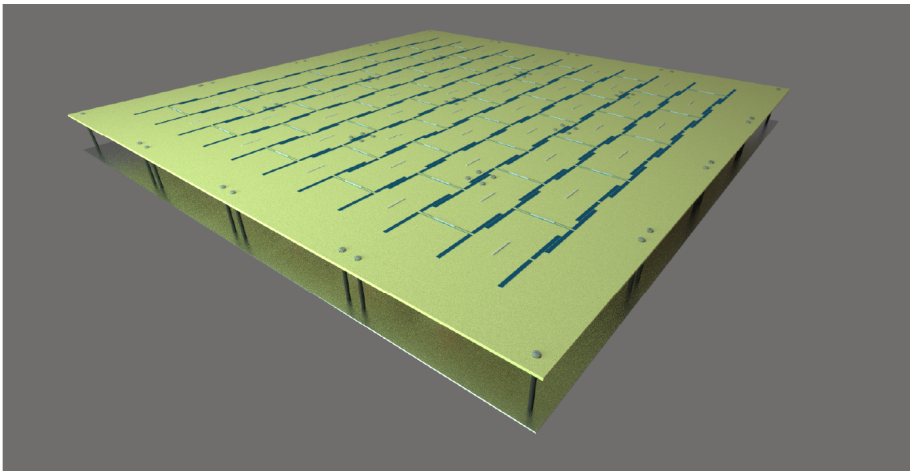

FIGURE 2.2: *The top view of the computer rendered DDA [21].*

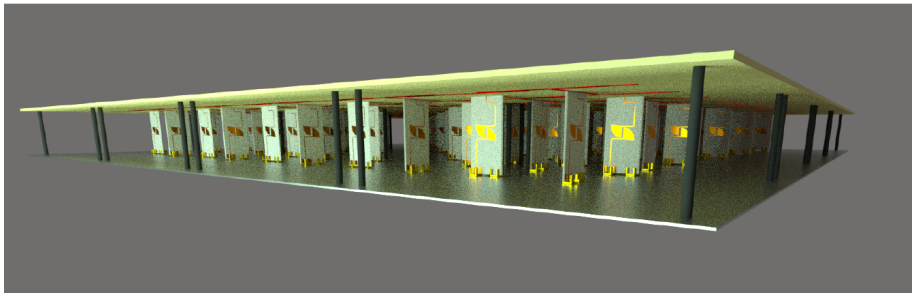

FIGURE 2.3: *The side view of the computer rendered DDA [21].*

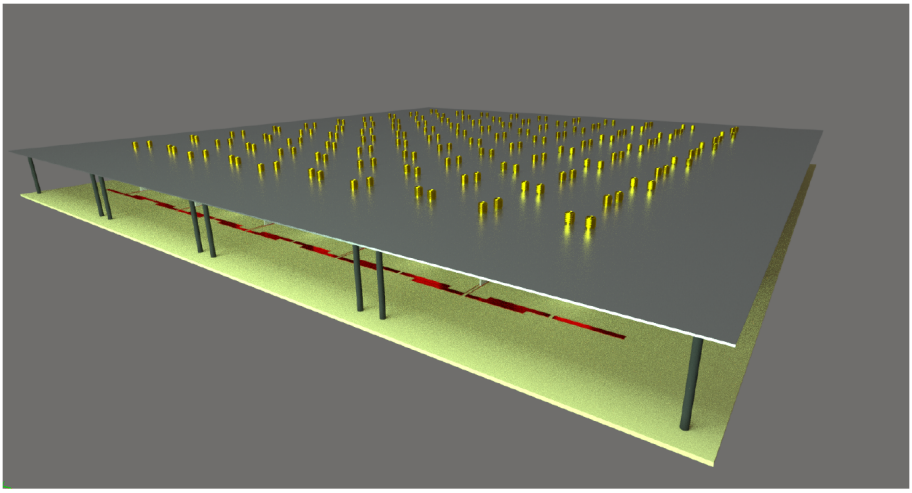

FIGURE 2.4: *The bottom view of the computer rendered DDA [21].*

2.3.1 Heat Transfer

Heat transfer describes the flow of thermal energy in a medium or between media due to a spatial temperature difference. This occurs when a system is in a state of non-thermal equilibrium. The laws of thermodynamics lay the framework for heat transfer and require that the rate of energy transferred into a system be equal to the rate of increase in energy of that system. A temperature gradient always results in heat transfer in the direction of decreasing temperature with the rate of which proportional to the gradient [22], [23]. There are three mechanisms of heat transfer namely conduction, convection and radiation.

Conduction transfers heat via direct molecular collision, increasing the kinetic energy of the less energetic molecules with the adjacent more energetic ones. Conduction is the most common form of heat transfer and occurs via physical contact. The rate of heat transfer through conduction is governed by *Fourier's Law* [24]

$$\dot{Q}_{cond} = -kA\frac{dT}{dx} \tag{2.1}$$

where k is the thermal conductivity of the material (which is a measure of the ability of a material to conduct heat) in $(W/m \cdot K)$, A is the area perpendicular to the heat flow in (m^2), and dT/dx in (K/m) is the temperature gradient.

Convection is the heat transfer from one material to another via a fluid and is dependent on the nature of the flow. Forced convection refers to flow caused by external means such as atmospheric winds or a pump. In contrast, for natural convection any flow motion is induced by buoyancy forces, which are due to density differences caused by temperature variations in the fluid. The rate of convective heat transfer is represented by *Newton's law of cooling* [22], [24] as follows

$$\dot{Q}_{conv} = hA_s(T_s - T_\infty) \tag{2.2}$$

with h the heat transfer coefficient (a.k.a. film conductance) in $(W/m^2 \cdot K)$, A_s is the surface area between the interacting elements, T_s the surface temperature and T_∞ the fluid temperature.

Heat transfer that occurs without any medium and through electromagnetic waves is radiation. The energy in a wave can be transferred through, absorbed by, or reflected from a material based on its properties. The movement of charged protons and electrons results in the emission of electromagnetic radiation, the rate of which is based on *Stefan-Boltzmann's law* [22]–[24] where ε is the emissivity of the surface and σ = *Stefan-Boltzmann constant*.

$$\dot{Q}_{rad} = \epsilon\sigma A_s(T_s^4 - T_\infty^4) \tag{2.3}$$

2.3.2 Finite Element Analysis

In a simulation driven design it is often not feasible to perform a thermal analysis through experimentation to gather measured data. Rather thermal analysis through simulation is used as it can still provide a very close approximation of temperature distribution while greatly simplifying the approach. Good thermal assessments require a combination of analytical calculations using thermal specifications, empirical analysis and thermal modeling. This can accurately be done with the use of thermal analysis software such as *Midas NFX* that utilises numerical methods to solve complex heat transfer problems [25]. Partial differential equations (PDEs) provide the mathematical structure with which finite element software operates. One of the primary methods applied in solving for coupled non-linear PDEs that describe a thermal network is the finite element method (FEM) [26].

A thermal finite element model is capable of modeling conduction in solid elements with specified thermal conductivities and can approximate convection and radiation heat transfer from boundary conditions based on empirical correlations [27]. The core concept of the FEM solves a complex problem by dividing it into smaller easier to solve sections with approximations from boundary conditions and then combining the individual results to get the final answer. The boundary conditions applied in a thermal model simulation are the symmetry and fixed temperature conditions as well as the heat flux sources. A symmetry boundary condition implies that

there is an inward boundary heat flux of zero and is equivalent to an adiabatic boundary condition. A fixed temperature condition specifies a desired temperature on the boundary. Lastly, a heat flux source describes the intensity of thermal energy transferred to a specific area [23], [28]. The finite element analysis (FEA) provides an accurate approximation of a thermal model and will be used in the general application of this thesis

2.4 Radio Noise

In radio frequency (RF) systems, the received waveform is usually categorized into two parts. The first being the desired part containing the information, known as the signal and the second, the extraneous or undesired part called noise. The noise of a signal varies greatly with random fluctuations as it is produced by several different effects and as a result cannot be predicted. The quality of a received signal directly depends on the level of noise present in the system. High amounts of noise can greatly decrease the efficiency of an RF system degrading the system performance to the point where the received signal cannot be distinguished from the noise. This is especially prominent when detecting weak signals, which is the case for the SKA and is therefore an extremely important factor considered throughout design. It has been discovered through multiple studies that the source of noise in the system can be either internal or external or in most cases a combination of both. A thermal body's radiation in the field of view of an antenna may lead to extrinsic noise experienced by the system, the same can be said for terrestrial disturbances in the environment. Intrinsic noise is introduced by the vibrations of electrons in a material as well as the fluctuations in current [29]–[31], with the following different types:

- **Thermal noise** - Is generated from the thermal agitation of bound charges inside an electrical conductor.
- **Shot noise** - Is the random fluctuations of electrical current caused by the discrete or quantized nature of charge carriers or photons comprising the signal.
- **Flicker noise** - Is an electronic noise that has a power spectral density of $1/f$ and is therefore highly prominent in low frequency systems.

The noise level in RF systems is proportional to the gain and bandwidth of the system as well as the receiver temperature. Thermal noise is present in all circuitry and is mitigated with proper thermal management and is therefore a focus of this thesis. Furthermore, other noise processes including both intrinsic and extrinsic can be modelled as thermal noise.

2.4.1 Thermal Noise

If an electrical conductor operates at a temperature above absolute zero kelvin the charge carriers within the conductor experience random motion. This leads to a temporary agglomeration of carriers at either end of the conductor inducing a rapidly fluctuating potential difference (V_{AB}) between each end (see Figure 2.5(a) and (b)). This phenomenon was initially observed by Johnson in 1928 and was later mathematically described by Nyquist and is the reason why thermal noise is also referred to as Johnson or Nyquist noise [32]–[34].

Consider a simple resistor circuit operating at temperature $T(K)$ as shown in Figure 2.6(a). As previously mentioned if the temperature of the resistor is above absolute zero kelvin, the electrons

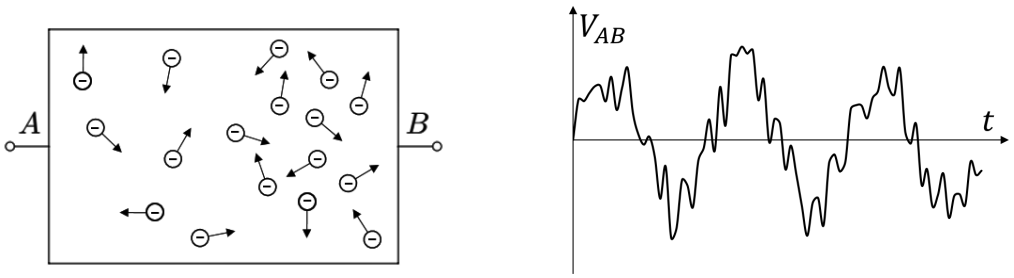

(a) (b)

FIGURE 2.5: *(a) Spontaneous clustering of electrons in a conductor at one end, (b) Thermal noise voltage versus time.*

become thermally agitated and cause an instantaneous noise voltage. This noisy resistor can be modeled with its Thevenin equivalent by means of an identical noiseless resistor and a noise voltage source ($\overline{v_n}$) as shown in Figure 2.6(b). This thermal noise voltage can be mathematically described as follows [32]

$$\overline{v_n} = \sqrt{\frac{4hf_0BR}{e^{\frac{hf_0}{kT}} - 1}} \tag{2.4}$$

where h = *Planck's constant* ($6.0626 \times 10^{-34}\ J \cdot s$), k = *Boltzmann's constant* ($1.380 \times 10^{-23}\ J/K$), f_0 is the centre frequency and B is the bandwidth in Hz, R is the resistance in Ω and T is the temperature in K. A simplification of Equation 2.4 can be made with the *Rayleigh-Jeans approximation* ($e^{\frac{hf}{kT}} - 1 \approx \frac{hf}{kT}$) for microwave frequencies [35], from which it follows that

$$\overline{v_n} = \sqrt{4kTBR} \tag{2.5}$$

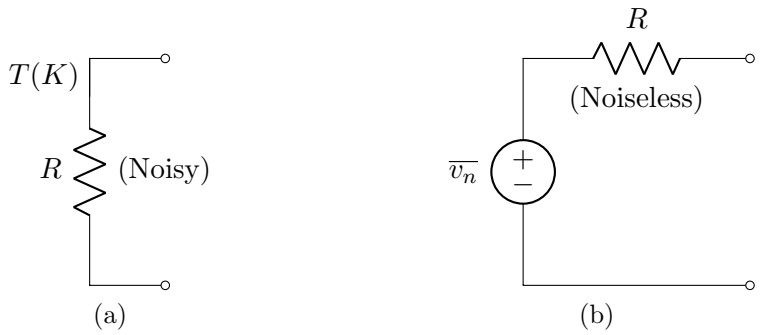

(a) (b)

FIGURE 2.6: *(a) Noisy resistor at temperature T, (b) Thevenin equivalent circuit of noisy resistor.*

It is often also useful to express the thermal noise in terms of a power level. If a noiseless load is connected to the circuit in Figure 2.6(b), the available noise power measured can be written as [32]

$$N = \frac{\overline{v_n}^2}{4R} = kTB \tag{2.6}$$

From Equation (2.5) it is important to note that the thermal noise of a system is directly proportional to the temperature and bandwidth of that system. The MFAA is set to operate at a very wide bandwidth and it is therefore necessary to ensure the system temperature is kept to a minimum for the best possible received signal.

2.4.2 Sky Noise

When an antenna is pointed at a body with thermal radiation, that body acts as a noise source with an associated noise temperature [32]. These thermal bodies include the sun, the earth, the moon, and also the atmosphere. The intensity of thermal radiation seen in the FoV of the receiver is reduced depending on the translucency of the body. Although, even if the atmosphere were perfectly transparent with no bright stars or galaxies in the FoV, the receiver would still pick up noise from cosmic background radiation. The sky noise temperature is a measure of the amount of cosmic noise power that is received from outer space as well as the noise caused by atmospheric attenuation [36].

There are two causes of radio signal attenuation that are introduced from the atmosphere and these include absorption by atmospheric gases and absorption by rain [32]. The thermal process of absorption where the absorbed radio wave is transformed into heat, results in noise being introduced to the signal as it passes through the media. The level of noise contribution from the atmosphere depends on the zenith angle, which describes the angle between the pointing direction of the antenna and the zenith (straight up). Pointed towards the zenith the antenna signal will experience the smallest possible thickness of atmosphere. When angled towards the horizon, the antenna signal has to pass through a much longer portion of atmosphere; greatly increasing the occurrence of absorption leading to an increase in sky noise.

In addition to signal attenuation there is another noise source introduced when pointing the antenna skyward towards the rest of the galaxy. This noise is known as galaxy noise and decreases with increasing frequency. Hence, the reason why sky noise dominates the low frequency band. When considering sky noise, the two major sources are galaxy noise and atmospheric noise. Similar to thermal noise, these noise processes can be modelled with an equivalent noise temperature that represents the noise power available at the terminals of the antenna. This equivalent noise temperature is plotted in Figure 2.7, as a function of frequency and for a variety of elevation angles.

From the figure, the microwave window can be seen where the noise temperature is the lowest, between about 1-10 GHz. This frequency band is highly used in satelite and deep-space communication [32]. For each angle of elevation it can be seen how the noise contribution decreases due to the shorter effective signal path length through the atmosphere. The effect from rain with atmospheric attenuation is also playing a role as it narrows the microwave window. Lastly, the noise temperature drastically increases beyond 10 Ghz on account of the higher rates of absorption at higher frequencies. As the mid-frequency range operates close to within the microwave window the sky noise has little impact making the intrinsic noise the limiting factor of sensitivity of the system.

2.4.3 Equivalent Noise Temperature

With the high impact noise can potentially have on a system, it is important to determine the appropriate noise limits and the conditions necessary to remain within said limits such that the desired signal can be attained. A method of measuring the noise of a system is therefore

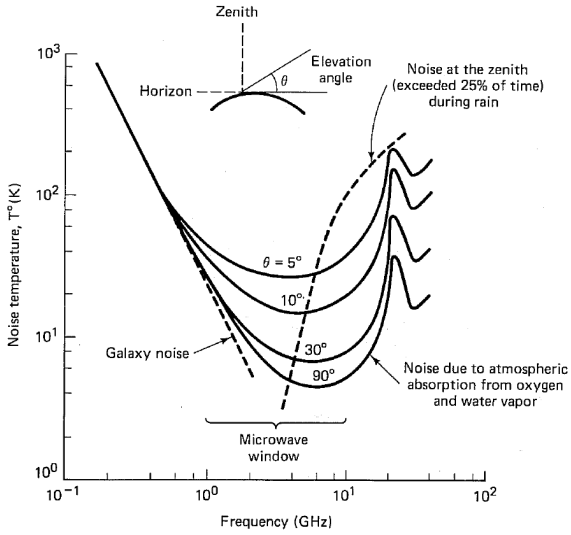

FIGURE 2.7: *Noise temperature from sky noise with frequency [36].*

required and is characterised by a quantity called "the system noise temperature" and has the units of absolute temperature (Kelvin). Noise temperature is not the physical temperature of the component but rather a theoretical construct defined as a thermal source equivalent to the available noise power spectral density as the actual source. Although the noise temperature does not directly correspond with physical temperature there may be a dependence on temperature as is the case with thermal noise [37].

In practise, the amount of noise power known from an arbitrary white noise source can be modelled using an equivalent situation. This involves the rearrangement of Equation 2.6, where the noise generated by a resistor is represented by an equivalent temperature T_e and N is the actual noise power generated by the noise source as follows [31], [32]

$$T_e = \frac{N}{kB} \tag{2.7}$$

As previously discussed there are multiple causes of random noise in electrical devices and noise characterisation usually refers to the combined effect from all noise sources in the system. When considering an isolated receiver that is not connected to an antenna the noise measured at the receiver output is solely due to the noise generated in the receiver itself. This noise is referred to as the receiver input and the input power is associated with a noise temperature that is called the receiver system temperature T_{rec}. This noise temperature is what sets the limiting sensitivity of the receiver with the lower the temperature the better the overall performance. If the receiver is connected to an antenna that is pointed to the sky, then the noise at the output of the receiver is a combination of the noise generated within the receiver itself, and the sky noise collected by the antenna. Similarly to intrinsic noise sources, the noise from the atmosphere, sky and the antenna losses can be modelled as a resistor at the input of the receiver with an equivalent antenna temperature T_{sky}. The total equivalent temperature used to describe the combining noise powers of the system is the summation of the two grouped noise sources as follows

$$T_{sys} = T_{sky} + T_{rec} \tag{2.8}$$

Note that the subject of interest in the field of view can greatly influence the necessary receiver. This is because if the antenna is pointed to a region of the sky near the galactic centre with a potentially very high sky noise, even the highest quality receiver will have a minimal impact on improving sensitivity. As the noise will be dominated by the background sky noise, not the receiver noise. The level of acceptable noise in a system is determined from the maximum point where the desired information can still be effectively differentiated from the interfering noise. A strong signal can be retrieved from a system with a high level of noise as long as the quality of the radio link is of an acceptable standard. This is consequently quantified by the ratio of the signal power to noise power with the term signal-to-noise ratio (SNR)

$$SNR = \frac{\text{average signal power}}{\text{average noise power}} \tag{2.9}$$

The SNR is expressed in decibels since it is a ratio (SNRdB = 10log SNR) and when determining the output SNR of an RF system it is important to consider the effect of the receiver chain as each of the components can add intrinsic noise. This is further explained by the fact that an LNA serves as the first-stage amplification in the analogue receiver, and is designed to add very little noise to the amplified signal. Hence, the SNR at the output of the amplifier is reduced due to the amplifier noise added to the signal. The ratio of the input SNR to the output SNR is called the noise factor (NF) [30]

$$NF = \frac{S_i/N_i}{S_o/N_o} \tag{2.10}$$

where S_i and N_i are the input signal and noise powers, and S_o and N_o are the output signal and noise powers. The NF is always greater than 1 as the input SNR is always higher than the output SNR.

$$NF \geq 1 \tag{2.11}$$

The NF can also be expressed in dB and for a noiseless network, NF = 1 or NF = 0 dB. Very low noise figures can be achieved when the amplifier is cooled to a temperature below ambient.

2.5 Temperature Dependent Properties

Many materials and products have temperature-dependent characteristics which makes analysing the impact of heat and ensuring thermal management a crucial step in product development. This involves understanding the temperature limits of a component and the effects temperature can potentially induce when operating outside of acceptable conditions. Temperature can directly influence the performance reliability and in most cases reduce the life-time of a product when exposed to harsh conditions [38]. It is therefore necessary that the proper thermal management is achieved for the intended environment. The Dense Dipole Array is comprised of various components subject to temperature induced effects and are elaborated on below.

2.5.1 The Low-Noise Amplifier

The operating temperature of electronic components is almost always an important factor to consider when analysing performance as high temperatures can lead to increased thermal noise,

overheating and even premature failure. The DDA is accompanied with multiple electronic components in the receiver chain and for operation. These include LNAs, filters, beam former and beam combiner electronics, control electronics and lastly power supplies. The primary component limiting the operating temperature of the DDA and the main consideration during thermal analysis is the LNA. The role of the LNA is to improve the signal level without adding significant noise and distortion [29].

As the first and most sensitive element of the receiver chain, the LNA influences the SNR as well as the linearity of the receiver. It is the most important subsystem from a noise perspective and is consequently designed specifically for optimum noise performance. In order to mitigate noise contribution to the receiver due to noise coupling the performance is optimised through *noise matching* and involves matching the amplifiers to the active reflection coefficients of the array [39]. The physical temperature of the LNA greatly influences its NF, impacting the quality of the amplified signal; and as receiver noise temperature has a larger influence on the overall system noise temperature with increasing frequency, this becomes a primary concern in the mid-frequency range. To achieve optimum performance, LNA's are often accompanied with cryogenic coolers as is the case with the *MeerKAT Project* [12].

At cryogenic temperatures, NFs are better than 0.1 dB [40], however LNAs with cryogenic cooling are not cost effective for a very large number of receivers, which is the case of the SKA MFAA. Therefore LNAs that operate at room temperature that still meet the required noise performance of the SKA are currently in development and are what will be considered during the thermal analysis of this project. Current reports have shown certain LNA topologies obtaining close to 20 K measured noise temperatures when at room temperature [9], [41]. With a 40 K maximum array noise temperature set for the MFAA this does provide some flexibility for the LNA system temperature [15]. This is incredibly important as the Karoo will often experience climates above that of room temperature although with proper thermal management the MFAA will be able to achieve its set out performance requirements. The rest of the electronic components for the DDA will not be impacted as much by temperature, therefore providing acceptable conditions for the LNA should meet the necessary requirements.

2.5.2 Calibration

Calibration is an integral part of the system design to ensure that the system meets its expected performance. With the MFAA still in the design phase and multiple array topologies being investigated there is still much uncertainty with regards to the approach of calibration. This refers to the set of operations used to establish a correlation between standard reference quantities and values that have been measured. Different procedures are currently being researched such as the method that utilises *Self-holography* to reduce computation power when calibrating the complex valued receive paths within a station [42]. Although, there is still many complexities to be overcome with much to be determined. One of these complexities includes the effect of the array operating temperature when in the Karoo as this will influence antenna parameters and consequently calibration.

Calibration is an imperative procedure for ensuring signal quality and determining the uncertainty in final measurements. This process can become quite difficult for the SKA as the aperture array systems are so large that in order to maintain management over the data volumes a hierarchical signal processing scheme is used [43]. This entails that calibration is required at each level of the signal processing hierarchy to prevent signal losses and ensure proper beam control. The complication arises as each level differs in hardware with different FoVs and sensitivities

impacting the calibratability[1] of the system.

The calibration process is as a result extremely power intensive for such large systems although maintaining a calibrated state is imperative to ensure the accuracy of data collected. Therefore increasing the required period between each calibration will greatly assist with the stability of the system as well as reduce power requirements. However, a typical antenna system is temperature, frequency, signal chain, RFI-environment and zenith angle dependent, and needs to be continuously calibrated on timescales shorter than the variation of each of these parameters [44]. The change in the array operating temperature throughout the duration of the day will have to be considered during thermal analysis of this project as the more stable the temperature, the more stable the system.

2.5.3 Material Conditions

A solid material is made up of a composition of molecules that form a defined shape. When the temperature of the material increases similarly the kinetic energy of the molecules increase and therefore begin to vibrate more rapidly and push away from one another [45], [46]. The separation between the individual atoms causes the solid to expand and is a phenomenon known as thermal expansion. When a material undergoes thermal expansion and has restricted degrees of freedom, great levels of thermal stress is generated. This can compromise the strength and stability of a material, which can potentially lead to cracks or breaks effectively decreasing the material's lifetime. The temperature change ΔT experienced by a material and the corresponding thermal expansion coefficient α_s is equivalent to thermal strain. With Young's modulus E, which is a measure of a material's ability to retain shape, these can be used to determine the thermal stress [47]

$$\sigma_s = E\alpha_s\Delta T \tag{2.12}$$

The deformation from the expansion/contraction of a material is also dependent on thermal strain δ_T and can be determined with the *temperature-displacement relation*

$$\delta_T = \alpha_s\Delta T L \tag{2.13}$$

where L is the initial length of the material. Each of the DDA components have different material properties that might be subject to high thermal stresses and expansion when exposed to the climate of the Karoo and will therefore require analysis. High stresses are most likely to occur at the joints of the array structure and will need to be compared to that of the maximum allowable material stress where no deformation is experienced. As mentioned in §2.2, the ground plane of the DDA is made with an aluminium alloy, the feed-boards are designed using a hydrocarbon ceramic woven glass classified as *RO4003C*, the top plane of the array with substrate FR4 and the support standoffs are PVC plastic. The stress properties of which are shown in Table 2.1.

2.6 Similar Case of Thermal Management

The Octagonal Ring Antenna (ORA) is mentioned in §2.2 as one of the candidates currently in development for the MFAA and is characterised by a planar coupled ring antenna design.

[1] Calibratability not only refers to whether a system can be calibrated but also the level of accuracy at which the process is performed [43].

Material	**Expansion Coefficient** α_s $(\times 10^{-5})$	**Elastic Modulus** E (GPa)	**Mass Density** ρ (kg/m^3)
Aluminium Alloy	1.1	69.0	7850
Substrate FR4	1.4	113.0	1850
PVC Plastic	9.0	3.0	1400
RO4003C	14.0	19.7	1790

TABLE 2.1: *Material properties of the primary components comprising the DDA.*

The model is comprised of four layers each spaced with foam and a central LNA element and is shown in Figure 2.8. The passive layer of the ORA is a metamaterial superstrate layer with conductive rings that are used to stabilise the impedance bandwidth [19].

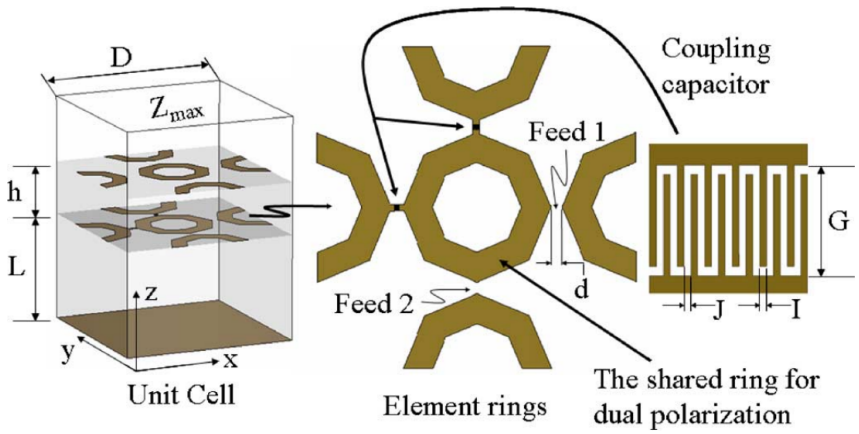

FIGURE 2.8: *Two-dimensional geometry of an ORA unit cell [19].*

The design of the ORA as a multi-layered element limits air ventilation and as a result can lead to a temperature build-up from the trapped air at the bottom of the unit. A thermal design solution is investigated via thermal analysis to deduce whether the LNA maintains within acceptable operating conditions throughout intended operation. Chimneys are integrated into the design to assist with ventilating the air naturally by providing free flow through the array tile. The appropriate size and quantity of chimneys is determined from the amount of heat build-up below the tile and the time it takes for the air to reach a limiting value. With this information the flow rate of a single chimney is calculated and then multiplied to achieve the required amount of air flow to prevent the LNA from exceeding the maximum temperature limit. As the DDA is also likely to experience a temperature build-up within the array, this should be evaluated to conclude whether it will impact performance. Although the DDA may actually benefit from its open design as it has a large surface area exposed to ambient air, and as a result wind will be able to ventilate the system. The thermal analysis of the ORA is evaluated under the extreme conditions of the Karoo and the same approach will be used in the evaluation of the DDA.

2.7 Conclusion

A broad understanding of the literature related to this project was given in this chapter with an emphasis on the importance of thermal management. It started with an introduction to the

DDA and its structural design. This was followed by a description of the modes of heat transfer and common methods of thermal analysis. The effects of temperature on the noise of radio systems is also discussed where it is found that the noise temperature of the DDA is primarily dependent on the noise contribution of the LNA with little influence from sky noise. The chapter closes with a similar case of thermal analysis that incorporates chimneys as a thermal design solution. The next chapter describes the development of the thermal model that will be used to conduct the thermal analysis.

CHAPTER 3

Thermal Model

Contents

This chapter is devoted to the development and testing of the thermal model that will be used to predict the temperature profile of the DDA during operation in the Karoo. The chapter opens in §3.1 with a description of the analysis methods necessary for the thermal simulation. In §3.2 the development of the thermal model begins with the creation of the CAD geometry of the DDA. This is followed by the assumptions when determining the heat transfer listed in §3.3 and the model set-up in §3.4. The thermal load that is expected to act on the DDA when in the Karoo is described in §3.5 along with its application. The model is then finalised in §3.6 with defining the analysis case and the meshing procedure. The focus then shifts in §3.7 to validating the model and determining its accuracy. The chapter finally closes with a brief summary in §3.8.

3.1 Thermal Simulation

A thermal simulation is created of the DDA with *Midas NFX* analysis software [25] that can model the thermal response of a structure under a thermal load. The solution type chosen for

analysis is a non-linear transient heat transfer case that can model the change in temperature of the DDA over time. This is chosen so that a dynamic load that simulates the changing weather conditions of the Karoo can be applied to find the worst case scenarios possible in terms of temperature. Two methods of analysis are required to simulate the heat transfer of the DDA. These include the finite element analysis and CFD. The FEM model is used to model the dynamic thermal load over a transient period, where CFD will be used to simulate the flow of air due to natural convection and determine the increase in temperature within the array.

3.2 DDA CAD Model

To manufacture a telescope the scale of the SKA MFAA within a reasonable budget and to reduce the technical complexities that arise from a system with so many integrating components, a simplistic structural design is necessary. This is to improve the mass production of the components, assist with deployment and limit the level of maintenance required. The DDA has achieved this criteria with a planar structure consisting of two flat layers and connecting components of basic shape as described in §2.2. To perform the thermal simulation of the DDA an accurate CAD model portraying the dimensions and configurations of each of the components is necessary. These dimensions are given in Table 3.1.

Component	Length	Width	Thickness
Top Plane	1080	1080	0.8
Feed-board	75	35	2
Standoff	75	D10	-
Ground Plane	1080	1080	2

TABLE 3.1: *Physical dimensions in mm of each of the DDA components.*

The CAD model of the DDA shown in Figure 3.1 and 3.2 is generated with *Autodesk Inventor Professional*, where each of the individual components are first created and then assembled with the appropriate joints and constraints. The model resembles that of the prototype developed in [21] where only two quadrants of the array have been connected with feed-boards. This is done so that a comparison can later be made between the thermal simulation results and a measured experiment on the prototype that will serve as a form of validation for the model. The ground plane is first constructed with the drilled holes to provide the appropriate placement of the feed-boards and support standoffs. A simplification is made to the feed-boards by removing the SMA connectors and extending the length to the point of contact with the ground plane. It is assumed that the connectors will have little thermal influence as the feed-boards have a very low thermal conductivity and thereby removing them will greatly improve model meshing without hindering results. Finally, the top plane is modelled with a simple rectangular plate of 0.8 mm and assembled with the other components to form the DDA.

3.3 Assumptions

The following assumptions have been made in the development of the model:

I All contact surfaces between components are fully effective in conduction as each joining component has a low thermal conductivity with a small surface area of connection and will result in a very low thermal contact resistance.

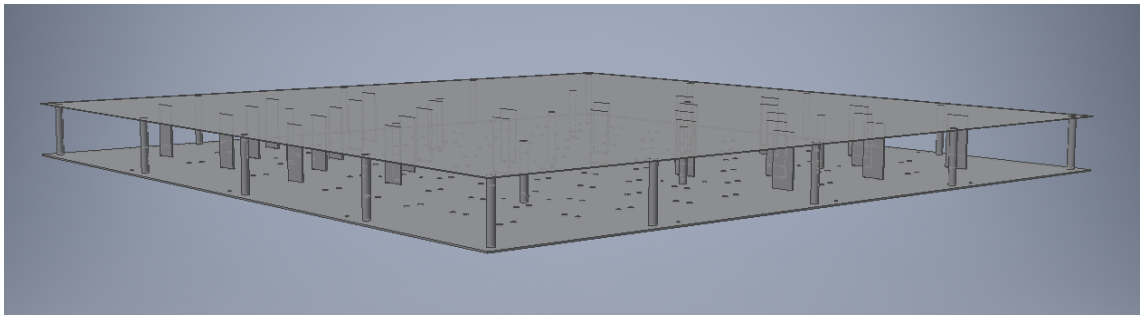

FIGURE 3.1: *The top-view of the DDA prototype CAD model.*

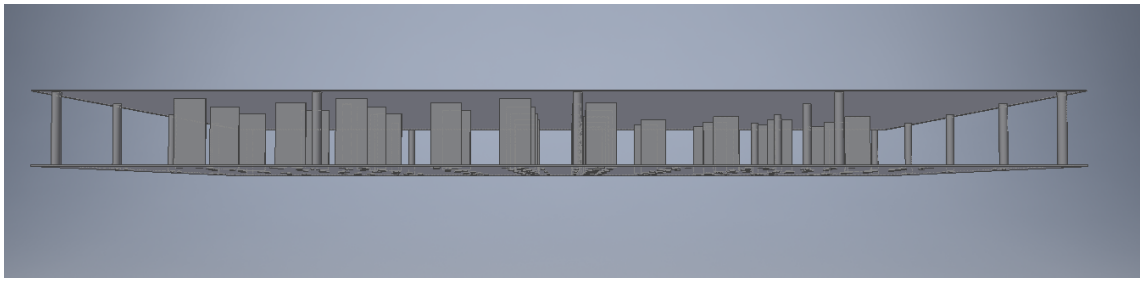

FIGURE 3.2: *The front-view of the DDA prototype CAD model*

II The array elements and feed lines printed onto the surface of the top plane will have no effect on the thermal conductivity of the material as they are non-continuous.

III Wind is not considered in the thermal simulation as this will only improve ventilation of the system and alleviate critical conditions.

IV A cloudless environment is modelled for the weather conditions such that the intensity of solar irradiance and sky radiation is not mitigated.

V Air is free to move within and around the array through natural ventilation as the DDA is intended to be positioned 1∼1.5 m above the ground.

VI The ground plane is never exposed to direct sunlight as this is covered by the antenna layer.

VII Only heat dissipation from the LNA is considered as the power of the received signal will generate negligible amounts of heat and the additional electronic components situated below the ground plane such as the beam formers are still unknown with regards to size and power levels.

VIII All materials are considered to be isotropic and the air surrounding the array is given the properties of an incompressible ideal gas.

3.4 Model Set-up

The assembly CAD model of the DDA is imported into *Midas NFX* as a *CATProduct* while still permitting modification for each individual component. The model is first simplified by removing each of the drilled holes in the ground plane. These can be removed as they are intended to be filled with the SMA connectors of each feed-board, which in turn will be connected to co-axial cables allowing no air to pass through. The contact surfaces between each of the components

are located and then defined with a fully effective surface to surface bond as per the assumption in §3.3. The thermal properties necessary for calculation are applied to each of the component models by assigning the corresponding isotropic material. During meshing these properties provided in table 2.1 will then be carried over to the mesh nodes generated for the array.

3.5 Thermal Load

The thermal load describes the heat transfer processes that take place within a medium as well as the heat exchanged between the medium and its surroundings. The DDA will experience various types of heat transfer when deployed in the Karoo and these are shown with the thermal schematic in Figure 3.3. Each of these thermal loads are to be applied to the model such that an accurate simulation can be attained.

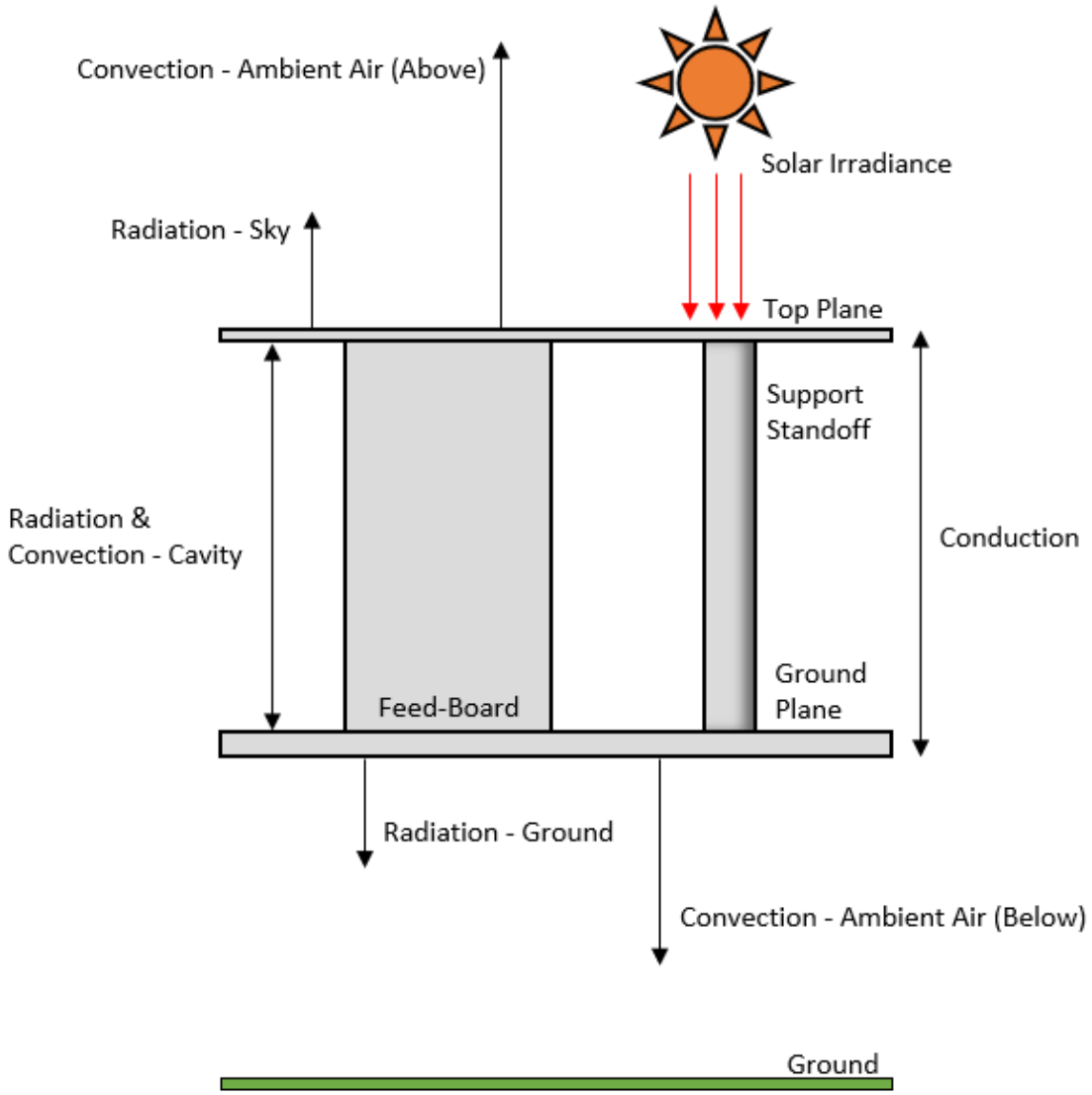

FIGURE 3.3: *Thermal schematic of the DDA displaying the acting heat transfer processes.*

3.5.1 Solar Irradiance

The solar irradiance is the Sun's radiant power per unit area, in the form of electromagnetic radiation exerted on a surface under solar exposure. The intensity of the Sun's rays at the outer edge of the Earth's atmosphere can be defined by the solar constant, which is the average solar irradiance experienced when the Earth is the mean distance from the Sun. This value is found to be 1367 W/m^2 with use of the*Stefan's Boltzmann's Law* from the following calculation

$$G_{sc} = \sigma T^4 \left(\frac{4\pi R}{4\pi D}\right)^2 \tag{3.1}$$

where R and T represent the radius and temperature of the Sun, and D is the average distance between the Sun and the Earth. As these rays travel through the Earth's atmosphere a significant amount of solar radiation is attenuated through absorption and reflection before reaching the surface. When the irradiation on the top plane of the array hits the surface, one part is reflected, another part is absorbed and the rest is transmitted. The total solar energy incident on the unit area of a horizontal surface can be expressed as [24]

$$G_{solar} = G_D \cos\theta + G_d \tag{3.2}$$

where the solar radiation that reaches the surface without being scattered or absorbed is called the direct solar radiation G_D and the scattered radiation that still reaches the surface is called the diffuse solar radiation G_d. Lastly, θ is the angle of incidence of direct solar radiation. As a result the peak solar flux on a surface is generally experienced when the sun is positioned directly overhead relative to the surface, close to the zenith point. Many additional factors can also influence the intensity of the solar flux such as cloud cover and the level of pollution in the area.

The solar irradiance that will be experienced by the DDA is applied to the model as a uniformly distributed heat flux in W/m^2, on the face of the top plane that is exposed to the sun. This is the primary source of thermal energy that is transferred to the DDA during the day and will greatly influence the operating temperature.

3.5.2 Conduction

One of the primary modes of heat distribution throughout the model to attain thermal equilibrium is conduction. From Equation 2.1 it is seen that the rate of heat transfer is dependent on the the surface area of connection and the thermal conductivity of the material. Conduction is applied to the model during the model set-up where each of the components are assigned a thermal conductivity from the corresponding material and by defining each of the contact surfaces. With the thermal conductivities of most of the materials fairly low as they are non-metallic despite the ground plane, the heat transfer via conduction will occur at a slow rate.

3.5.3 Convection

Convection is the transfer of heat from one place to another through the mass motion of a fluid. This is therefore dependent on the type of fluid motion as well as the thermophysical properties of the fluid. As discussed in §2.3.1 there are two types of convection, namely forced and natural. With the shear size of the MFAA no forced cooling is to be implemented in an attempt to

reduce technical complications and alleviate budget expenditure. This implies that only natural convection heat transfer will occur in the absence of wind and is what will be modelled in the simulation. Buoyancy forces induce free convection currents that generate motion in a fluid where there are density gradients and is typically due to a difference in temperature.

To determine the rate of convective heat transfer between a solid and fluid during natural convection the surface area and film coefficient are required for Equation 2.2. The film coefficient from its units can be defined as the rate of heat transfer between a solid surface and a fluid per unit surface area per unit temperature difference [24]. As the coefficient is dependent on so many variables it becomes difficult to determine and as a result, relationships have been discovered through empirical data for various cases. The DDA is comprised of horizontal and vertical plates that experience natural convection with ambient air. The film coefficients can be calculated from the corresponding empirical expressions in [24]. For a horizontal plate such as the top plane of the array the following calculation can be performed

$$Gr_L = \frac{g\beta(T_s - T_\infty)L_c^3}{v^2} \tag{3.3}$$

where Gr_L is the *Grashof* number, g is the gravitational acceleration, β is the coefficient of volume expansion, L_c is the characteristic length defined below and v is the kinematic viscosity of the air. The *Rayleigh* number Ra_L is the product of the *Grashof* and *Prandtl* number P_r, which describes the relationship between buoyancy and viscosity within a fluid and the relationship between momentum diffusivity and thermal diffusivity, respectively.

$$Ra_L = Gr_L P_r \tag{3.4}$$

This is used to determine the *Nusselt* number Nu from the following derived formula for a horizontal plate.

$$Nu = 0.54 Ra_L^{\frac{1}{4}} \tag{3.5}$$

The *Nusselt* number represents the enhancement of heat transfer through a fluid layer with convection, relative to the heat transfer through the same fluid layer with conduction. With the *Nusselt* number the following relationship can be used to determine the resulting heat transfer coefficient

$$h = \frac{k}{L_c} Nu \tag{3.6}$$

where k is the thermal conductivity of the air and the characteristic length L_c is found from the surface area and the perimeter p of the convective surface.

$$L_c = \frac{A_s}{p} \tag{3.7}$$

Convection is applied to each of the faces of the array model that are exposed to ambient air. Although in the FEM model the conduction heat transfer applied to each surface only considers the direct contact between the surface and the adjacent fluid. This does not consider the temperature distribution within the fluid. An additional simulation is therefore necessary with CFD analysis to model the air flow inside of the array to determine the temperature build up of air in the cavity and the resultant ambient temperature below the ground plane.

3.5.4 Radiation

Apart from the solar radiation experienced by the DDA an additional radiative heat transfer process is applied to the model. This originates from the gas molecules and suspended particles in the atmosphere as they emit as well as absorb radiation [22]. It is often convenient during heat transfer calculations to model the atmosphere as a blackbody (*i.e.* a perfect emitter and absorber of radiation), that emits an equivalent amount of radiation energy at some temperature. This is termed the effective sky temperature T_{sky}, and depends on the atmospheric conditions. As per assumption IV, a cloudless environment is modelled and therefore the sky temperature can be related to the ambient temperature with the following formula from [48].

$$T_{sky} = 0.05522(T_{amb})^{1.5} \tag{3.8}$$

As the DDA experiences an increase in temperature from the absorbed radiation, a part of that energy will leave the surface of the array. The amount of radiation emitted from the surface at a given wavelength depends on the surface temperature as well as the material of the body and the condition of its surface. The emissivity of a material denoted by ε, represents the ratio of radiation emitted at a given temperature to the radiation emitted by a blackbody at the same temperature and therefore varies between one and zero [24]. A plastic material often has a fairly high emissivity as is the case with *FR4*, which results in a high radiation intensity for emitted radiation. The amount of energy emitted $E_{emitted}$ from a surface may be calculated with *Stephan-Boltzman's law*.

$$E_{emitted} = \varepsilon\sigma T_s^4 \tag{3.9}$$

The total net radiation heat transfer acting on the top plane of the array when exposed to sunlight can then be determined from the following energy balance equation.

$$\begin{aligned} \dot{q}_{net,rad} &= \Sigma E_{absorbed} - \Sigma E_{emitted} \\ &= \alpha G_{solar} + \varepsilon\sigma T_{sky}^4 - \varepsilon\sigma T_s^4 \\ &= \alpha G_{solar} + \varepsilon\sigma \left(T_{sky}^4 - T_s^4\right) \end{aligned} \tag{3.10}$$

The solar absorptance α is a measure of a materials ability to absorb radiation and is defined as 0.4 for *FR4*. When the array is constantly absorbing radiation from the sun during the day an overall positive heat gain will occur and the array will increase in temperature. As the sun starts to set, the amount of heat absorbed decreases to the point where the energy emitted overcomes that which is absorbed and the array will drop in temperature. During the night no heat is gained from the sun and the low sky temperature will induce what is known as night radiative cooling. The down welling thermal radiation absorbed by the array from the sky temperature will barely negate the amount of heat emitted from the arrays surface under the night sky. This will result in an overall negative net radiation and therefore a heat loss. An empirical formula has been developed to determine the down welling sky radiation Q_{sky} in [49] that considers the effects of clouds and humidity.

$$Q_{sky} = \left(1 + KC^2\right)\left(8.78 \times 10^{-13}\right) T^{5.852} RH^{0.07195} \tag{3.11}$$

Where K represents a derived coefficient for cloud height, C is the level of cloud cover (0 for a clear sky and 1 for totally overcast) and RH is the relative humidity percentage. From this

formula it can be seen that cloud cover will increase the down welling thermal radiation and therefore reduce the temperature drop experienced by the DDA. By assuming no cloud cover the DDA will undergo a more critical temperature change for a more conclusive thermal analysis to determine the suitability of the array under extreme conditions.

The radiation that occurs on the surface above the array is applied to the FEM model with a radiative thermal load, specifying the view factor and ambient temperature. As the top of the array has an unobstructed view, a view factor of one is defined and the temperature is set to sky temperature. The same load is applied to the base of the model although with the ambient temperature below the ground plane. The radiation that occurs inside of the array will contribute towards a temperature build up and is modelled in the CFD simulation.

3.5.5 Internal Heat Transfer

The DDA is assumed to undergo natural convection such that no forced cooling is applied and no wind is considered. This implies that the air within the array will be subject to natural ventilation in that only the fluid motion induced by density gradients will refresh the internal air. As the top of the array begins to increase in temperature from the thermal loads discussed above an increase in air temperature is expected within and below the array due to the slow air flow rate. This increase in air temperature can be determined based on the assumption that the heat emitted through convection and radiation from surfaces within and below the array results in an increase in surrounding air temperature. The rise in air temperature within and below the DDA can be represented with Equation 3.12.

$$Q = mC_p\Delta T \tag{3.12}$$

Where Q is the heat flow into the air from the surface in (J), m is the mass of air in (kg), C_p is the specific heat capacity of air in $(J/kg \cdot K)$ and ΔT is the change in air temperature in (K). To accurately model the increase in air temperature a CFD simulation is used. This is capable of determining the heat transfer in the air as well as the motion of the air during natural ventilation. When situated in the Karoo, the DDA tiles are intended to be positioned next to one another to form a station. It is therefore unlikely that the open sides of the array will be exposed to air at ambient temperature and rather another DDA. For validation purposes the array sides are modelled as open such that a proper comparison can be made with an experiment of the DDA prototype. The array in a station configuration will need to be considered at a later stage in the project.

The CFD simulation is first established by creating the geometry of the top and bottom planes of the array and defining the gravitational load. This is followed by defining the computational fluid domain that will represent the air surrounding the array. This is set large enough to allow for natural convection to take place. As the air is not trapped in a vacuum inside of the array the simulation is set up as an external flow simulation. The simulation will therefore consider the flow of air around and inside the array. To simulate the effects from the buoyancy forces the air is defined as an incompressible ideal gas. This simplifies the simulation for a better convergence while still allowing the local pressure to influence density ρ with the following expression.

$$\rho = \frac{P_{op}}{\frac{R_G}{M_w}T} \tag{3.13}$$

The incompressible ideal gas law states how the density is determined, where P_{op} is the operating

pressure, R_G is the universal gas constant (8.314 $J/mol \cdot K$), M_w represents the molecular weight of air and T the temperature. This is accompanied by the analysis case setting that enables *floatability by density* to simulate the rise of hot air as it expands and the fall of cold air as it condenses. Each of the modelled components are then defined with their corresponding CFD material properties listed in Tables 2.1 & 3.2, after which the boundary conditions are applied. These include wall boundary conditions between the contact surfaces of the air and solid and a pressure boundary condition that sets the sides of the air model to atmospheric pressure. To ensure conjugate heat transfer between the solid and fluid, *fluid-solid* contact types are defined on all the exposed faces.

Material	**Specific Heat** C_p $(J/kg \cdot K)$	**Thermal Conductivity** k $(W/m \cdot K)$
Aluminium Alloy	300	231
Substrate FR4	896	0.556
PVC Plastic	1000	0.16
RO4003C	880	0.71

TABLE 3.2: *Thermal properties of the primary components comprising the DDA.*

Radiation can have a more significant rate of heat dissipation than convection in situations with natural convection and therefore needs to be considered. This is done by applying a radiative surface condition to the surface of each part with their corresponding emissivity and absorptance. The simulation is run with solar radiation acting directly on the top plane of the array and the environmental temperature set to the sky temperature. The rise and fall in temperature of the air within the array can then be computed over a transient analysis with the *k-epsilon* turbulence model. The resultant thermal air profile is then applied to the FEM model through a convective load with the fluid convection effects to determine the final resulting temperatures of the DDA.

3.6 Analysis Case and Meshing

The FEM model is meshed using a hybrid meshing technique with an adaptive seed factor of 1.5 and with geometry proximity control to increase the number of nodes near edges of the model. Since the aspect ratio is so high as a result of the flat plates representing the top and bottom plane of the array a very fine mesh size is used to ensure no poor elements are attained. The meshed model can be seen in Figure 3.4. The total mesh is comprised of 25092 thermal three-dimensional solid elements with the appropriate material properties. A non-linear transient thermal analysis case is created to analyse the model over a defined period with the set initial conditions.

3.7 Model Validation

To validate the model generated for the DDA and determine the degree to which the model is an accurate representation of the real world scenario, a comparison between modelled results and measured data is required. To obtain the measured data an experiment is performed with the prototype of the DDA developed in [21], where temperature measurements are recorded on the array when outside under exposed solar radiation. The experiment is performed on three

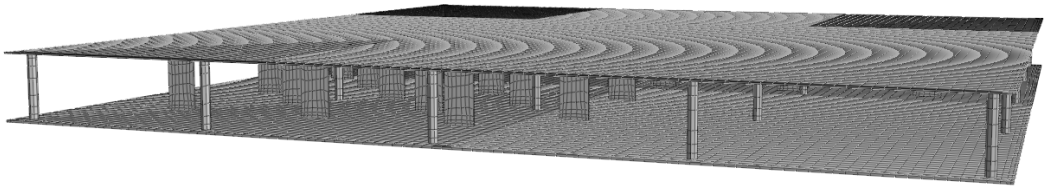

FIGURE 3.4: *The mesh of the DDA model.*

separate days to gather temperature measurements under different weather conditions for a thorough comparison.

3.7.1 Experiment Set-up

To perform the experiment in such a manner that an accurate comparison can be made between the modelled results and the measured data; the thermal load applied to the model must match the weather conditions experienced by the DDA, and the location points of temperature comparison must be the same for both the model and prototype. The equipment used to conduct the experiment and meet the necessary conditions is provided in Table 3.3.

Quantity	Part	Description
1	Arduino Uno	DIP Rev. 3
4	Thermistor	AVX NJ28
4	Resistor	10kΩ
1	Weather Station	Oregon Scientific WMR89
1	Thermo Hygro Sensor	Cable Free 3.0

TABLE 3.3: *The equipment used to conduct the validation experiment.*

The *Oregon Scientific* weather station is used in conjunction with the *Thermo Hygro Sensor* to record the ambient conditions experienced by the DDA during each day. This is done so that the same thermal conditions experienced by the prototype can be applied to the model for an accurate comparison. To validate the temperature distribution throughout the model, multiple thermistors are used to compare the temperature values at different locations along the vertical axis of the DDA. The NJ28 Thermistors [50] have been chosen as the temperature sensors for the experiment and are a negative temperature coefficient type. This means that as the temperature of the thermistors increase, their resistance will decrease and therefore with an appropriate conversion a temperature reading can be attained. An *Arduino Uno* is used as the micro-controller to process the readings of the thermistors and is programmed with the *Arduino IDE* interface. The development board also provides a stable voltage supply, which will be used for each thermistor.

The circuit diagram of how each of the electronic components are connected is shown in Figure 3.5. Each thermistor is wired in a simple voltage divider configuration with a 10kΩ resistor. The pairing resistor is chosen as 10kΩ as this matches the resistance of the NJ28 thermistors. The voltage across each thermistor is carried to the analog inputs of the *Arduino Uno* for measuring. To gather temperature readings from each thermistor a three step conversion is required. The

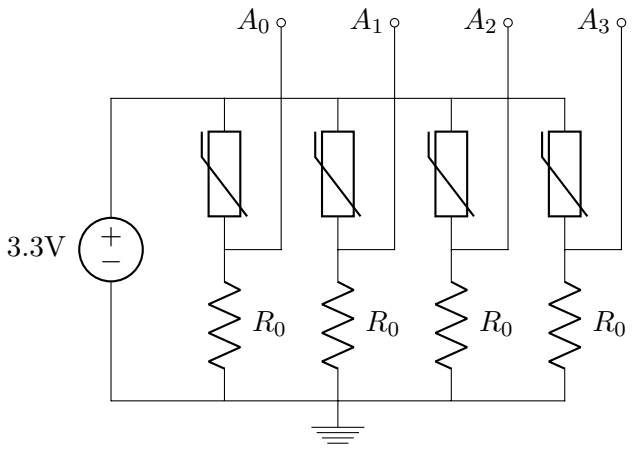

FIGURE 3.5: *Circuit diagram of the thermistors for the measured experiment.*

first step involves sending the voltage value that is across each thermistor to the analog ports of the *Arduino Uno*. This is so that a digital representation of each voltage can be acquired with the analog-to-digital converter (ADC). In an effort to reduce noise, the 3.3 V supply is used as this is more stable and the ADC reading is taken over an average of ten measurements before being converted. The next conversion step involves determining the resistance of each thermistor from the corresponding digital voltage value and is done with the following derived Equation 3.17.

$$V_o = \left(\frac{R}{R + R_0}\right) V_{cc} \tag{3.14}$$

$$ADC = V_i \left(\frac{1023}{V_{cc}}\right) \tag{3.15}$$

With the output voltage of each thermistor V_o equivalent to the input voltage V_i supplied to the ADC, the following simplified expression is attained:

$$\therefore ADC = 1023 \left(\frac{R}{R + R_0}\right) \tag{3.16}$$

Rearranging Equation 3.16 for thermistor resistance:

$$R = R_0 \left(\frac{ADC}{1023 - ADC}\right) \tag{3.17}$$

With the resistance value for each thermistor acquired in a digital representation, the temperature can be calculated in the final conversion step. This is done with an empirical expression that provides a relationship between the resistance and temperature of thermistors, known as the *Steinhart-Hart* equation:

$$\frac{1}{T} = A + B \ln(R) + C(\ln(R))^3 \tag{3.18}$$

Although this has been simplified to the β *parameter* equation in the following expression, acceptable for use with NTC thermistors at ambient temperatures.

$$\frac{1}{T} = \frac{1}{T_0} + \frac{1}{B} \ln\left(\frac{R}{R_0}\right) \tag{3.19}$$

Where T_0 is the room temperature in Kelvin and B is the thermistor coefficient, unique to each thermistor type. This is provided in the NJ28 datasheet [50] as 4100. After applying the simplified *Steinhart-Hart* equation to each resistance value, the corresponding temperatures can be determined. Lastly, the temperature values are converted to degrees Celsius and programmed to be displayed on the serial monitor with a time stamp each minute using a real-time clock (RTC).

Before the experiment is performed the accuracy of each thermistor needs to be evaluated. This is simply done by placing the thermistors in a controlled environment at a specific ambient temperature and comparing the thermistor readings. The closed room has a recorded temperature of around 22.5°C that has been measured with the weather station. The thermistors are placed within the room and are set to record for a two hour period. The temperature readings from each thermistor are shown in Figure 3.6. From the graph it can be seen that the thermistors are close to room temperature with an accuracy of about 0.05°C. The discrepancy between each thermistor reading is also very small as they closely follow the same path. The thermistor set up is therefore within an acceptable accuracy for use in the experiment.

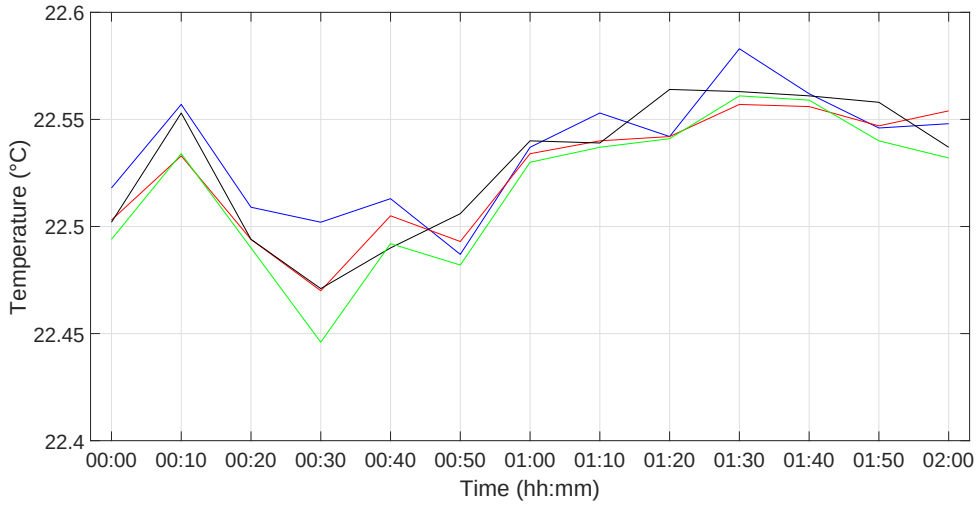

FIGURE 3.6: *Temperature readings of each thermistor in a controlled environment.*

To measure the temperature profile of the DDA, each thermistor is positioned along the vertical axis close to the center. This is where the temperature build up within the cavity will be the highest and is what has been modelled. The first thermistor is placed on the top plane of the array, which is to be used to gather an estimate value of the solar flux experienced by the DDA. The second thermistor is placed on the internal surface of the top plane and the third is positioned half way down one of the central feed-boards. Lastly, the fourth is placed on the inner surface of the ground plane. With each thermistor attached, the array is then ready to be placed on the roof of the engineering building in *Stellenbosch*. The roof is chosen as it will provide unobstructed sun exposure on the DDA and is slightly shielded from wind. Polystyrene cut-outs are placed underneath each corner of the array to mitigate conductive heat transfer from the ground (as this is not modelled in the simulation) and provides cushioned support. Figure 3.7 shows the array while positioned on the roof. The *Arduino Uno* is then connected to the laptop alongside the array with the weather station and sensor shown in Figure 3.8, to

record the weather conditions.

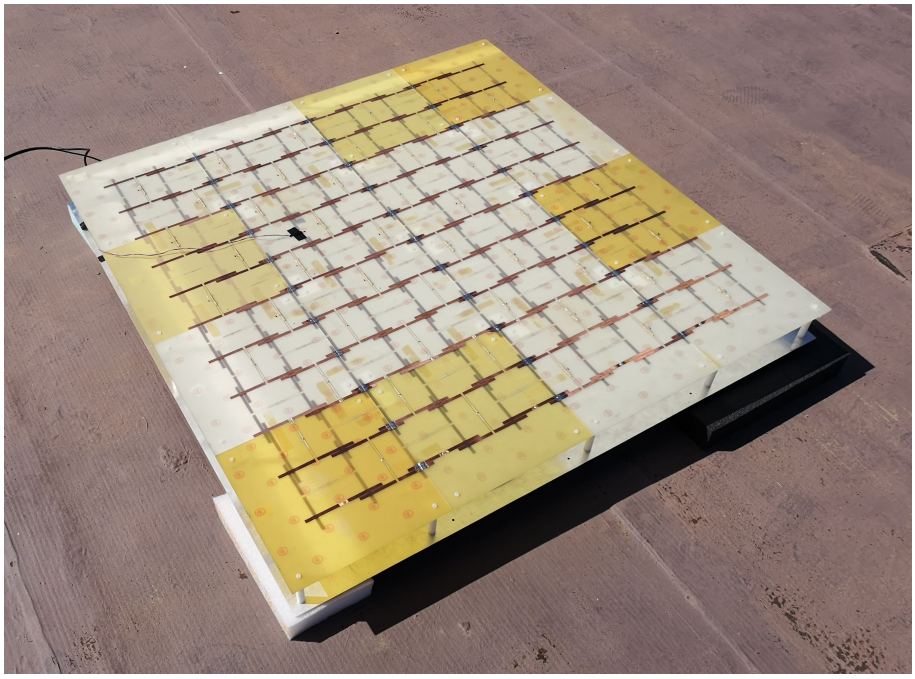

FIGURE 3.7: *The DDA positioned on the roof with each of the thermistors attached.*

FIGURE 3.8: *The laptop connected to the Arduino Uno with the weather station.*

3.7.2 Experiment Results

The experiment is run on three separate days with high ambient temperatures and little to no wind. These days are chosen as the weather conditions best adhere to the assumptions made in the model such that an acceptable comparison can be made between the results. The experiment is run during the hottest time of the day between 11:00 AM and 16:00 PM with the results shown in Figures 3.9, 3.10 and 3.11.

From the graphs it can be seen that the temperature difference between each of the thermistor

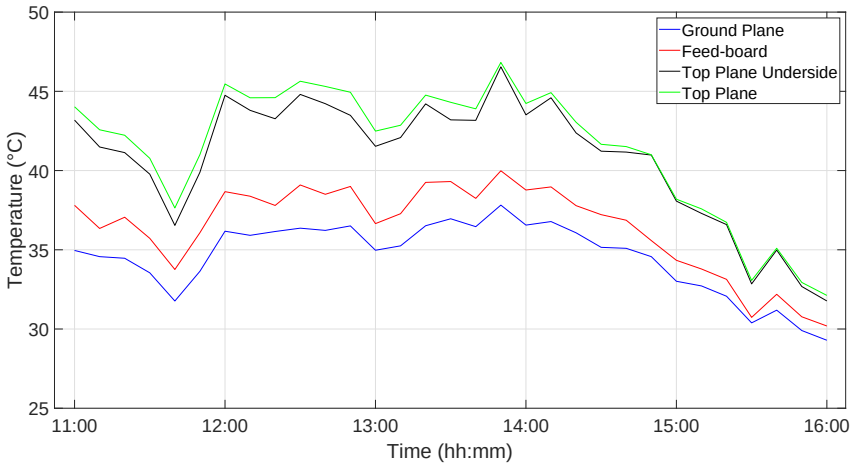

FIGURE 3.9: *The thermistor temperature measurements of Day 1 for the DDA experiment.*

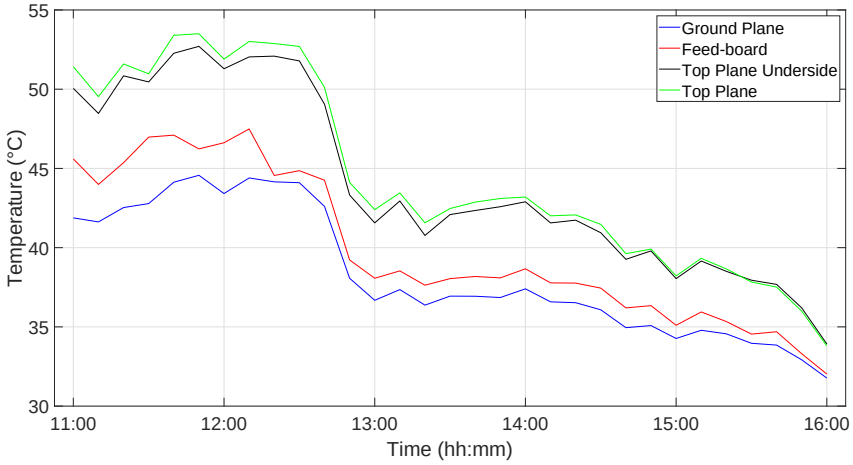

FIGURE 3.10: *The thermistor temperature measurements of Day 2 for the DDA experiment.*

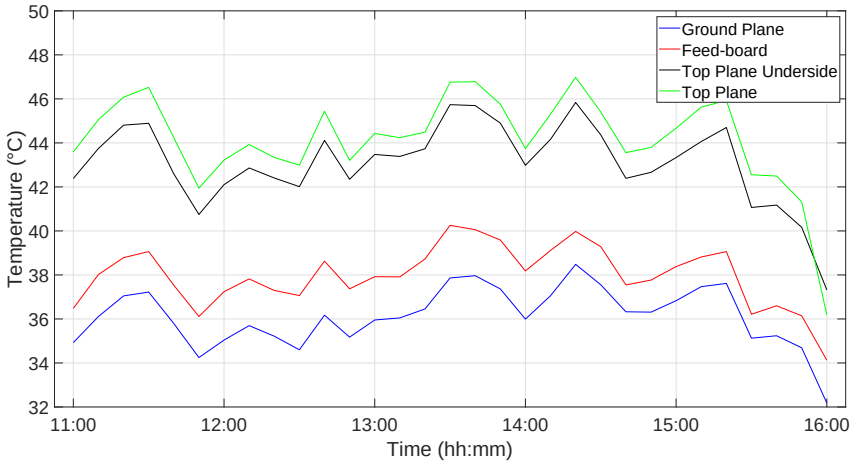

FIGURE 3.11: *The thermistor temperature measurements of Day 3 for the DDA experiment.*

positions remains fairly consistent over the majority of the period. Towards the end of the experiment period the temperatures do tend to drop off as the sun begins to set and the temperature difference decreases. The peak temperatures from each day appear to occur around noon where the solar irradiance is generally the strongest. Day 2 does experience a fairly drastic heat loss at around 12:30 that is most likely due to cloud cover. It is evident that a fair amount of noise is present in the readings and will have to be considered during comparison.

3.7.3 Modelled Results

To make a comparison between the model predictions and measured results, the conditions in both cases must be the same. This implies that the the weather conditions experienced during each day of the experiment must ultimately be applied to the model. The variables that describe the weather and are necessary to apply a matching thermal load include the ambient temperature and solar irradiance. The *Oregon Scientific* weather station together with the *Thermo Hygro Sensor* is used to determine the ambient temperature of the air surrounding the array. The level of solar flux acting on the top surface of the DDA is determined with *Midas NFX*. This is done with the temperature reading of the thermistor placed on the top plane of the array, the ambient temperature and the thermal properties of *FR4*. With both of the variables acquired, the thermal load can be applied to the model to determine the thermal distribution of the array as well as the temperature build-up of air inside the cavity. To mitigate the effects of noise, the comparison is made between 12:00 and 12:30. Here the results from the measured data is fairly constant and the array is close to peak temperature.

Day 1

At 12:00 till 12:30 on experiment day 1, the ambient temperature is recorded at 31°C and the solar irradiance is calculated in *Midas NFX* to be 560 W/m^2. This thermal load is first applied to the CFD model to determine the temperature build-up of air within the array with the air temperature set to ambient and the solar radiation on the top plane. The following air temperature distribution is acquired and shown in Figure 3.12 with a cut plot at the center of the array.

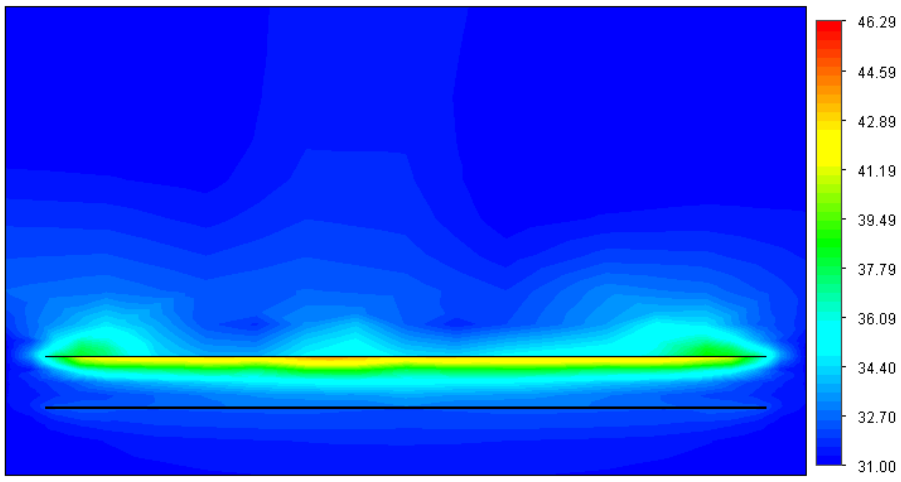

FIGURE 3.12: *Air temperature distribution of experiment day 1.*

In this figure the temperature build-up of air below the top plane due to limited ventilation

and the rise of hot air can be seen. Despite the temperature of the top surface of the plane being higher than that of the underside, the air in contact with this surface is able to escape as it rises and together with its exposure to the sky does not experience the same increase in temperature. By applying the air model to the FEM simulation described in §3.5 with the thermal load corresponding to the day 1 weather conditions the thermal image of the DDA is attained in Figure 3.13. The array reaches a maximum predicted temperature of 45.02°C on the top plane and a minimum of 34.1 at the edge of the ground plane. The legend for the thermal image is set from 30°C to 53°C such that a visual comparison can be made between the thermal images of each day.

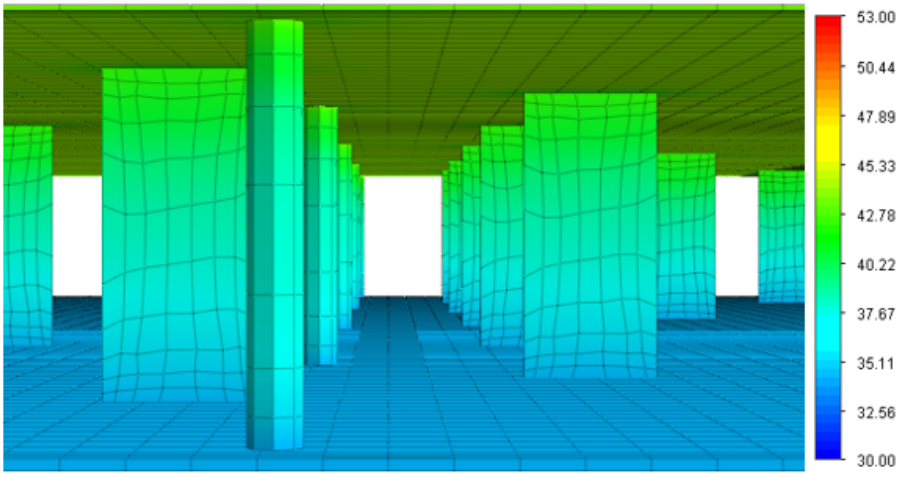

FIGURE 3.13: *The DDA thermal image of experiment day 1.*

Day 2

The ambient temperature measured between 12:00 and 12:30 on day 2 with the weather station was 35°C and the solar irradiance is calculated to be 690 W/m^2. Day 2 of the experiment has a higher temperature together with a stronger solar flux and as a result the DDA experiences higher temperatures. The increase in air temperature at the centre of the array is found to reach an average of 43.2°C, a 9°C increase from ambient. The model is shown in Figure 3.14.

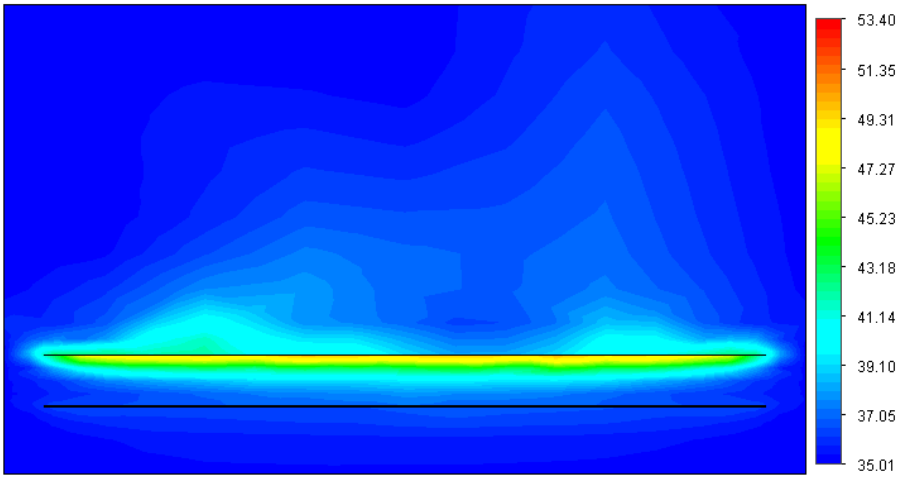

FIGURE 3.14: *Air temperature distribution of experiment day 2.*

The FEA thermal image of the array is shown in Figure 3.15. With the increase in air temperature and the high level of solar irradiance, the DDA is predicted to reach a maximum of 52.28°C on the top plane and a minimum of 41.77°C on the ground plane.

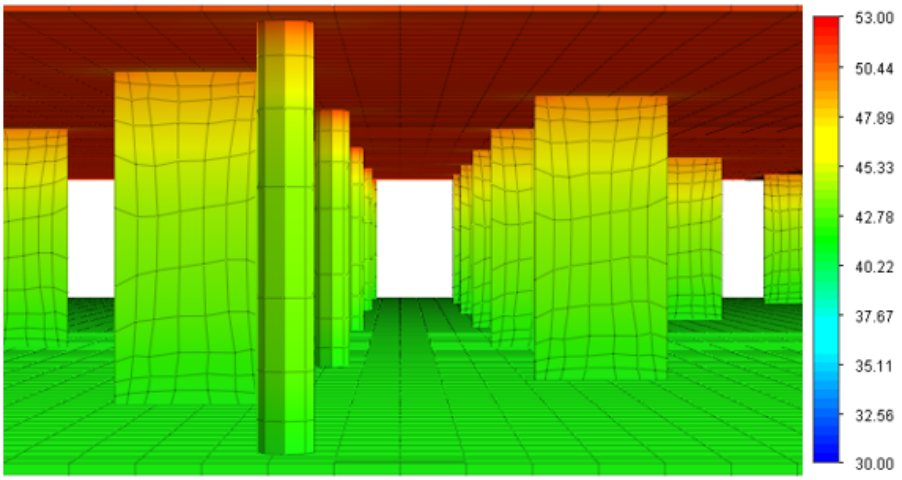

FIGURE 3.15: *The DDA thermal image of experiment day 2.*

Day 3

On day 3 of the experiment, the ambient temperature is found to be slightly cooler than that of day 1 and is measured at 29°C with a solar irradiance of 550 W/m^2. The resulting increase in air temperature within the array is shown in Figure 3.16.

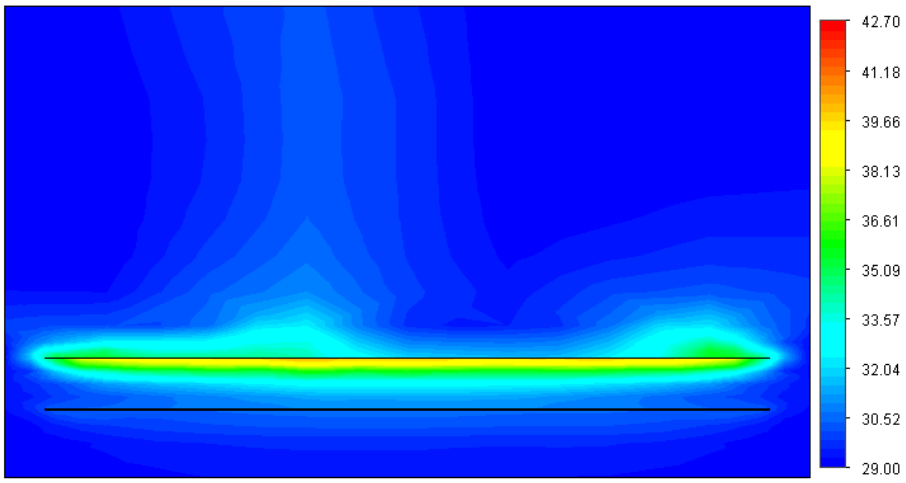

FIGURE 3.16: *Air temperature distribution of experiment day 3.*

The thermal image of the temperature distribution through the inside of the DDA for day 3 of the experiment is shown in Figure 3.17. The temperature distribution closely resembles that obtained from the first model only with slightly lower temperatures. The minimum temperature is found to be 33.21°C and the maximum reaches 42.77°C.

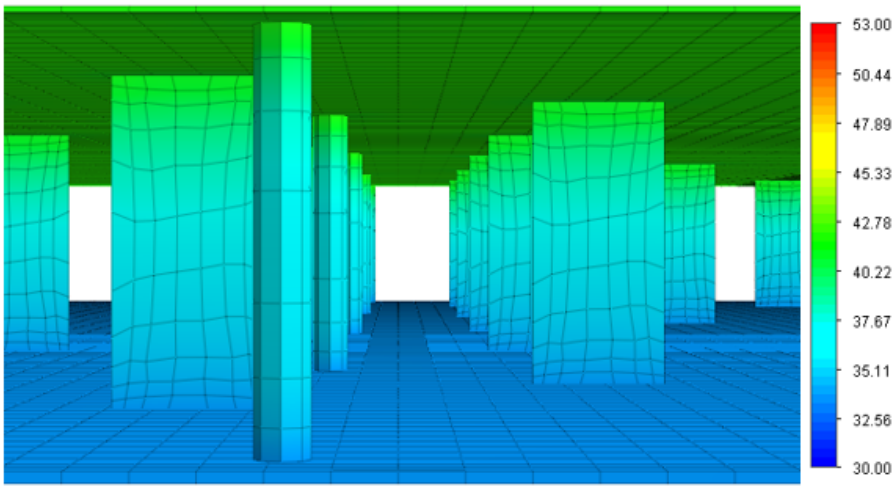

FIGURE 3.17: *The DDA thermal image of experiment Day 3.*

3.7.4 Temperature Comparison

To compare the temperatures between the modelled predictions and those measured during the experiment, nodal points are taken near the centre of the array corresponding to the placement of thermistors. The comparison is made with the three nodal temperatures and the average measured temperature from 12:00 till 12:30 for each day. The tabulated results are provided in Table 3.4 along with Figure 3.18 of the probed temperatures.

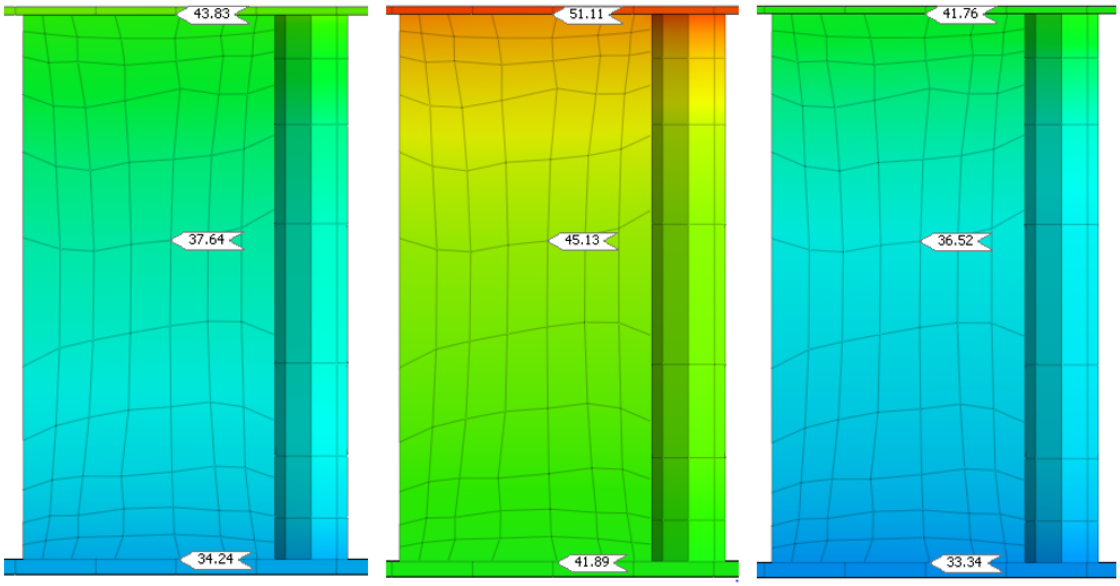

FIGURE 3.18: *Thermal images of the nodal temperatures across the three days starting with day 1 on the left.*

The temperature values determined in the simulation compare fairly well with the measurements on all three days. The biggest discrepancy appears to be with the ground plane temperatures, where the predicted values are lower than those measured. This is most likely due to some sunlight shining directly on to the ground plane and has consequently caused an increase in temperature, which has not been accounted for in the model. Overall the simulation should provide enough accuracy for an effective thermal analysis.

	Temperature °C					
	Day 1		Day 2		Day 3	
Location	Measured	Model	Measured	Model	Measured	Model
Top Plane	44.16	43.83	51.80	51.11	42.35	41.76
Feedboard	38.48	37.64	45.88	45.13	37.35	36.52
Ground Plane	36.15	34.24	44.02	41.89	35.14	33.34

TABLE 3.4: *The temperature comparison between the model predictions and the experiment measurements.*

3.8 Conclusion

This chapter was devoted to the development of a thermal simulation that can accurately portray the temperature distribution of the DDA under specified conditions. The theory behind the thermal load that acts on the DDA was discussed along with its application in the simulation. This was followed by the procedure for meshing the array and the analysis case used for the model. With the thermal model complete a validation procedure was then performed through an experimental comparison. The set-up of the experiment was discussed along with the results obtained for each day. Finally, a thermal load matching the weather conditions for each day was applied to the model and the results were compared. It was found that the level of accuracy of the model should be of an acceptable level to conduct a thermal analysis.

CHAPTER 4

Modelled Simulations

Contents

It is imperative that the DDA is maintained within the operating limits for desired performance when in the Karoo. To ensure this, this chapter is devoted to simulating the thermal response of the DDA for analysis in the most extreme climate conditions recorded at the SKA site. The chapter opens in §4.1 with the updated DDA model to simulate the temperature profiles of the final product. This is followed by the heat dissipation of the LNA in §4.2 and the corresponding effects. The focus shifts in §4.3 to the operating limits of the DDA that will provide the conditions of its suitability in the Karoo. §4.4 & 4.5 begin the assessment of the DDA, with the temperature responses in the hot and cold environments respectively throughout the duration of a day. The chapter is concluded in §4.6 with the evaluation of the DDA's suitability in the Karoo.

4.1 Fully Fed DDA

The final product of the Dense Dipole Array is intended to have all its elements connected to achieve its full receiving aperture, as was shown in §2.3. This entails that each element be connected to a feed-board. Therefore to accurately portray the DDA that will be deployed in the Karoo, all the feed-boards are added to the CAD model. This is shown in Figures 4.1 and 4.2. Modifying the CAD for a fully fed DDA, will not compromise the validity of the model

developed in the previous chapter. This is because the feed-boards have already been accounted for and so the same thermal load and properties will simply be replicated.

With the addition of more feed-boards, the heat transfer throughout the array may be influenced. For instance, the surface area of exposed faces to convection will increase providing a better exchange with the air temperature. This could assist with drastic temperature changes experienced in the early mornings as there will be more convection heat transfer with the ambient air. Although, with more feed-boards results in an increase in heat generated per tile from the LNA's, which could influence the rate in rise of internal temperature.

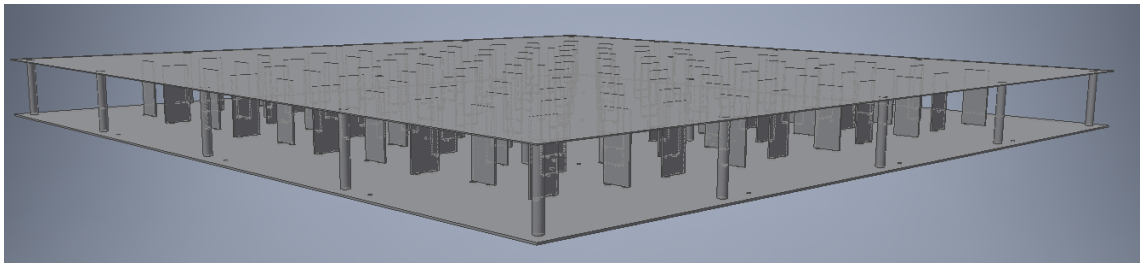

FIGURE 4.1: *The top-view of the fully fed DDA CAD model.*

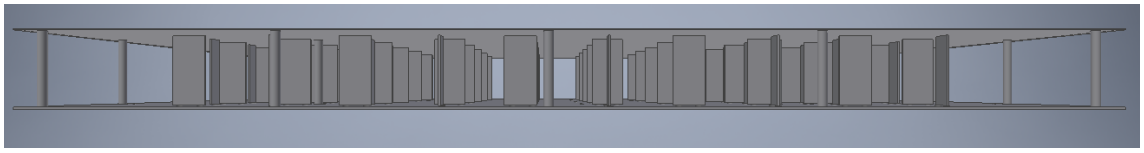

FIGURE 4.2: *The front-view of the fully fed DDA CAD model.*

4.2 DDA Heat Generation

The DDA is expected to dissipate thermal energy caused from internal heat generation during operation. When the array is powered, currents will flow through the electrical components and depending on power efficiency, some energy will be converted to heat. This is primarily due to resistance heating, where the electronics heat up because of slight inefficiencies in the electricity conducting components. From Assumption VII, it is stated that only heat dissipation from the LNA is considered as the other potential heat sources are considered to have a negligible effect or are of an unknown quantity.

Each LNA is planned to have a supply voltage of 3.3 V and draw a current of about 40 mA. The electrical power P of the LNA can therefore be calculated to be 132 mW from Equation 4.1. To ensure the maximum internal heat generation is considered during the analysis it is assumed that the total electrical energy from the LNA is converted to thermal energy, as this represents the extreme case. Therefore the LNA is considered as a heat source of 132 mW.

$$P = VI \tag{4.1}$$

When considering the integrated placement of the LNA, it is imperative that the distance between the feed-point and amplifier is as small as possible. As even the slightest increase in displacement can have an incredible influence in the amount of noise present in the system [51], [52]. For this reason there are only two potential placements for the LNA of each receiving element on the DDA. The first is to position the amplifier on the antenna layer itself right at the feed-point and the second is on the feed-board, as close to the antenna layer as possible.

From a thermal perspective the best placement will be the latter and is therefore recommended as this will provide a layer of protection to shield the LNA from direct sunlight. This will result in a lower exposed temperature as seen from the results attained during the experiment. For this thermal analysis the second option is considered as the first will be purely dependent on the temperature of the top plane.

The heat dissipated from the LNA will influence the temperature profile of the DDA and will need to be included in the thermal model. This is done by applying a uniform heat source equivalent to the electrical power of each LNA. The placement on the model is selected to be the three dimensional nodal element of the feed-board closest to the top plane representing the amplifier of each receiving element. To gather an understanding of the thermal influence from the LNA heat dissipation, a thermal simulation is run with the DDA at room temperature (23°C). A thermal image is shown in Figure 4.3 at steady state, with a resulting temperature increase of about two degrees from the LNA.

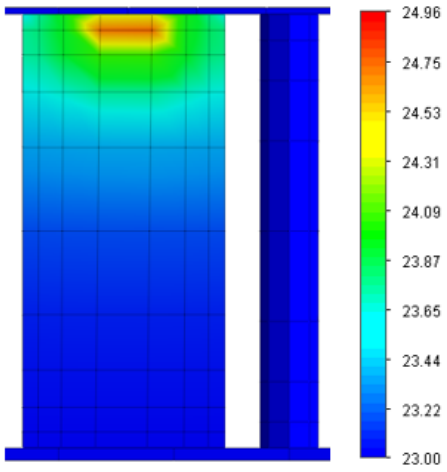

FIGURE 4.3: *Front-view thermal image of the LNA heat dissipation at room temperature.*

4.3 Operating Limits

The Karoo is a semi-desert natural region of South Africa and as a result often experiences harsh climates with high ambient temperatures and dry air. The primary research aim of this project is to evaluate the suitability of the DDA in this environment and determine if its desired level of performance can be achieved. This entails assessing the temperature dependent properties from §2.5, that govern the performance and operation of the DDA to determine whether they fall within the design operating limits whilst exposed to the climate of the Karoo.

4.3.1 LNA Temperature

The importance of the physical temperature of the LNA is discussed in §2.5.1 and is declared as the main consideration for the thermal analysis of the DDA. With so many factors of noise contributing towards the overall system temperature of the array, an LNA with the lowest possible noise temperature is required. Current developments have LNAs with measured noise temperatures of 20 K below that of the maximum set out for the MFAA at room temperature [15], [53]. Unfortunately though, without cooling the LNAs will often operate above room

temperature in the Karoo. This is further emphasized with the expression for sensitivity in Equation 4.2 [54]

$$\frac{A_e}{T_{sys}} = \frac{\eta_{rad}\eta_{ap}A_p}{\eta_{rad}T_{ext} + (1-\eta_{rad})\,T_p + T_{min}/\eta_n} \tag{4.2}$$

Where A_e is the effective area, T_{sys} is the system noise temperature, η_{rad}, η_{ap} & η_n are efficiency factors for beam radiation, aperture and noise matching respectively. Lastly, T_{ext} is the external noise temperature, T_p is the physical temperature of the antenna and T_{rec} is the receiver noise temperature. With the physical temperature having a direct influence on the system temperature, the lowest possible operating temperature of the LNA without forced cooling is desired for the MFAA. A maximum physical temperature for the LNA of the MFAA has been specified as 50°C in the *Antenna Array Manufacture related to the Development of a Mid-frequency Aperture Array* [19]. This temperature is considered the maximum physical temperature of the LNAs that will still meet the sensitivity requirements for the SKA. The amplifier for the DDA is yet to be integrated into the design and consequently specific operating limits of the LNA have not been determined. It is however safe to assume that by abiding by the required 50°C maximum, the array will perform as intended. This approach has also been implemented in the thermal analysis of the DDA counterparts, the *Vivaldi Array* and the *Octagonal Ring Antenna* [55], [56].

4.3.2 Temperature Stability

As mentioned in §2.5.2, the temperature stability of an antenna system can greatly impact the calibration procedure. A high variance in temperature will require consistent calibration to ensure signal quality but will translate into a more computationally expensive system [43]. Each of the elemental RF systems are subject to gain drift when exposed to changes in environmental temperature [6]. This influences the gain and phase of the system, which has to be accounted for in calibration. The rate in change of temperature is therefore considered an important factor in the thermal analysis of the DDA. The drastic changes in temperature in the transition from night to day and vice versa are desired to be as low as possible to improve the stability of the system. By mitigating the effect of external temperatures on the system the overall calibration stability of the MFAA will improve.

Another key factor for calibration is the difference in physical temperature between the LNAs across the DDA. If each LNA is operating at a different physical temperature and consequently so a different SNR, this can create complications during calibration decreasing likelihood of acceptable accuracy [42], [57]. This is unlikely to occur however, as the solar radiation and sky temperature effect is uniformly distributed and the DDA is fairly symmetrical but it is still a factor to consider during analysis. The method of calibration is also yet to be defined for the DDA and so a defined period between calibrations is still unknown. A 4°C/h rate in change of temperature is considered acceptable for the *Vivaldi Array* and on account of system similarities will be set as the goal for the DDA for this thermal analysis [55]. Although this parameter was tested under normal Karoo conditions and not the extreme conditions applied to the model, but provides a benchmark for what is to be achieved for acceptable operation.

4.4 Hot Day

As stated at the beginning of the chapter, the DDA is to be evaluated in the most extreme climate conditions it may experience during operation. Two thermal loads are created for this purpose that represent an extreme hot day and an extreme cold day. The recorded weather conditions at the SKA site of the ambient temperature and solar irradiance are each analysed to find the days with the maximum and minimum of both parameters. The day with the maximum ambient temperature is combined to that of the day with the maximum solar irradiance to form the thermal load of the hot day. This is similarly done with the minimum of each parameter to form the cold day thermal load. Although these days may not have existed in reality they represent the most extreme climate conditions and are plausible as each combination is done with days from the same time of year.

4.4.1 Conditions

The solar irradiance data is attained from values estimated every half-hour with satellite imagery from a *Meteostat Second Generation* satelite [58]. Three data types of the solar irradiance is provided depending on the location of measurement. These include the global horizon, clear-sky and top of atmosphere measurements. As this analysis assumes clear skies the clear-sky data is analysed to find the maximum value for the hot day simulation. The day with the highest solar irradiance is recorded during the summer period in December and reaches a peak of 1184 W/m^2 at 11:00. A graph of the solar irradiance over the period of the day that is applied to the hot day model can be seen in Figure 4.4.

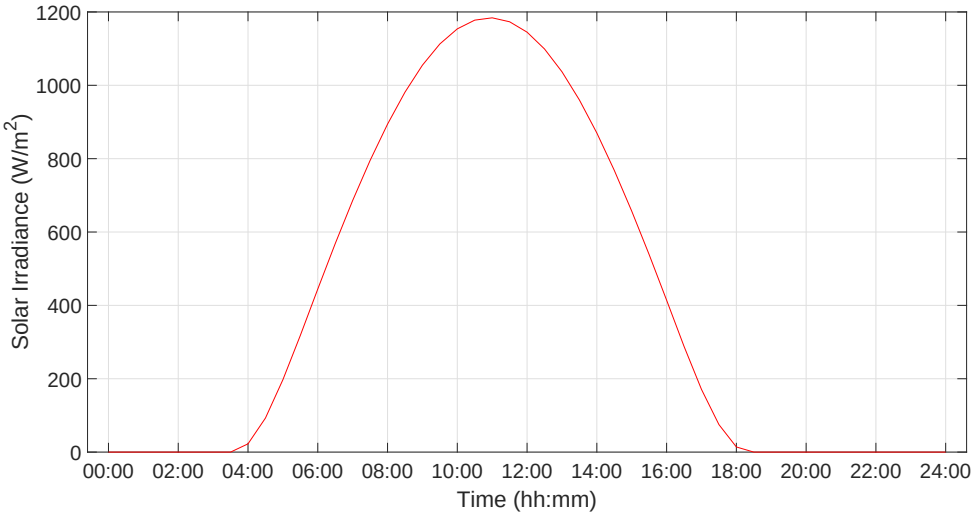

FIGURE 4.4: *Solar irradiance of the hot day.*

The day with the maximum ambient temperature is found in the *SKA physical characteristics annexure* [59], where measurements have been taken at ten minute intervals over a period of five years. This day also occurs in December and reaches a maximum of 40°C at 16:00. To remove noise from the measured data the ambient temperature is smoothed and is shown in Figure 4.5.

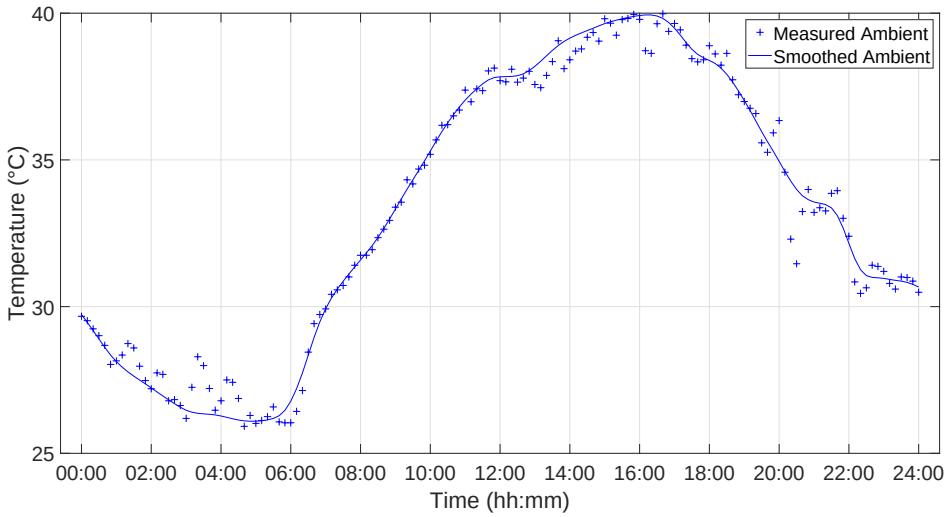

FIGURE 4.5: *Smoothed ambient temperature of the hot day.*

4.4.2 Results

With the conditions of the hot day determined, these are applied as dynamic thermal loads to the model generated in the previous chapter with the updated CAD geometry of the fully fed DDA. To provide the best chance for the DDA to maintain within the operating limits, the top surface is considered to be painted white to minimise the amount of radiant energy absorbed. The absorptance factor α is therefore set to that of typical white paint, 0.4 [60]. The CFD simulation is first run to simulate the fluid flow and heat transfer in the air. During this simulation the DDA is considered to be isolated with the surrounding faces open to the ambient air, as the spacing between each tile in a station configuration is currently unknown.

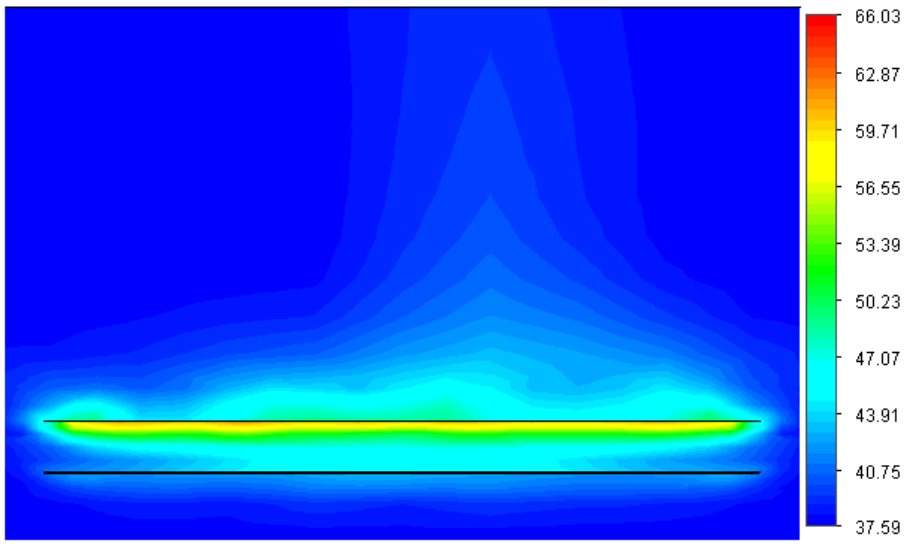

FIGURE 4.6: *The air temperature of the DDA on the hot day at 11:30.*

The contour plot of a clipping plane at the center of the array is shown in Figure 4.6. This describes the fluid temperature of the air surrounding the array during the hottest time of the day in °C. This is found to occur at around 11:30 with a peak air temperature of 66.03°C in

contact with the top plane of the array. From the plot it can be seen that there is a temperature build-up at the center of the DDA between the top and bottom planes during natural ventilation. Similarly there is also an increase in the air temperature below the ground plane.

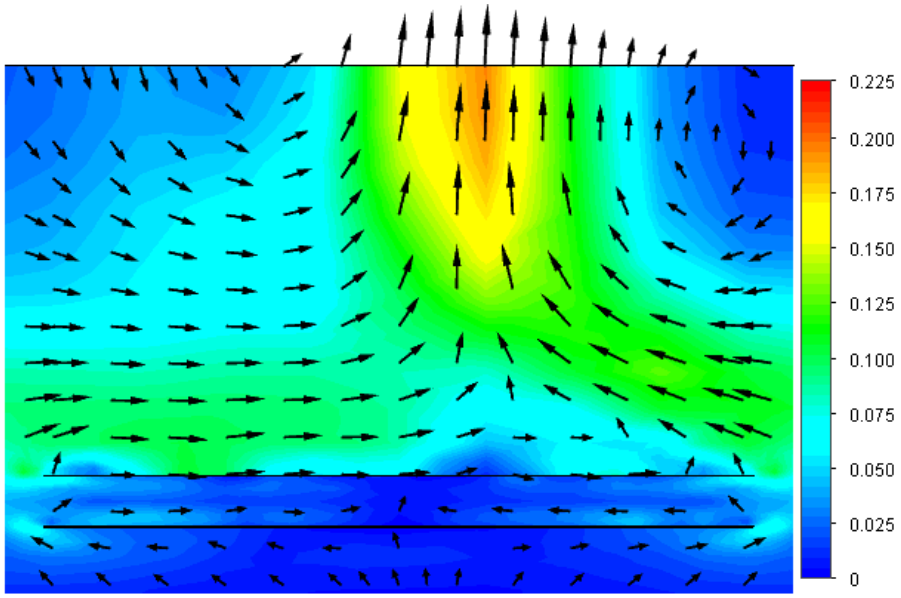

FIGURE 4.7: *The air velocity of the DDA on the hot day at 11:30.*

Figure 4.7 describes the velocity of the air surrounding the DDA in m/s. Here the buoyancy effects due to natural convection can be seen with the fluid velocity increasing with temperature. It can be noted that the air within and below the array has a very low velocity and as a result the temperature build-up is significant due to the low circulation rate. This is better seen with the plot of the variance of temperature inside and below the DDA shown in Figure 4.8, as the solar flux increases so does the air temperature from ambient.

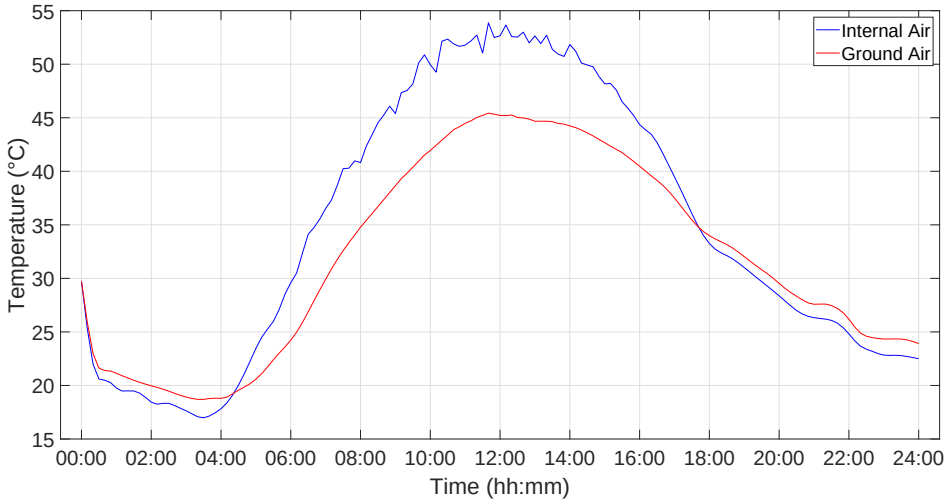

FIGURE 4.8: *Internal and ground air temperatures of the DDA during the hot day.*

With the results of the air temperatures surrounding the array, the FEA is performed with the applied thermal loads and initial temperatures set to ambient. A thermal image of the inside of the DDA at 11:30 is shown in Figure 4.9, where the temperature distribution between the

top and bottom planes can be seen. It is expected for the LNA to benefit from the low thermal conductivity of most of the components as the rate of conduction will be low between the top plane and feed-boards. But as a result of the temperature build-up of air within the array and its close proximity to the top plane the LNA temperature increases accordingly reaching a max temperature of 58.53 °C at around 12:00.

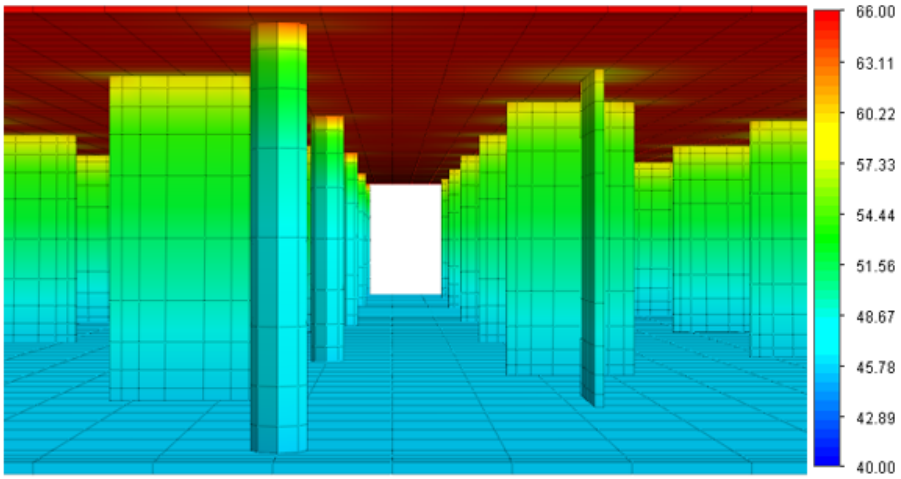

FIGURE 4.9: *The thermal image of the DDA during the hot day at 11:30.*

Table 4.1 and Figure 4.10 show the temperature change at the top plane, LNA and ground plane over the period of the hot day simulation. The temperature distribution during the night between the three temperatures is fairly small as the air is cooled from the sky radiation and sinks to the ground plane. This drastically changes as the sun rises and the top plane is exposed to sunlight. A maximum temperature change in time of 8.1°C/h is experienced by the DDA between 07:00 and 08:00 as the top plane begins to warm up.

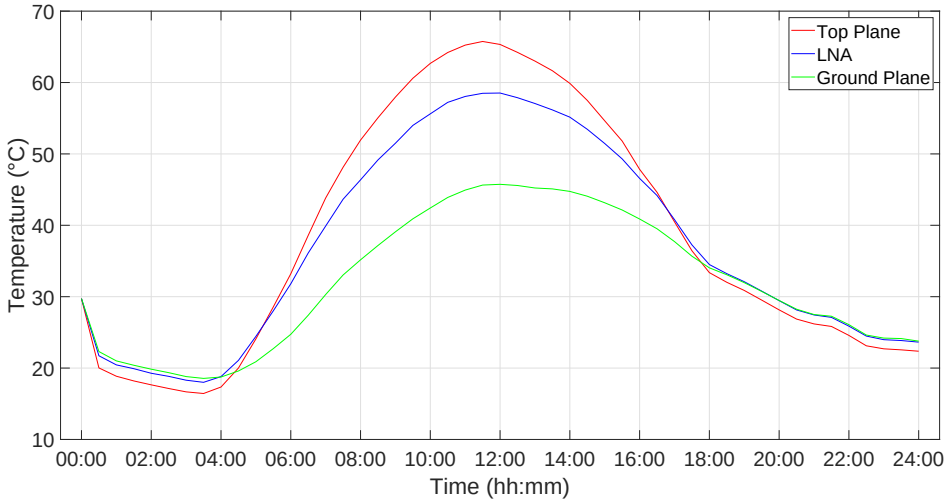

FIGURE 4.10: *Top plane, LNA and ground plane temperatures of the DDA during the hot day.*

	Temperature								
Time	00:00	03:00	06:00	09:00	12:00	15:00	18:00	21:00	00:00
Top Plane	29.73	16.67	33.20	57.96	65.33	54.64	33.37	26.19	22.36
LNA	29.73	18.30	31.80	51.50	58.53	51.46	34.50	27.44	23.63
Ground Plane	29.73	18.81	24.73	39.09	45.74	43.16	34.04	27.50	23.77

TABLE 4.1: *The temperature values (in °C) of the top plane, LNA and ground plane during the hot day.*

4.4.3 Discussion

The primary concerns for this thermal analysis as discussed in §4.3 is the maximum LNA temperature and the change in temperature per hour. From the simulation results of the isolated DDA during the hot day, a maximum LNA temperature of 58.53°C is predicted along with a temperature change of 8.1 °C/h. Both of these parameters fall outside of the required limits of 50°C and 4 °C/h and will have to be addressed later in the project. The effects of thermal stress on the DDA during the simulation are found to be non-impactful as no deformation occurs on the FEM model during the simulation, although this may change when analysed over a very long period of time. The consistency in temperature between each of the LNAs is considered acceptable as the temperature difference is found to be extremely small.

4.5 Cold Day

The cold day represents the coldest environment and is a combination of the days with the lowest ambient temperature and solar irradiance. Cold environments are better suited for LNAs as the thermal noise from the physical temperature will be minimal improving sensitivity. This simulation is therefore primarily run to determine the possible temperature changes that might occur during the transition from an extremely cold night to day and vice-versa.

4.5.1 Conditions

The solar irradiance of the measured data attained from [58] is analysed in the winter period to find the lowest acting solar irradiance at 11:00 when the sun is positioned at the zenith point. This day is found to only have a maximum solar irradiance of 574 W/m^2 and is recorded in June. It can also be noted that the solar irradiance has a shorter effect as the sun only rises at 06:00 and then sets at 16:00 shown in Figure 4.11.

The coldest ambient temperature recorded at the SKA site is found to be -3.77°C at around 03:00 from [59]. From the *Swinbank* formula this will result in a very low sky temperature that will induce night radiative cooling and expose the DDA to extremely low temperatures. The temperature change is therefore expected to be more severe than that found during the hot day analysis. Similarly to the hot day, the ambient temperature of the cold day is smoothed to remove noise and is shown in Figure 4.12.

4.5.2 Results

With the conditions of the cold day determined, these are applied as dynamic thermal loads to the model. Again, the CFD simulation is run first to simulate the fluid flow and heat transfer

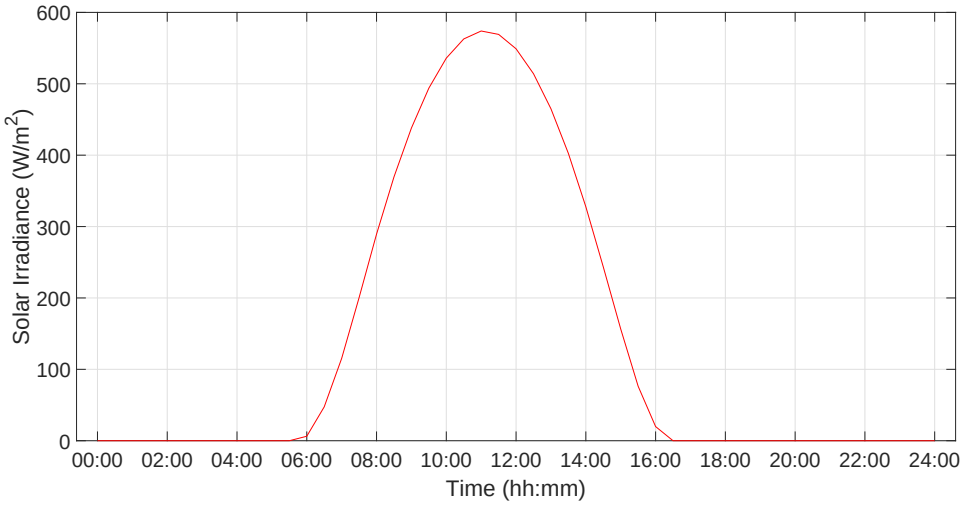

FIGURE 4.11: *Solar irradiance of the cold day.*

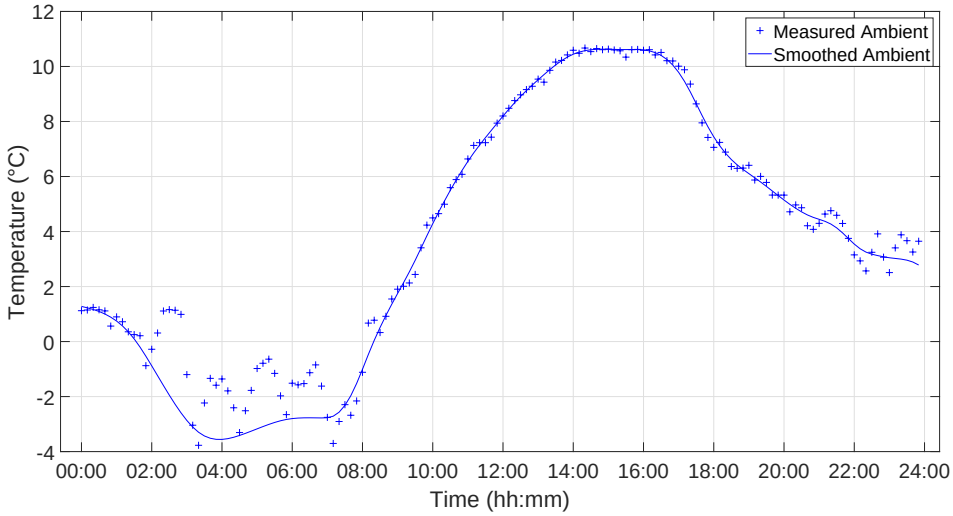

FIGURE 4.12: *Smoothed ambient temperature of the cold day.*

in the air during the cold day. The temperature build-up during the cold day is expected to be far less significant than that of the hot day but is still modelled as the heat transfer through the air impacts the temperature change in the DDA. The time of minimum temperature of the cold day is further analysed to determine the lowest temperatures the DDA may experience. The minimum air temperature is found at 04:00 with the fluid temperature distribution shown with a contour plot in °C in Figure 4.13.

From the figure it can be seen that the sky temperature greatly cools the DDA to the point where the ambient air temperature at night is the highest surrounding the array. As the top plane decreases in temperature the air near the top of the cavity is cooled and sinks to the ground plane. The night radiative cooling results in an air temperature of -18.8°C near the top surface of the array, 15.3°C colder than ambient. With such low temperatures the air particles contain very little energy and consequently move very slowly, this can be seen in Figure 4.14.

The temperature variation of the internal and ground air over the period of the cold day is shown in Figure 4.15. The air below the ground plane ranges from around -15 to 5 °C with a fairly

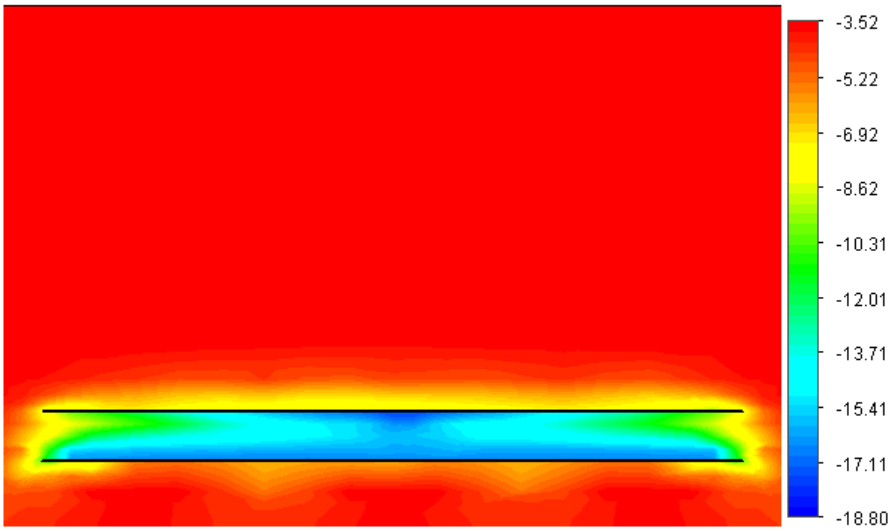

FIGURE 4.13: *The air temperature of the DDA on the cold day at 04:00.*

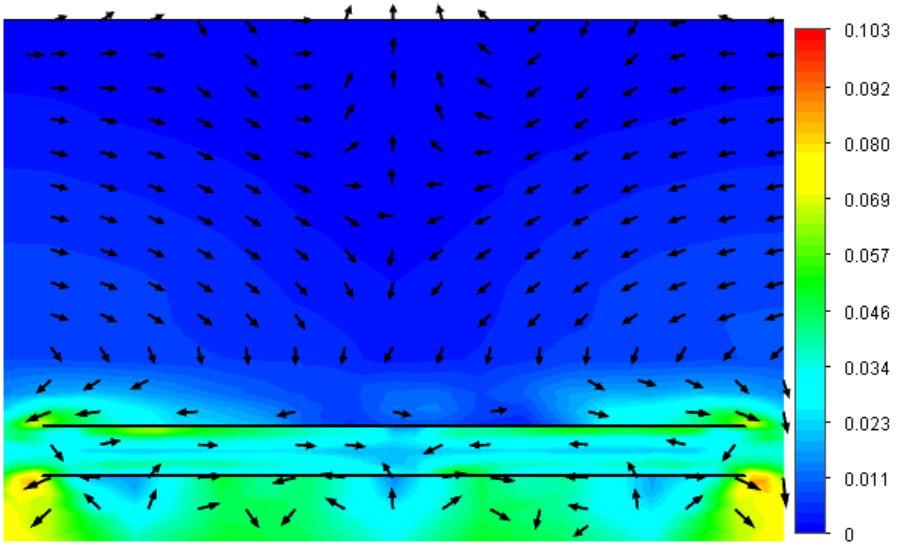

FIGURE 4.14: *The air velocity of the DDA on the cold day at 04:00.*

smooth transition when compared to the internal temperature. The small sporadic changes in the internal air temperature seen in the figure can be accounted to the air circulation as a result of the temperature difference between the top and bottom planes.

After applying the resulting air temperatures to the FEA model together with the thermal load, a thermal image of the DDA is attained in Figure 4.16. This image is shown at the time step of 04:00 where there is a small temperature difference between the top and bottom planes. The LNA drops to a temperature of -16.3°C during this time but as a result experiences a drastic increase in temperature as the sun begins to rise. This can be seen in Figure 4.17, which provides the temperature change of the top plane, LNA and ground plane over the course of the cold day simulation.

As mentioned earlier the main purpose of this simulation is to determine the temperature change during the transition from night to day and vice-versa. As with low ambient temperatures results in significant night radiative cooling. From Figure 4.17 a steep increase in temperature is seen

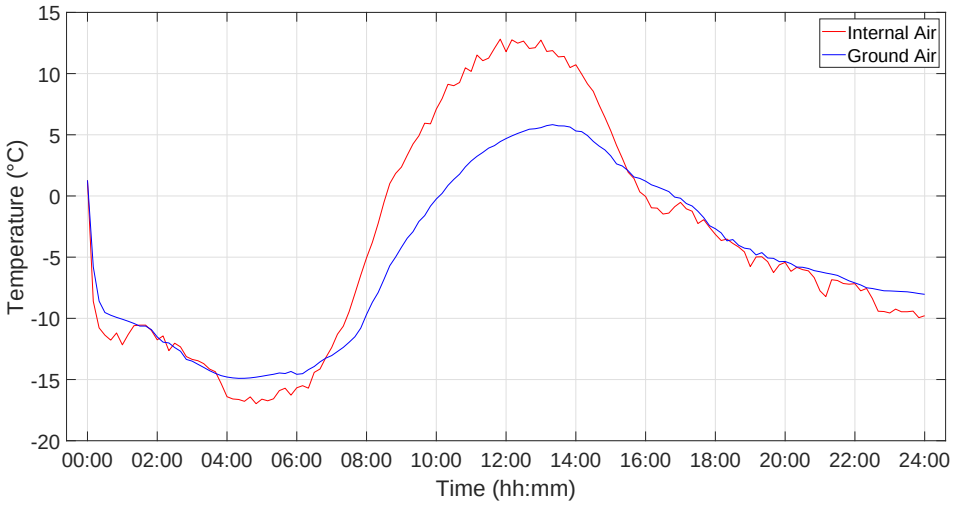

FIGURE 4.15: *Internal and ground air temperatures of the DDA during the cold day.*

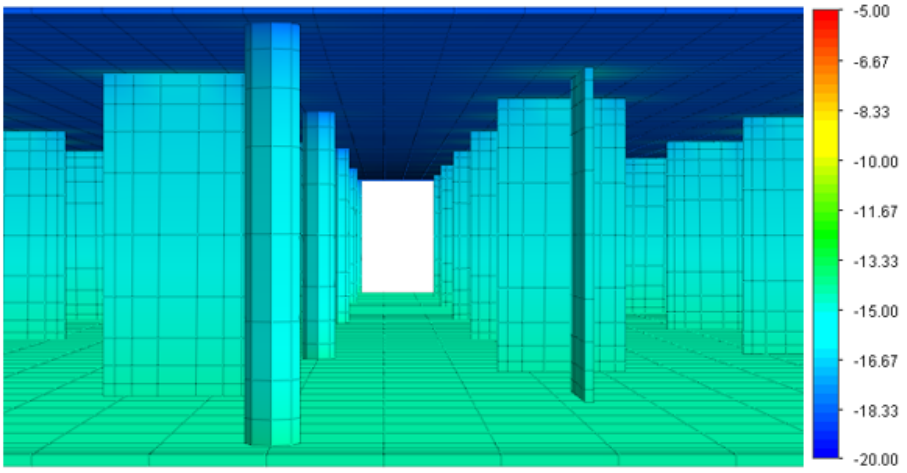

FIGURE 4.16: *The thermal image of the DDA during the cold day at 04:00.*

between 06:00 and 12:00. This increase results in a temperature change experienced by the LNA of 9.4°C between 07:30 and 08:30. As expected this is a larger temperature change than that found during the hot day simulation. Table 4.2 provides the temperature values at three hour intervals over the course of the cold day.

	Temperature								
Time	00:00	03:00	06:00	09:00	12:00	15:00	18:00	21:00	00:00
Top Plane	1.28	-17.04	-17.85	7.02	17.57	5.44	-5.82	-9.75	-11.66
LNA	1.28	-14.28	-15.42	5.34	14.99	6.26	-3.41	-7.49	-9.37
Ground Plane	1.28	-13.67	-14.60	-2.71	5.76	3.63	-2.68	-6.35	-8.20

TABLE 4.2: *The temperature values of the top plane, LNA and ground plane during the cold day.*

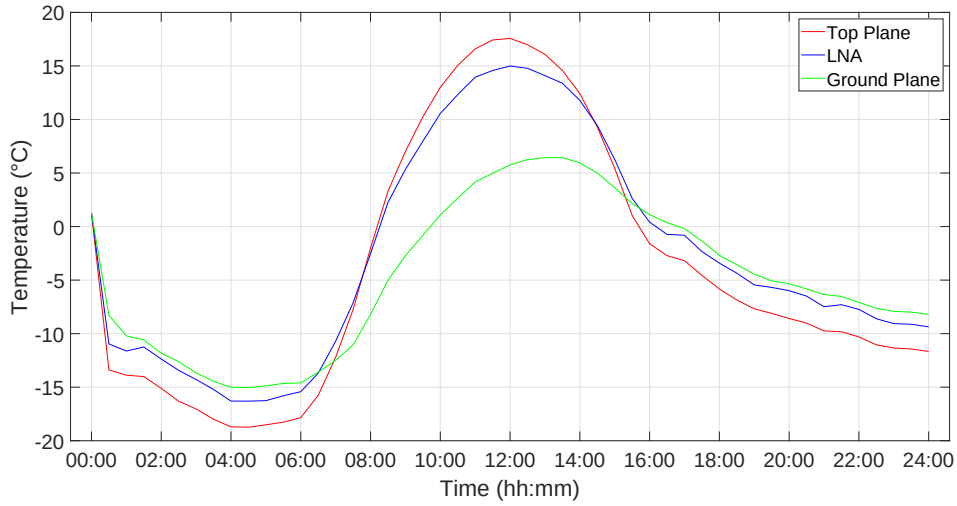

FIGURE 4.17: *Top plane, LNA and ground plane temperatures during the cold day.*

4.5.3 Discussion

The cold day simulation represents a non-critical case with regards to the physical temperature of the LNA during operation. However, the change in temperature per hour is found to be more severe in this simulation and likewise does not remain within the temperature operating limits. After the sun sets the heat inside the array appears to dissipate fairly quickly as the temperature between the three measured locations reforms back to that seen between 00:00 and 06:00.

4.6 Conclusion

This chapter was devoted to simulating the thermal response of the DDA in two extreme environmental conditions over the period of a day to evaluate its suitability in the Karoo. This was performed on the updated CAD geometry of the DDA that represents the current final product for deployment and with defined operating limits required for the DDA to achieve. In the hot day analysis it was found that the LNA reached a peak temperature of 8.53°C higher than the desired limit and with a temperature change per hour double of that which is deemed acceptable. The cold day analysis is considered a non-critical case for the physical temperature of the LNA but resulted in a worst temperature change per hour. The isolated DDA fails to meet the desired operating limits for the Karoo and therefore a thermal solution is required.

CHAPTER 5

Enclosure Design

Contents

This chapter is devoted to developing and testing a thermal solution for the DDA when operating in the Karoo that utilises natural convection cooling to mitigate the impact of the environment on the array. The chapter opens in §5.1 with a discussion of what is required of the thermal solution and an overview of an enclosure design concept generated for this project. §5.2 covers the detailed design of the enclosure with the material selection and the design traits necessary for the DDA to remain below critical temperatures. The focus then shifts in §5.3 to the thermal model of the enclosed DDA and the results attained when simulated in the hot and cold day conditions of the previous chapter. A conclusion is then provided in §5.4 on the thermal improvements achieved by the enclosure.

5.1 Thermal Solution

From the results of the thermal simulations performed in the previous chapter it was concluded that a thermal solution is necessary to bring the critical operating parameters of the DDA within their desired limits. As no cooling equipment can be implemented to assist with decreasing the temperature of the LNA, another approach is necessary. By analysing the results of the hot and cold day simulations run on the DDA it can be seen that the LNA temperature is influenced by its close proximity to the top plane that is in contact with direct sunlight; and the temperature build-up of the air within the cavity of the array. An enclosure is proposed to

mitigate these effects and improve the temperature profile of the DDA such that it will meet desired performance when in the Karoo.

5.1.1 Design Goals

The following design goals for the enclosure have been established to ensure an acceptable thermal solution for the DDA.

I The two primary sources of heat transfer include the heating from solar irradiance and the cooling from the night sky. Both of these act directly on the top plane of the DDA and thereby the enclosure is required to provide the proper shielding to negate their thermal impact.

II Multiple ports to the feed-boards of the DDA are situated at the bottom of the ground plane for connection. It is important that access to these are not obstructed by the enclosure.

III It's intended for the MFAA to be comprised of an extremely large quantity of array tiles and therefore suitable accessibility will need to be achieved when in a station configuration for maintenance and replacement purposes.

IV The enclosure will need to be capable of providing close positioning between each of the array tiles as to form an array station and is required to be elevated a height of 1∼1.5 m off the ground.

V The sheer size of the MFAA and the necessity of minimising budget expenditure and technical complications requires that the enclosure be of an affordable cost, with the potential of mass production and a simple assembly process (keep the design flat).

VI The effect of the enclosure on the electromagnetic performance of the DDA will need to be kept at a minimum as to not hinder the operation of the array.

VII Additional electronic components such as the beam former and beam combiner electronics are intended to be positioned below the ground plane of the DDA and will have to accounted for in the design of the enclosure.

5.1.2 Design Concept

A suitable enclosure that will meet the set out design goals requires three essential components. The first being a cover that will provide protection from direct sunlight during the day, and radiative cooling during the night. Support beams to elevate the DDA off the ground to enable access for maintenance and space for additional electronics. Lastly, an appropriate surface component for the DDA to rest on that doesn't obstruct cable access to each of the ports and allows for the removal of an individual DDA tile. An initial design concept has been created and is comprised of these three essential components to determine the potential effect an enclosure may have on the DDA from a thermal perspective.

The design for each of the components has been created and assembled in *Autodesk Inventor Professional* to form the enclosure. This initial design provided a framework to determine the required enclosure features necessary for the DDA to perform within its operating limits. Further optimisation from a mass production and structural analysis standpoint will be required

in future-work to attain a final enclosure acceptable for deployment. The CAD geometry of the optimised isolated enclosure can be seen in Figure 5.1 and with the installed DDA in Figures 5.2 & 5.3.

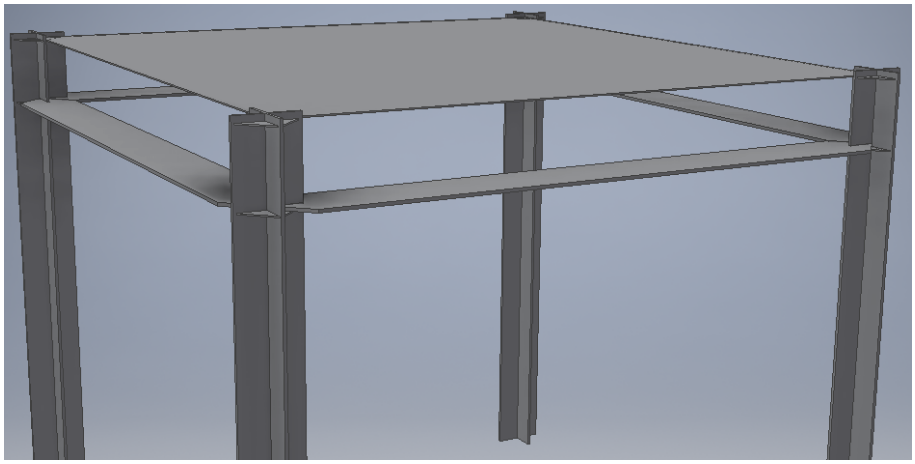

FIGURE 5.1: *The CAD geometry of the assembled enclosure.*

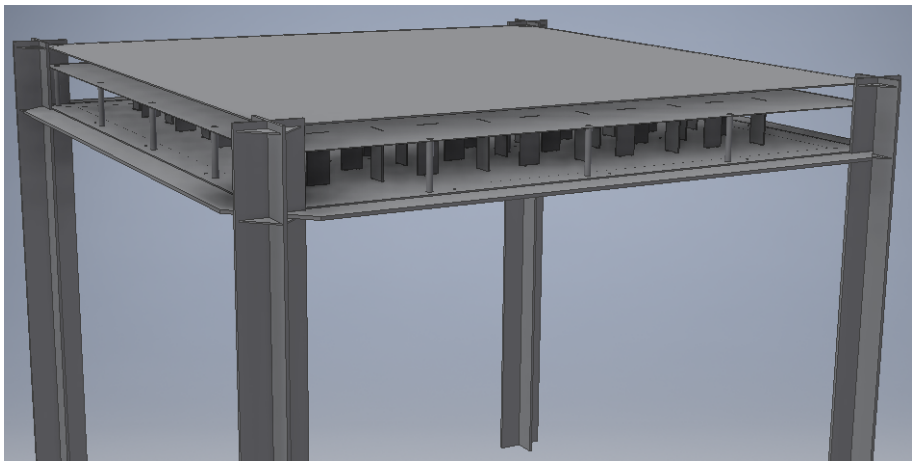

FIGURE 5.2: *The top-view of the CAD geometry of the enclosure with the DDA.*

A strength of the DDA when compared to other aperture array topologies is its flat design and open air cavity between the top and bottom planes. Not only does this improve production and reduce costs but can potentially assist with temperature stability as a large surface area is exposed to ambient air, and will therefore be strongly influenced by convection. When considering this and the fact that the DDA will only depend on natural ventilation to circulate the air within and below the array an open enclosure design is favoured. This will provide an escape for the air to travel and allow wind to pass through the components of the array, improving circulation. A CFD simulation is performed to gather an understanding of the effect of wind on the temperature of the isolated DDA, and how allowing wind to pass through will be beneficial. The simulation is performed during the peak temperatures of the hot day analysis, such that a comparison can be made between the maximum acting temperatures on the DDA at varying wind speeds. A flow condition for the air velocity is set to vary from 0 to 10 m/s in the x-direction with the constant thermal load of the hot day analysis set to the conditions at 12:00. Figure 5.4 shows the results from the simulation of the top plane temperature.

Here it can be seen that as the wind speed increases, the physical temperature of the top plane

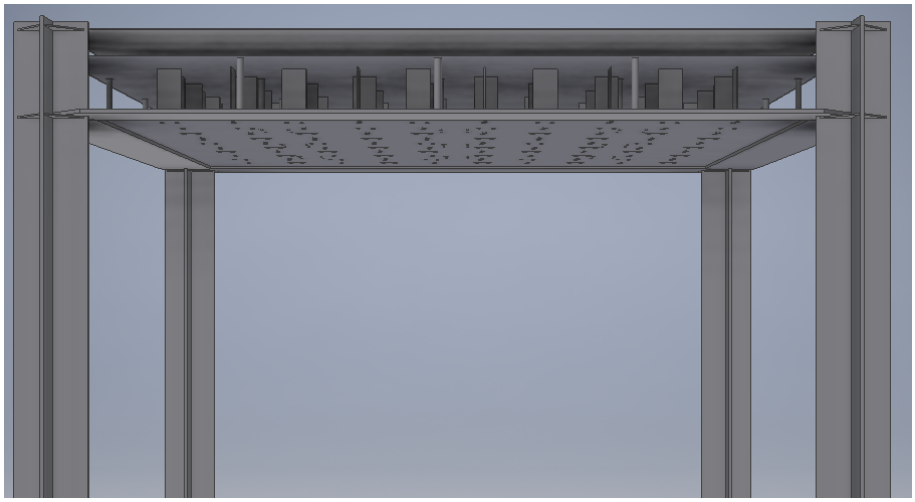

FIGURE 5.3: *The front-view of the CAD geometry of the enclosure with the DDA.*

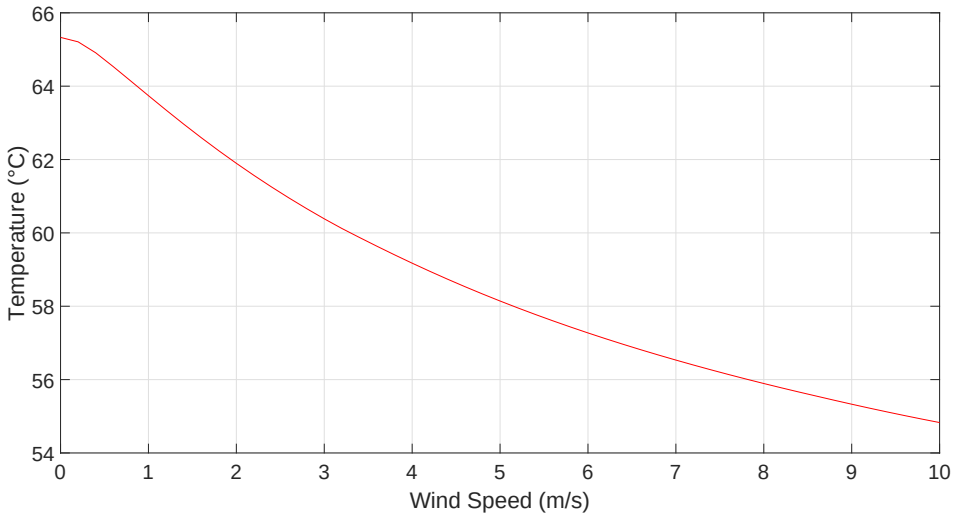

FIGURE 5.4: *Peak top plane temperature of the DDA with wind speed.*

decreases, this can be explained by three factors. With wind, the air within and around the array experiences an increase in flow rate and as a result the internal air circulates much faster than it would when under natural convection. This prevents the temperature build-up of air that rises to the top plane as it is constantly replaced with freshly circulated ambient temperature air. The bulk motion of fluid also heavily influences the rate of convective heat transfer as the *Reynolds* number R_e that represents the ratio of inertia to viscous forces depends on the fluid velocity shown in Equation 5.1 [22].

$$R_e = \frac{\rho V L}{\mu} \tag{5.1}$$

Where ρ is the density of the fluid (in this case air), V is the fluid velocity, L is the length of the plate and μ is the fluid viscosity. A faster flow rate of air will result in an increased *Reynolds* number and consequently an increased heat transfer coefficient improving the rate of convective heat transfer. Lastly, with a large surface area exposed to ambient air and from Equation 2.2, the temperature of the array decreases as it is cooled by the ambient air.

The hottest part of the DDA incurs a temperature drop of 4.33°C at 2.5m/s, which has been recorded as the average wind speed at the SKA site [59]. Therefore utilising this natural cooling component with an open enclosure can benefit the performance of the DDA. With open sides and the large surface area of the feed-boards exposed to ambient air, the overall temperature of the LNA will benefit from an improved rate of heat transfer with the ambient air and a faster circulation rate. An open enclosure also reduces the amount of material that would be required when compared to a closed enclosure, assisting with the costs and manufacturing time required for implementation.

5.2 Detailed Design

The initial concept of the enclosure has been designed with four support beams, four surface components and a cover. The approach was to provide unobstructed access to the base of the array for connectivity whilst still allowing the enclosure to interlink with additional enclosures to form an array station. Each support beam is planned to be split amongst four DDA tiles with the surface component interlinking each DDA with a gap of 5 mm. It is intended for each tile to be accessible from the base of the enclosure with the re-movability of the surface components. The design traits of the enclosure will determine the physical temperature of the LNA when operating in the Karoo. These will need to be tested and optimised such that the DDA will remain within the desired limits, while considering the impact on the electromagnetic performance.

5.2.1 Material Selection

Of the three components of the enclosure, the most important is the cover as this is required to adequately protect the DDA from the environmental conditions with minimal impact on the electromagnetic performance. The cover is intended to be placed over the array in the path of signals. This can introduce insertion losses of the incident wave as it will have to propagate through the cover material and as a result lose energy [61]. Two sets of properties of potential cover materials are therefore evaluated during selection and include the thermal properties together with the dielectric properties. A substance of good dielectrics coupled with high thermal resistance characterise the behaviour of a suitable cover.

When a wave propagates through a material, power losses will be incurred due to some electrical energy being stored and then dissipated through charge migration or as thermal energy [62]. In order to obtain a cover without impairing the performance of the DDA, the material will essentially have to be electrically invisible to the antenna. Dielectric materials have the best chance of achieving this as they are a class of insulating substances that are weak conductors of electricity. This entails that they have minimal signal dissipation and attenuation on account of their low dielectric constant and loss tangent. This can be further expressed by the characteristic impedance of the cover material and the resulting reflection coefficient. This parameter represents how much of the electromagnetic wave is reflected back by an impedance discontinuity in the transmission medium, which in this case is the cover. The reflection coefficient can be determined from the intrinsic impedance of free space and the dielectric material as follows [61].

$$\eta_0 = \sqrt{\frac{\mu_0}{\varepsilon_0}} = 377\Omega \tag{5.2}$$

$$\eta_r = \sqrt{\frac{\mu_0}{\epsilon_0}}\sqrt{\frac{\mu_r}{\varepsilon_r}} = \frac{377\Omega}{\sqrt{\epsilon_r}} \tag{5.3}$$

$$\Gamma = \frac{\eta_r - \eta_0}{\eta_r + \eta_0} \tag{5.4}$$

Where ε_0 & ε_r are the permittivity of free space and the relative permitivity of the dielectric material respectively, μ_0 & μ_r are the permeability of free space and the relative permeability of the dielectrictric material respectively and finally Γ is the reflection coefficient. From Equation 5.4 it can be seen that selecting a material with a low dielectric constant will result in a reduced amount of reflections in the signal thereby reducing the impact on the radiation pattern of the antenna [63]. The loss tangent is also considered as this indicates the measure of power loss to total transmitted power.

When considering the thermal properties of the material, the primary concern is how well it can reduce the heating effect of solar radiation. This requires a low absorptance such that most of the sunlight is reflected from the material to reduce the temperature build-up of air between the cover and DDA. This can be achieved with a white material substance of a low thermal conductivity that isn't susceptible to temperatures up to 70°C. A material with a high UV resistance will be beneficial, although substances with added UV-stabilisers generally increase loss. After researching multiple cover materials, three have been selected on account of their properties, availability and pricing and include polypropylene (PP), acrylonitrile butadiene styrene (ABS) and polyvinyl chloride (PVC). These properties are chosen as they each have ideal thermal properties with a low absorptance of 0.31 when white [60] and are good dielectric materials. Each material is also readily available and is capable of being manufactured into a cover for the enclosure. Table 5.1 provides the thermal properties and resulting temperatures of each of the materials that are evaluated by performing a simulation on the isolated cover with the extreme temperature pre-load of the hot day analysis at 12:00.

Property	**Density** kg/m^3	**Conductivity** W/mK	**Specific Heat** J/kgK	**Emissivity**	**Temperature** $°C$
PP	905	0.22	1920	0.97	51.96
PVC	1400	0.16	1000	0.91	52.23
ABS	1050	0.25	1423	0.92	51.75

TABLE 5.1: *Thermal properties of the potential cover materials.*

As each material has fairly similar thermal properties the resulting temperatures only deviate slightly to the point where the material can be chosen on account of its dielectric properties. These are shown in Table 5.2 where it can be seen that polypropylene has the best relative permittivity and loss tangent. This material is chosen as the cover of the enclosure and is used in the further analysis of the DDA as it will have the smallest impact on the performance of the array and should be capable of providing adequate protection from the environmental conditions of the Karoo.

The material selection of the support beams and surface components have minimal influence on the resulting temperature profile of the array as the thermal conductivity of the array components is very low apart from the aluminium ground plane. The materials are therefore selected based on a structural integrity standpoint and for manufacturing where the beams are chosen as steel and the surface components are aluminium.

Material	Permittivity	Loss Tangent
PP	2.2	0.0003
PVC	3	0.1
ABS	2.4	0.005

TABLE 5.2: *Dielectric properties of the potential cover materials.*

5.2.2 Cover Thickness

Besides the dielectric constant and loss tangent, the thickness of the cover will also influence the impact on antenna performance as this will contribute towards its radio frequency transparency. To minimise the effect on performance, the polypropylene will have to be made electrically thin [64]. This entails setting the thickness of the cover to less than 0.1λ such that waves can propagate through with minimal insertion losses.

$$\lambda = \frac{c_0}{f} \tag{5.5}$$

Due to the fairly low frequency of the MFAA this is not incredible hard to achieve as shown by Equation 5.5 to calculate wavelength λ, where c_o is the speed of light and f is frequency [61]; the wavelengths range from 0.6 to 0.2 m. Therefore a suitable cover thickness should be attained to produce good RF performance with high transmission. At this thickness, the signal reflections that occur at the boundary between the cover and free space should be cancelled out by the out-of-phase reflections from the boundary on the other side of the material [65]. The cover thickness is chosen to be 0.01λ at the highest operating frequency which translates to 2 mm as this should provide enough structural integrity for the enclosure and be electrically thin to the array. The effect of the enclosure on the electromagnetic performance is evaluated in the following chapter.

An additional benefit of polypropylene is its inherently hydro-phobic properties. This is important as water can act as a shield to RF transmissions due its high dielectric constant and loss tangent. In the event a layer of water rests upon the cover, the thin film will result in significant signal attenuation [66]. Although with polypropylene this will be less likely to take place as water is naturally repelled from the surface.

5.2.3 Cavity Size

The distance between the cover and top plane of the DDA has to be optimised to ensure the LNA will remain below 50°C with the smallest gap possible. A bigger gap will result in more required materials for the enclosure and therefore a more expensive deployment cost of the DDA. The gap size that will ensure the LNA remains below 50°C will depend on the heat flow rate into the air and the ventilation of the system. The following expression (Equation 3.12 with respect to time) explains this relationship as with a higher volume of air, the more mass of air, the longer it will take for the temperature inside the cavity to build-up.

$$W = mC_p\Delta T/s \tag{5.6}$$

Here, W is the heat flow rate into the air in Watts and s is time in seconds. To accurately model the increase in air temperature whilst taking into account ventilation to determine the minimum

necessary gap size, a parametric study is performed with CFD. This is done by modelling the DDA below a cover with a symmetry boundary condition surrounding the array and only considering natural ventilation. As the DDA is intended to be surrounded by additional DDA's when in a station, it can be said that no heat transfer will occur between each tile on account of symmetry and uniformly distributed loads. To model this, *lids* are placed on the sides of the DDA with an adiabatic condition and the faces are set to non-radiating surfaces. A gap of 2.5 mm is accounted for between each DDA for air to escape as this is how the enclosure has been designed. The effect of the surface that supports the DDA when in the enclosure is not considered as this is positioned below the ground plane and will have no influence on the increase in air temperature. The parametric study is performed by varying the distance between the cover and top plane until the top plane drops below 50°C at convergence during the hottest conditions of the hot day simulation. By designing for the top plane surface of the array to have a maximum of 50°C, the LNA will safely operate under acceptable conditions. The results of the parametric study are shown in Figure 5.5.

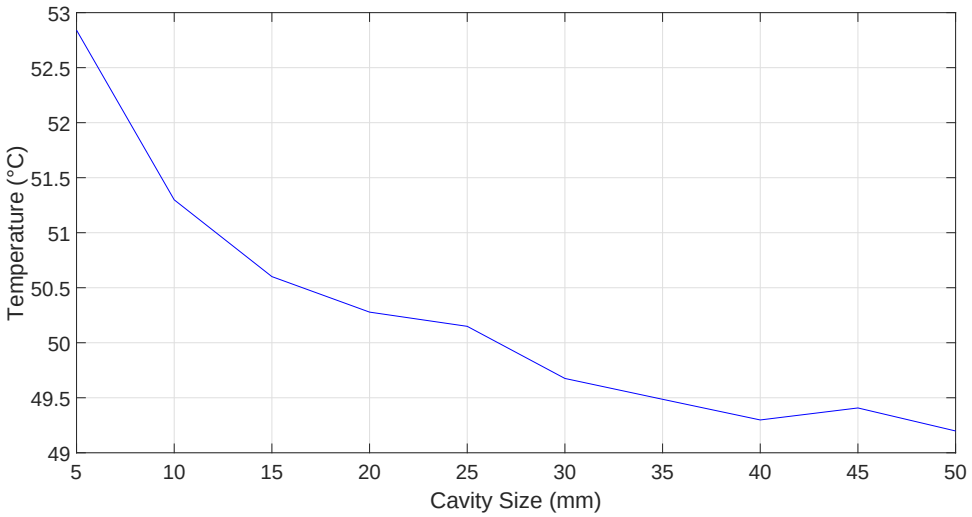

FIGURE 5.5: *Resulting temperature of the top plane with increasing cavity size.*

It can be seen that as the size of the cavity increases, the acting temperature on the top plane of the array decreases. A cavity size of 35 mm is chosen for the enclosure as this will allow the LNA to operate safely under acceptable conditions and assist with preserving the condition of the antenna layer of the DDA. Although the smallest gap size may not be used after further modifications, it does provide the benchmark for what is applicable to still achieve the desired performance of the DDA.

5.3 Thermal Model

With the enclosure design developed and optimised, the simulations that model the DDA in two extreme environments are repeated to analyse the potential improvement of the operating temperatures. This follows the same procedure described in Chapter 4 by applying the appropriate thermal loads of the heat transfer processes taking place in Figure 5.6 on the CAD geometry of the DDA with the enclosure. Although here the DDA is considered to be in a station configuration and as such does not have open sides exposed to ambient air but rather a symmetry boundary condition as described in the previous section. After each of the material properties

have been applied to the corresponding component and the contact surfaces defined at each of the connecting faces, the hot day and cold day simulations are performed.

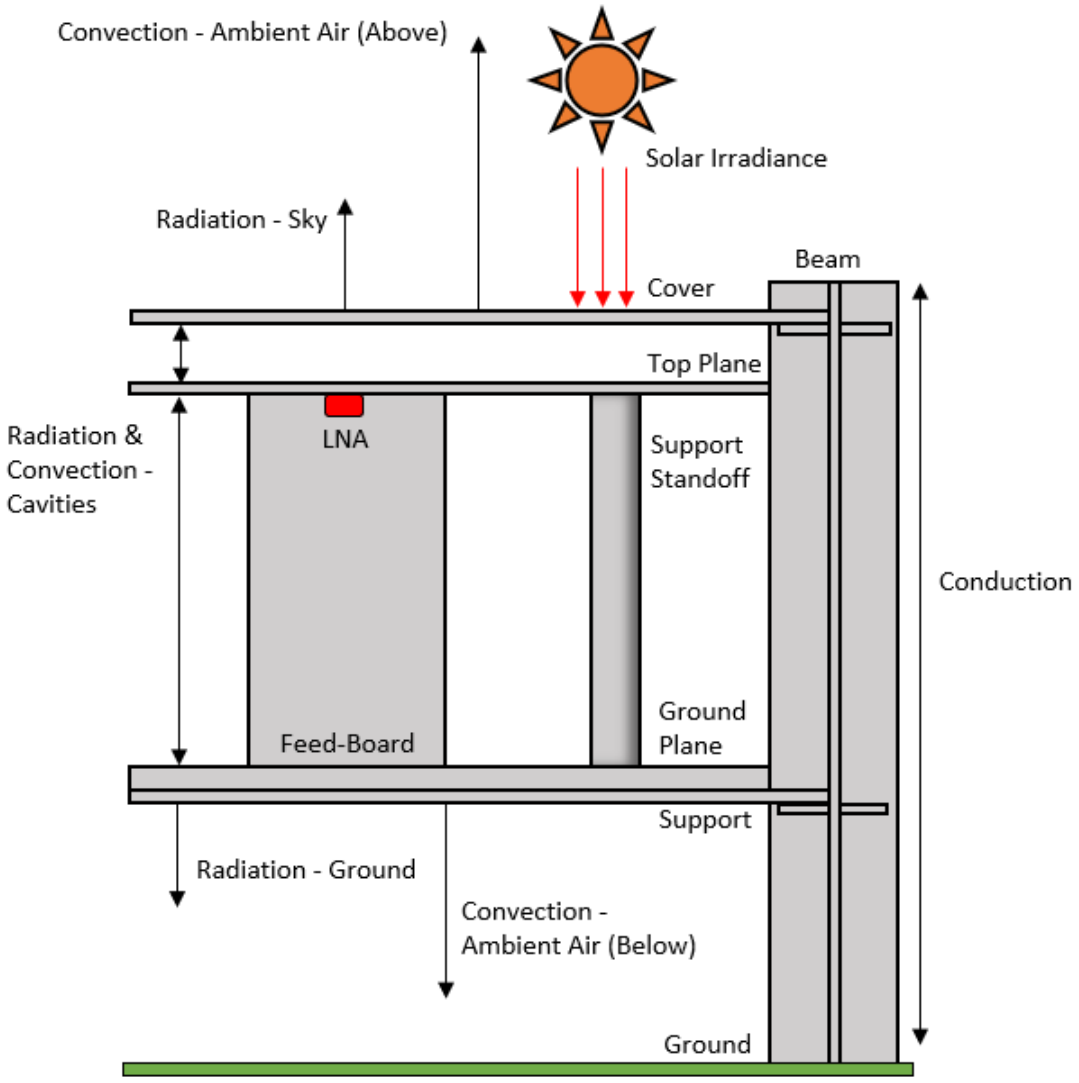

FIGURE 5.6: *Thermal schematic of the enclosed DDA displaying the acting heat transfer processes.*

5.3.1 Hot Day

The following results are attained after applying the conditions of the hot day from §4.4.1 to the enclosure model and running the simulation in a transient analysis over the twenty-four hour period. A contour plot of the temperature distribution of the air inside and around the enclosure is shown in Figure 5.7 at 12:00. Here the temperature rise of the air inside and below the array is at a maximum. It can be seen that the increase in air temperature between the cover and top plane is far more severe than the internal air temperature of the DDA, and by providing an additional layer has consequently improved the DDA's thermal response under extreme conditions. As the heat rises the hot air in the top cavity is allowed to escape around the edges of the array, preventing a critical temperature build-up.

The variation of the center temperature in the cavity and the ground air temperature have been

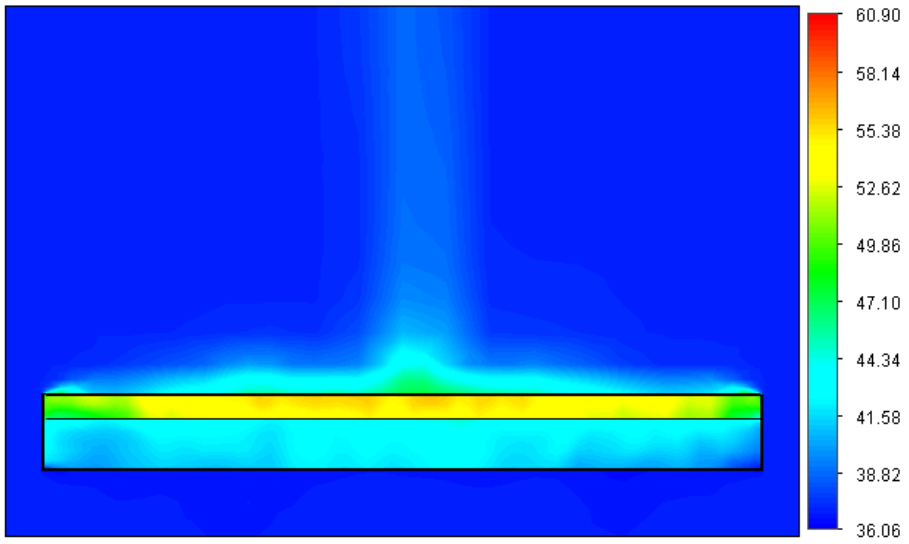

FIGURE 5.7: *The air temperature of the enclosed DDA during the hot day at 12:00.*

plotted over the course of the day in Figure 5.8. When compared to the results obtained from the isolated DDA analysis, the air in the enclosure has experienced close to a 10°C drop in temperature greatly improving the chances of the LNA to operate within acceptable conditions. The internal air is also more stable and should assist with the drastic temperature change during the transition from night to day and vice-versa.

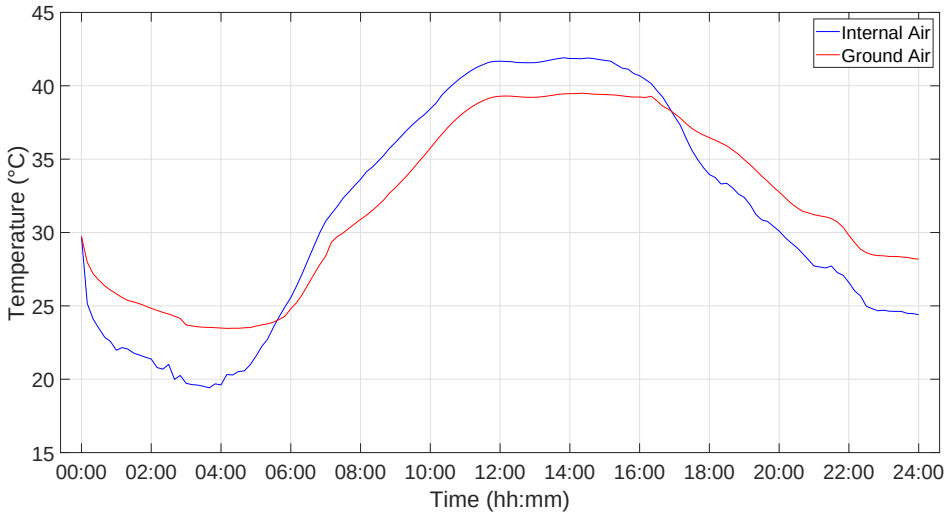

FIGURE 5.8: *Internal and ground air temperatures during the hot day.*

With the air temperatures obtained and applied to the FEA model the resulting temperatures of the DDA with the enclosure are determined. A thermal image of the enclosure is shown in Figure 5.9 where it can be seen that the cover greatly reduces the overall temperature of the array. This is furthered by the low absorptivity of the polypropylene as the maximum temperature experienced by the cover reaches 60.74°C, about 5°C less than the isolated DDA. This is further expressed in Figure 5.10, with the variation of the temperatures of the cover, LNA and ground plane over the course of the hot day.

The physical temperature of the LNA when protected by the enclosure reaches a maximum of

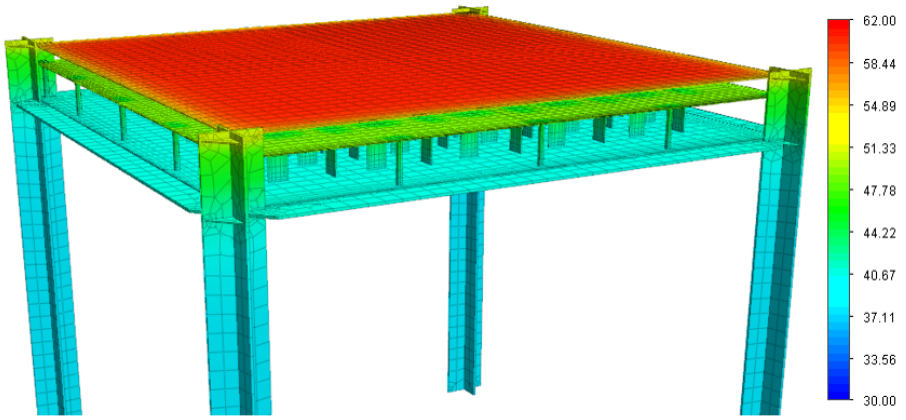

FIGURE 5.9: *The thermal image of the enclosed DDA during the hot day at 12:00.*

45.14°C at 12:00 during the hot day analysis. This is a significant improvement and enables the LNA to operate under acceptable conditions. With a lower physical temperature, the LNA will experience less receiver noise temperature, bringing the MFAA one step closer to achieving a 40 K maximum array noise temperature [15]. The results also show an improvement in the temperature stability of the LNA with a maximum change in temperature of 5.65 °C/h between 06:00 and 7:00 in the morning. Although this is over the operating limit, the hot day conditions represent the worst possible environment the DDA may experience and as such the ambient temperature alone reaches a change of 4°C/h at this time. Therefore this level of stability is expected under ordinary Karoo conditions, which the enclosure should achieve. Table 5.3 provides the temperatures of the cover, LNA and ground plane at three hour intervals over the course of the hot day.

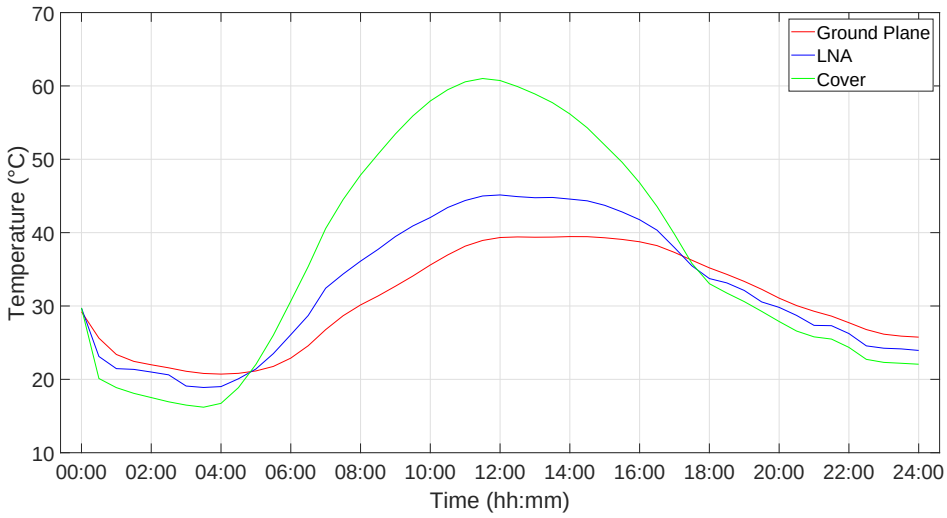

FIGURE 5.10: *Top plane, LNA and ground plane temperatures during the hot day with the enclosure.*

The results of the hot day analysis for the enclosure have shown a sufficient improvement in the LNA temperature and stability. Providing a cover capable of reflecting majority of the sunlight with high insulative properties has restricted a critical temperature build-up in the DDA and allowed better functionality. With lower sustained temperatures, the DDA should experience less thermal stress and therefore a longer lifetime that will ultimately assist with expenditure and consistent performance.

	Temperature								
Time	00:00	03:00	06:00	09:00	12:00	15:00	18:00	21:00	00:00
Cover	29.73	16.49	30.66	53.45	60.74	51.94	33.04	25.79	22.06
LNA	29.73	19.09	26.08	39.47	45.14	43.72	33.74	27.36	23.94
Ground Plane	29.73	21.10	22.89	32.70	39.33	39.30	35.20	29.28	25.75

TABLE 5.3: *The temperature values (in °C) of the top plane, LNA and ground plane during the hot day with the enclosure.*

5.3.2 Cold Day

To understand the effect the enclosure might have on the DDA in cold environments, the cold day simulation is run with the conditions from §4.5.1 applied to the thermal model. Although the LNA should perform better in cold conditions, extremely low temperatures can lead to condensation in humid environments which can be detrimental to electronics. This analysis can provide more insight on the level of precautions necessary with expected temperatures to avoid such situations. Another concern of condensation is the signal attenuation from the thin film of water that could potentially form on the surface.

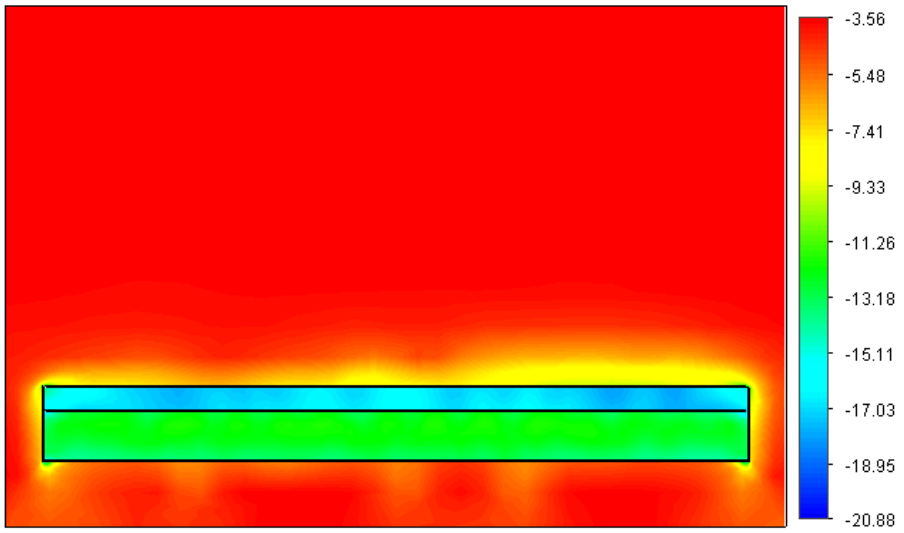

FIGURE 5.11: *The air temperature of the enclosed DDA on the cold day at 04:00.*

A contour plot at the center of the array is shown in Figure 5.11 during the coldest time of the day at 04:00. As with the hot day enclosure analysis, the DDA is given a symmetry boundary condition partially trapping the air inside the array. With the cover it can be seen that the night radiative cooling impact on the array is mitigated and the LNA does not suffer as much of a temperature drop when compared to the isolated DDA. A better representation of the results is shown in the variation of the internal and ground air temperatures over the cold day in Figure 5.12.

In a cold environment the heat dissipation of the LNA actually assists with temperature stability as this slows the rate of cooling from the sky temperature at night. At 06:00 when the sun starts to rise the internal air begins to heat up but this is at a slow rate as only natural convection is taking place and the cold air sinks to the ground plane. The ground air remains fairly stable throughout the course of the day, primarily influenced by the ambient temperature. A thermal image of the enclosure with the DDA is shown in Figure 5.13 at 04:00 where it can be seen that

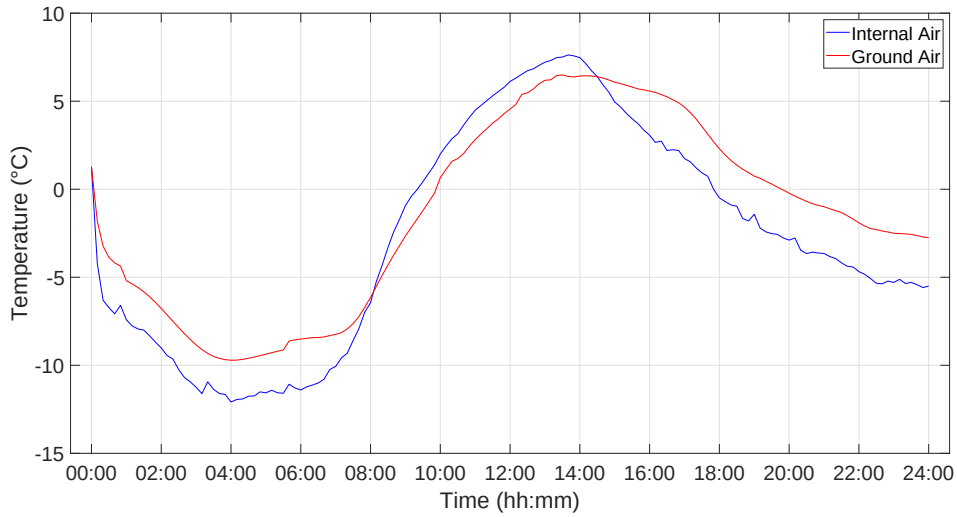

FIGURE 5.12: *Top plane, LNA and ground plane temperatures during the cold day.*

the cover reaches the coldest temperature of the system with -19.42°C.

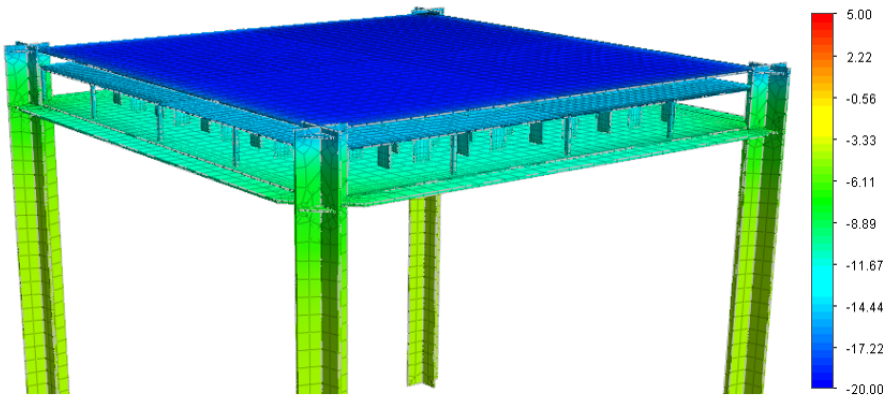

FIGURE 5.13: *The thermal image of the DDA during the cold day at 04:00.*

The minimum temperature of the cover is considered to be quite low but can be explained as at this time the ambient temperature is -3.77°C which translates into a -28.91°C sky temperature with the *Swinbank* formula. As a result of the sky temperature being so low, the down welling sky radiation determined from Equation 3.11 will have a minimal effect on the cover allowing the polypropylene to emit heat and as a result of its high emissivity only reaches equilibrium at -19°C. As mentioned earlier this may interfere with antenna performance as at this temperature condensation may take place resulting in water on the top plane. The effect of this may be reduced due to the hydrophobic properties of the polypropylene but it is still recommended to verify this and should be performed in future-work. The temperature variation of the cover, LNA and ground plane can be seen in Figure 5.14.

Here the LNA is safely within acceptable operating conditions and should benefit from the cold environmental temperatures. This should result in low receiver noise temperature and improved performance in the array. Although the LNA does experience a temperature change of 6.01°C/h when the sun begins to rise at 08:00. The change throughout the rest of the day remains below a 3 °C/h change per hour, which should assist with accuracy in the system. It should be said

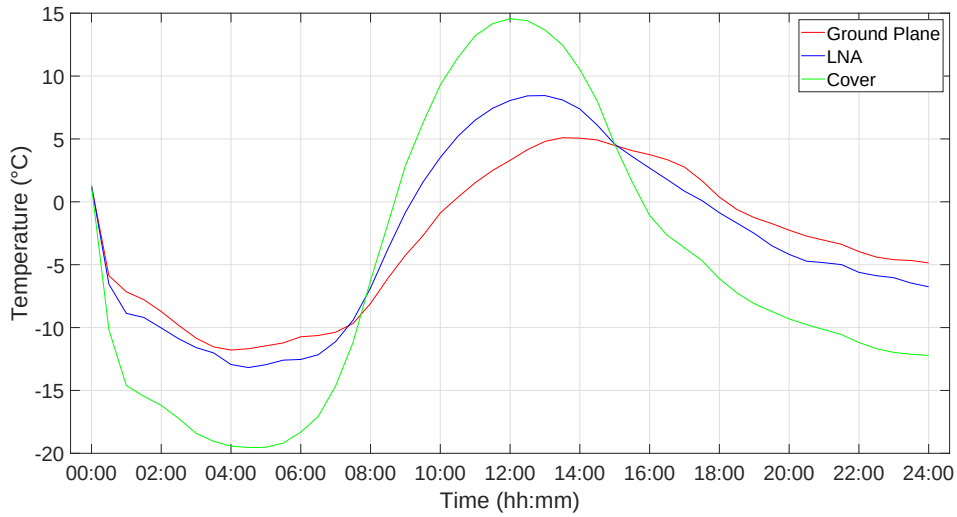

FIGURE 5.14: *Top plane, LNA and ground plane temperatures during the cold day.*

that the results presented are under extreme conditions and therefore the change in ambient temperature is higher than what would normally be experienced which is resulting in a high change in temperature for the LNA. Table 5.4 provides the temperatures at three hour intervals for the cover, LNA and ground plane over the course of the cold day.

	Temperature								
Time	00:00	03:00	06:00	09:00	12:00	15:00	18:00	21:00	00:00
Cover	1.28	-18.41	-18.32	2.88	14.56	4.57	-6.12	-10.16	-12.21
LNA	1.28	-11.59	-12.54	-0.84	8.06	4.58	-0.87	-4.84	-6.76
Ground Plane	1.28	-10.84	-10.73	-4.25	3.30	4.48	0.38	-3.05	-4.86

TABLE 5.4: *The temperature values (in °C) of the top plane, LNA and ground plane during the hot day.*

From the results of the cold day analysis for the enclosure, it can be seen that the LNA change in temperature greatly improved from the 9.4°C/h to 6.01°C/h. This is as a result of the lowered peak temperatures experienced and the LNA heat dissipation potentially reducing the rate of temperature change from the cold night sky.

5.4 Conclusion

This chapter was devoted to developing a suitable thermal solution that will improve the thermal conditions of the DDA such that it can operate effectively and below the maximum required temperature. Design goals were established on what the enclosure would need to achieve and were followed to develop an initial design concept. An open enclosure was favoured on account of the DDA having open sides and was found to benefit from the natural cooling and ventilation of wind. An important factor considered during development was the possible impact on the antenna performance of the DDA. Three materials were evaluated for the cover on account of their thermal and dielectric properties. All three materials achieved similar resulting temperatures and the polypropylene was therefore chosen due to its low dielectric properties. The distance between the top plane of the DDA and cover was optimised in a parametric study to ensure the

entire DDA would remain below 50°C in the worst conditions; as this would also assist with the lifetime of the components. Finally the hot and cold day simulations were performed on the enclosure to determine the resulting temperature profiles. Here it was found that the enclosure adequately improved the operating conditions of the DDA to the point where it can operate effectively within the specified limits. Both analysis cases experienced the worst temperature change at sunrise and for this reason it is recommended to recalibrate the system at this time to retain accuracy.

CHAPTER 6

Effect on Electromagnetics

Contents

Positioning a cover over the antenna can induce several effects that could possibly lead to the impairment of system performance. This chapter is dedicated to evaluating these effects through simulation to determine the resulting impacts. The chapter opens in §6.1 with the effect on the active reflection coefficient by analysing a central and corner element of the array. §6.2 follows with a comparison with and without the enclosure on the gain of the array at different frequency points. The effect of the support beams are considered in §6.3 followed by a discussion on the effect of the thermal solution on antenna performance in §6.4. The Chapter closes in §6.5 with a summary of the overall performance impacts.

As mentioned in the §5.2.1 introducing an additional medium for which the waves of the array will have to propagate through will induce some losses on account of reflections at the boundary layer and some dissipation within the substance. The dielectric properties that directly relate to these losses are the dielectric constant and the loss tangent. Polypropylene has been chosen as the cover material of the enclosure as it has been found to provide suitable protection for the array from the harsh climate of the Karoo and is a good dielectric material. The primary goal of creating an enclosure is to improve thermal management of the array to the point where the noise temperature will remain below acceptable limits and the array will operate effectively. This becomes redundant if by introducing an enclosure significantly impairs the sensitivity of the array. The following performance results are evaluated to gain insight on whether the designed enclosure has the potential to make a suitable thermal solution.

6.1 Antenna Bandwidth

The performance metrics of the DDA are gathered from a *FEKO* simulation [5], [21], that utilises an infinite substrate and ground plane approximation. These are coupled with an additional infinite layer that represents the cover and is placed over the array with the appropriate dimensions and dielectric properties. The simulation is run to gather the S-parameters and far field

patterns with and without the cover for comparison. The *FEKO* model and its three infinite planes that represent the ground plane, top plane and cover can be seen in Figure 6.1.

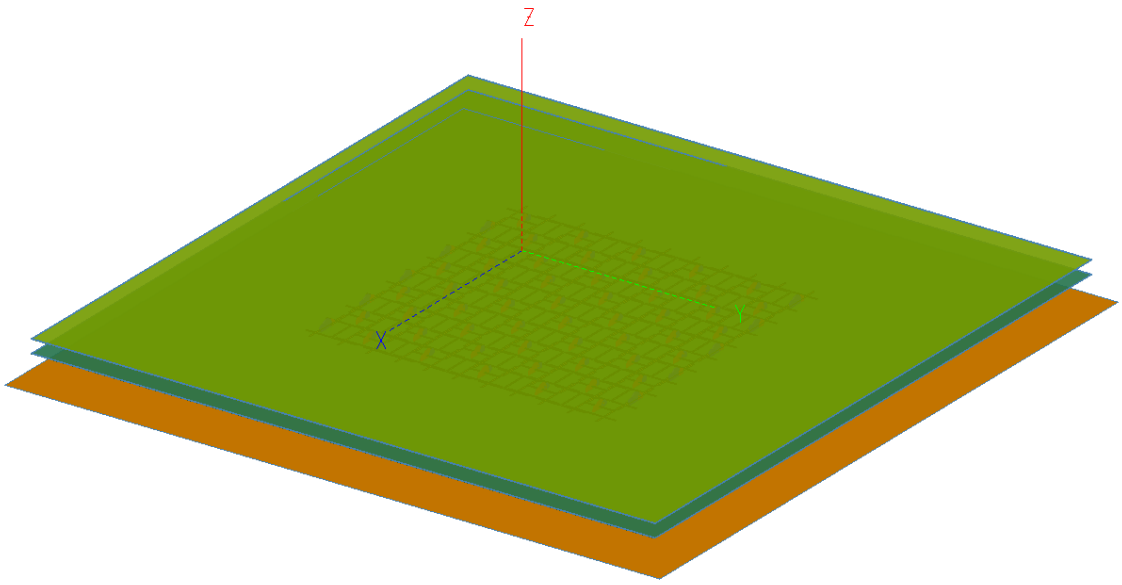

FIGURE 6.1: *FEKO model of the DDA with the cover.*

On account of the array structure of the DDA, the single-ended S-parameters must first be converted to mixed-mode parameters. This is done with the S-parameters matrix, whereby the differential ports denoted by m and n each consist of two single-ended ports p and q and is given by [5], [21]:

$$S_{MM} = \begin{bmatrix} S_{diff\ diff} & S_{diff\ comm} \\ S_{comm\ diff} & S_{comm\ comm} \end{bmatrix}$$

and the values pertaining to each submatrix can be determined as follows:

$$S_{diff\ diff,mn} = \frac{S_{pp,mn} - S_{pq,mn} - S_{qp,mn} + S_{qq,mn}}{2} \tag{6.1}$$

$$S_{diff\ comm,mn} = \frac{S_{pp,mn} + S_{pq,mn} - S_{qp,mn} - S_{qq,mn}}{2} \tag{6.2}$$

$$S_{comm\ diff,mn} = \frac{S_{pp,mn} - S_{pq,mn} + S_{qp,mn} - S_{qq,mn}}{2} \tag{6.3}$$

$$S_{comm\ comm,mn} = \frac{S_{pp,mn} + S_{pq,mn} + S_{qp,mn} + S_{qq,mn}}{2} \tag{6.4}$$

To evaluate the insertion loss introduced by the cover, the mixed-mode active reflection coefficient Γ_m is calculated from the above mentioned mixed-mode S-parameters of the differential mode in a specific scan direction for each antenna element as follows:

$$\Gamma_{dd,m}(\theta_0, \phi_0) = \sum_{n=1}^{N} S_{diff\ diff,mn} e^{-jk(x_n \sin\theta_0 \cos\phi_0 + y_n \sin\theta_0 \cos\phi_0)} \tag{6.5}$$

This is done for a central and corner element in the array at broadside and are shown in Figures 6.2 & 6.3 respectively. From each figure it can be seen that there is a deviation in the results between the isolated DDA and covered DDA. Although, when considering the mid-frequency band, the cover does not appear to heavily degrade the performance of the DDA but rather provides some stabilisation. This is especially seen with the corner element where the change in the active reflection coefficient in the mid-frequency range is seen to remain close to within 5 dB. When considering the $\Gamma < 10$ dB bandwidth, the covered DDA does experience some losses close to the end of the mid-frequency spectrum most likely due to impedance mismatch between the cover and array [64]. Therefore with further optimisation through impedance matching the enclosure could potentially not only be beneficial from a thermal perspective but also in performance.

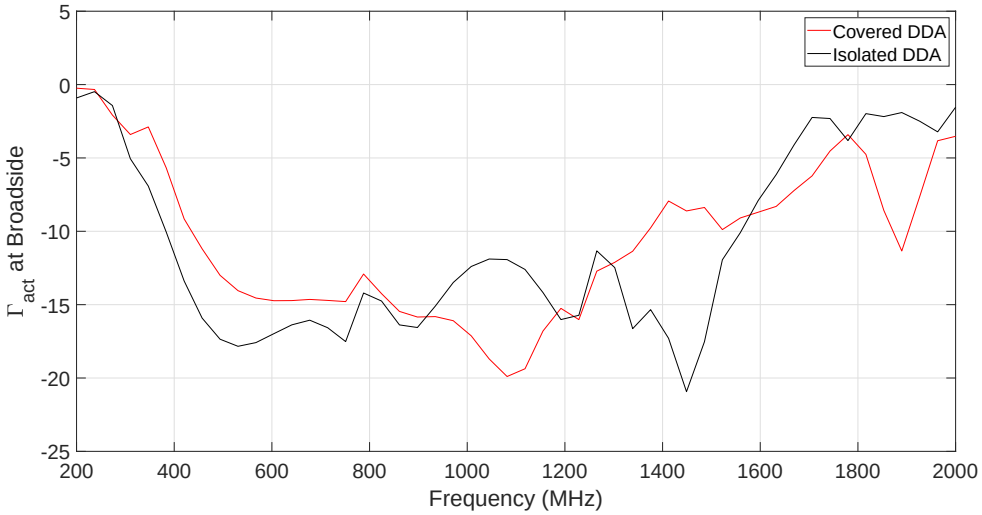

FIGURE 6.2: *Active reflection coefficient of the DDA with and without the cover for a central element at broadside.*

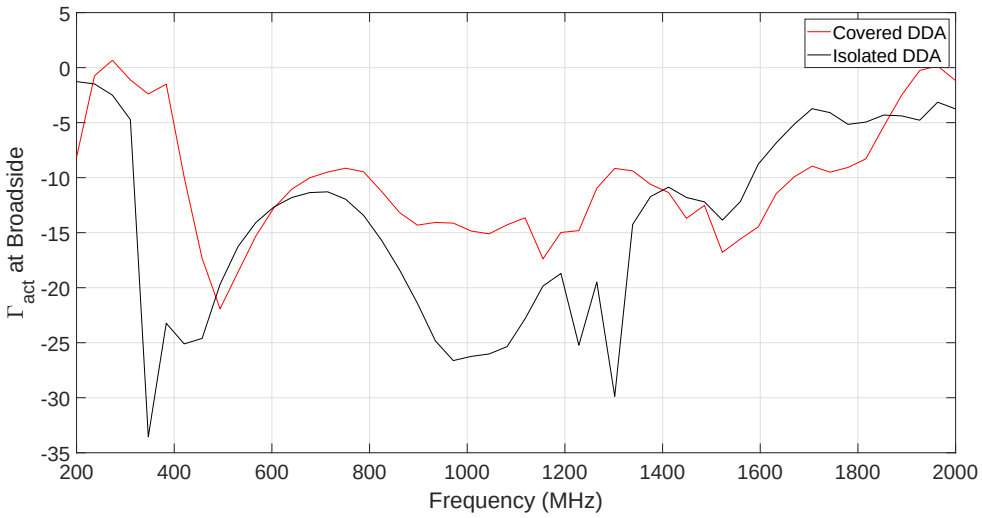

FIGURE 6.3: *Active reflection coefficient of the DDA with and without the cover for a corner element at broadside.*

The same analysis is performed at a 45° scan angle for further evaluation of antenna performance

with the cover. These active reflection coefficients of the same corner and central elements were plotted with the use of Equation 6.5 and are shown in Figures 6.2 & 6.3. Here it can be seen that the DDA itself experiences more loss although when comparing the isolated to the covered DDA results; apart from some spikes introduced by the cover it follows a very similar path of that of the isolated DDA across the necessary frequency band. It can also be seen that the cover still provides some stabilization to the loss experienced by the DDA, supporting the statement made in the analysis of the results at broadside.

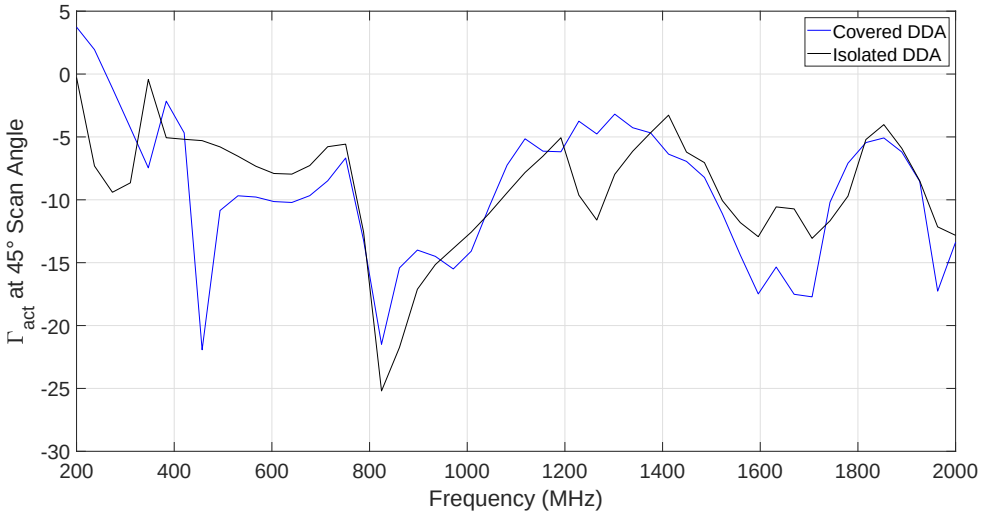

FIGURE 6.4: *Active reflection coefficient of the DDA with and without the cover for a central element at a 45°scan angle.*

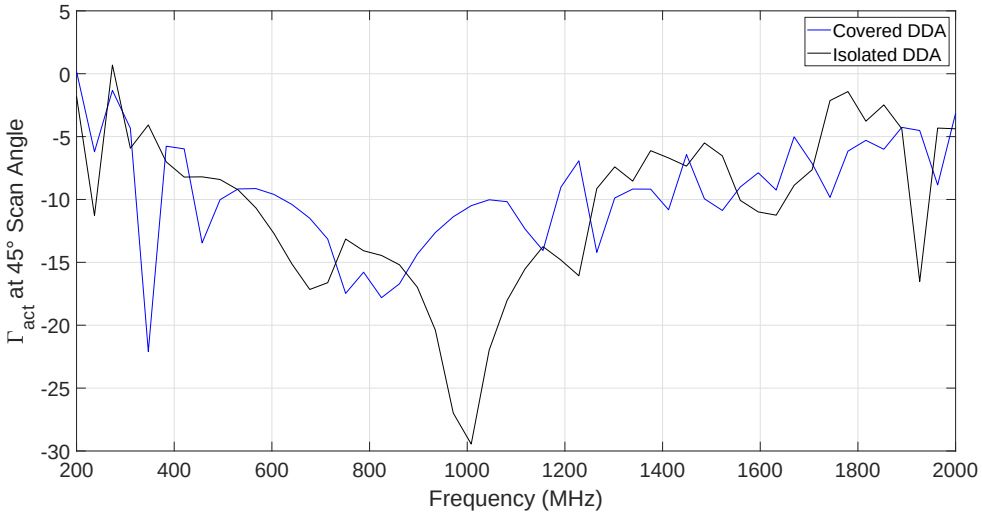

FIGURE 6.5: *Active reflection coefficient of the DDA with and without the cover for a corner element at a 45°scan angle.*

6.2 Antenna Gain

The gain patterns of the DDA were simulated with and without the cover to determine what deviations the enclosure may cause. This is done with the normalised co-polar gain patterns along the E-plane across three different frequencies. Figure 6.6 shows the 500 Mhz comparison where it can be seen that there is a very small deviation between the two patterns. The same can be said for the 1 & 1.5 Ghz gain patterns in Figures 6.7 & 6.8 respectively. When analysing the 1 Ghz band it can be seen that the covered DDA actually performs slightly better at the center frequency with a stronger gain potentially due to the cover assisting with focusing the antenna. There is slightly more deviation at the high frequency end in the side lobes but overall the gain remains fairly unaffected by the cover.

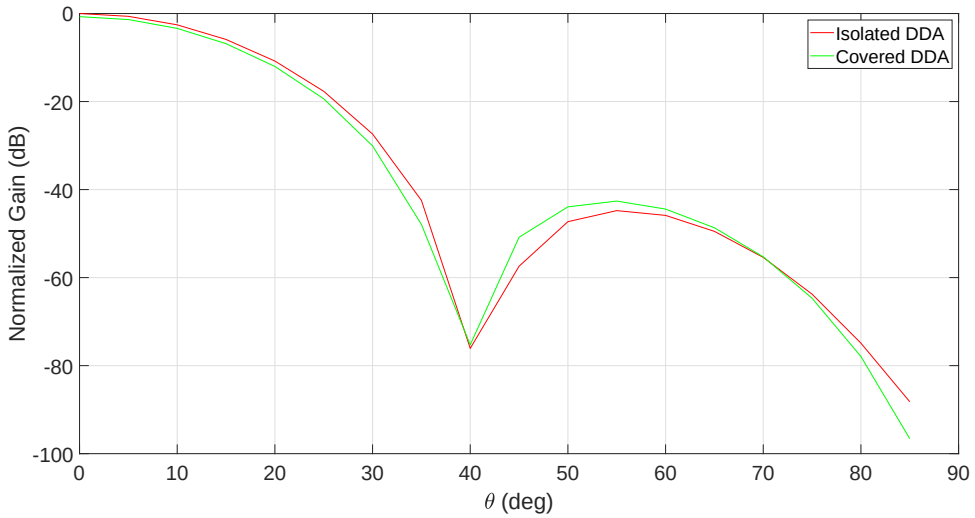

FIGURE 6.6: *Normalised co-polar gain patterns along the E-plane of the DDA with and without the cover at 500 Mhz.*

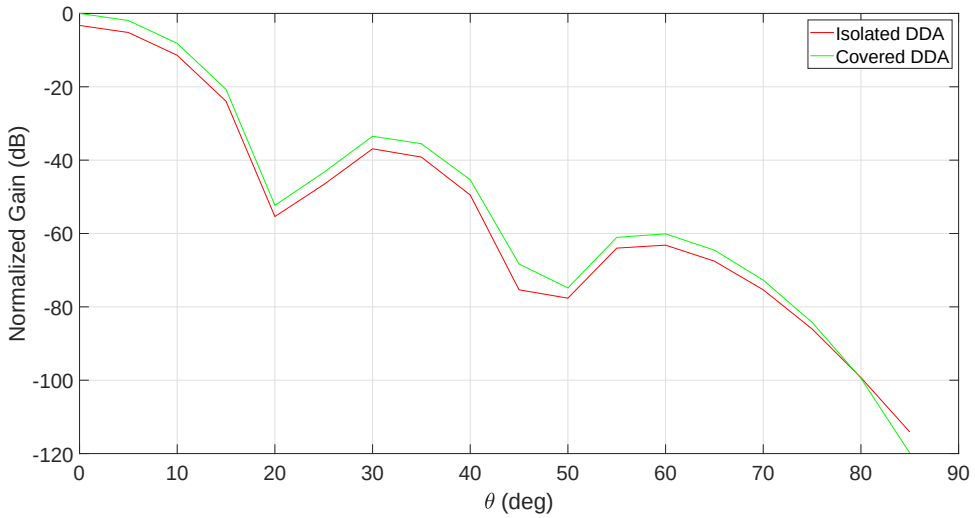

FIGURE 6.7: *Normalised co-polar gain patterns along the E-plane of the DDA with and without the cover at 1 Ghz.*

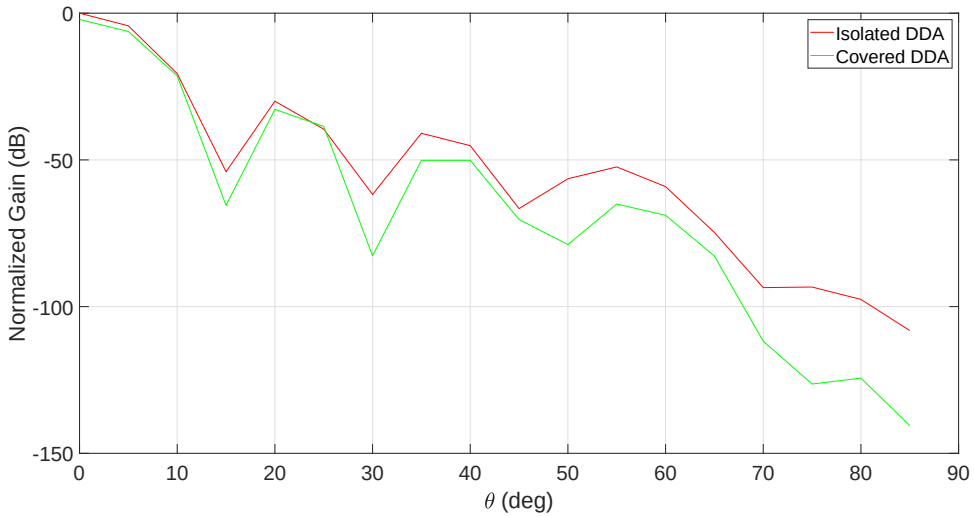

FIGURE 6.8: *Normalised co-polar gain patterns along the E-plane of the DDA with and without the cover at 1.5 Ghz.*

6.3 Impact of Support Beams

The support beams will not cause loss in the system, although it is possible that they could rather introduce undesirable radiation properties through mutual coupling that might result in scan blindness, impedance mismatch or a rapid loss of gain at certain frequencies. To analyse this, the same simulations are run with the CAD modelled support beams between the infinite layers at the appropriate locations. The gain results showed no difference in performance and the active reflection coefficient had very small deviations with no effect and is shown in Figure 6.9.

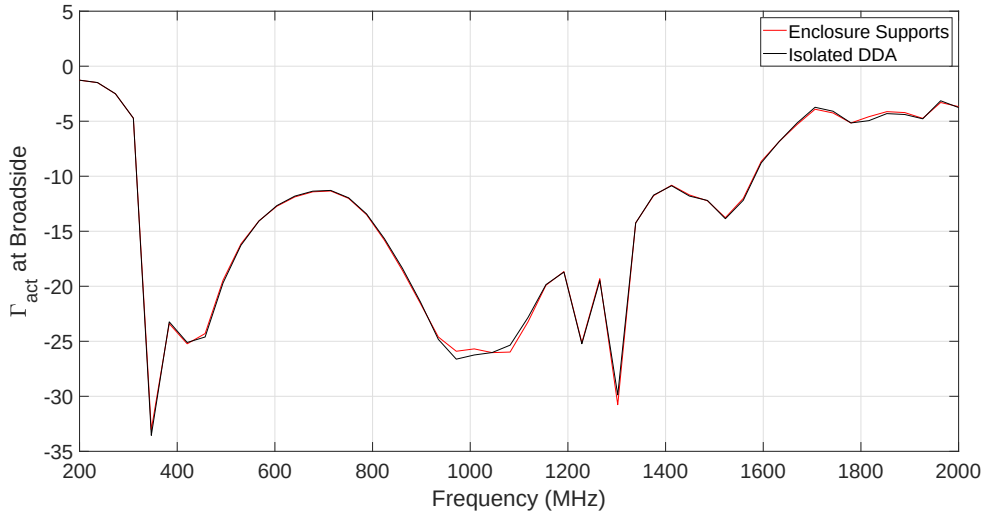

FIGURE 6.9: *Active reflection coefficient of the DDA with and without the supports for a corner element at broadside.*

6.4 Effect of the Thermal Solution on Antenna Performance

A thermal solution has been proposed in an attempt to enable the array to achieve desired operation with better thermal management, while taking into account the potential impairment on antenna performance. This has a large impact on antenna sensitivity as the thermal condition of the array influences the system noise temperature. This is better explained in Equation 6.6 where it can be seen that the system noise temperature is dependent on three main factors shown below.

$$T_{sys} = \eta_{rad} T_{ext} + (1 - \eta_{rad})\, T_p + T_{min}/\eta_n \tag{6.6}$$

These include the external noise temperature, the physical temperature of the antenna and lastly the receiver noise temperature. The intensity of each also vary depending on the noise source itself and their combined efficiency factor. The external noise temperature is comprised of extrinsic noise sources such as those encountered in the atmosphere and due to spillover. Although as explained previously, in this frequency range its contribution towards the total system noise temperature is minimal compared to the other factors and this is further emphasized with the radiation efficiency factor. As when this is low, the noise introduced from the physical temperature of the antenna will have a larger impact and for this reason, the thermal condition of the array becomes a great concern. The receiver noise is primarily dependent on the minimal achievable noise introduced by the receiver and varies depending on the noise matching efficiency as follows.

$$T_{rec} = \frac{T_{min}}{\eta_n} \tag{6.7}$$

This efficiency factor is dependent on how well the receivers and array element ports are ideally matched for optimal performance such that the LNA source reflection coefficient parameter is equivalent to the active reflection coefficient at the corresponding array element. The thermal solution can both improve and worsen this noise factor as with a decreased LNA temperature, the minimal noise temperature attained by the receiver will decrease but consequently by introducing a cover will impair the efficiency factor. Thus, it is imperative that the thermal solution is considered during the development of the DDA to achieve the best possible efficiency. A thermal solution is however necessary and with the appropriate impedance matching of the cover the resulting receiver noise temperature will improve. Therefore, with the thermal solution reducing the operating temperature experienced by the array, the noise introduced by both T_p & T_{rec} will be reduced improving sensitivity and thus the overall performance.

6.5 Conclusions

From an electrical standpoint, the main concern of the enclosure is the contribution of insertion losses as in a system such as the MFAA, the SKA is required to achieve a specified sensitivity and this is directly influenced by the loss introduced by the cover. This chapter provides insight on what kind of performance changes can be experienced when covering the DDA to ultimately determine if the designed enclosure will potentially serve as an acceptable thermal solution. The active reflection coefficient and gain patterns with and without the cover were analysed and discussed, after which it was concluded that the cover does result in some losses but actually improves stability. Therefore with further optimisation in impedance matching of the final

design of the DDA, a suitable protective enclosure can be achieved with foreseeable stabilisation in performance.

CHAPTER 7

Conclusion

Contents

7.1 Thesis Summary

A thermal analysis of the DDA is essential to ensuring the required performance standards can be met when operating in the climate of the Karoo. It was discussed in Chapter 2 than an increase in temperature would lead to an increase in receiver noise temperature, which would consequently result in a loss of sensitivity. The LNA operating conditions were identified as the main consideration for the analysis as it is the most important subsystem from a noise perspective. This was followed by the influence of temperature on calibration and the possible stresses that may result in the components of the DDA when in the Karoo.

The development procedure of the thermal simulation and the various heat transfer processes that will occur on the DDA are provided in Chapter 3. Here a finite element model was created to simulate the heat transfer experienced by the DDA when exposed to a specified environment. This model utilises CFD to model the heat transfer through the air as well as the radiation of the components. Only natural convection and clear skies are considered as these represent the worst case environmental conditions potentially experienced by the DDA. With the model developed, the accuracy was validated through a comparison with measured results and was found to be acceptable.

Chapter 4 begins the thermal analysis of the DDA with first specifying the necessary requirement that the LNA remains below 50 °C. The temperature change per hour is also identified as an important parameter as this will influence calibration as well as thermal stresses experienced by the DDA. The LNA is considered to dissipate heat and is applied to the model in the recommended placement on the feedboard. Two extreme day conditions are created from data obtained from measurements at the SKA site. These are applied to the DDA to determine the temperature variation over the course of the two days. Here it is found that the LNA reaches a maximum temperature of 58.53°C and therefore requires a thermal solution.

An enclosure design is proposed in Chapter 5 to improve the thermal conditions of the DDA such that it can operate effectively and below the maximum required temperature. Here it was

decided that an open enclosure would be beneficial to the DDA design as this will allow wind to flow through the array and provide natural cooling. An important factor considered during development was the possible impact of the enclosure on the antenna performance of the DDA. Polypropylene was chosen as the suitable material as it would provide adequate environmental protection with minimal impact on performance. The design was optimised to ensure the entire DDA will remain below 50 °C with a parametric study. Finally this was tested by simulating the enclosure under the same extreme conditions of the Karoo to analyse the potential thermal improvement. The LNA temperature was found to improve by 13.39°C and was reduced to within acceptable operating conditions.

The effect of the enclosure on the DDA was tested in Chapter 6 with a *FEKO* simulation, by comparing the active reflection coefficient and gain patterns with and without the cover. Here it was found that the cover did introduce some loss into the system but could potentially be beneficial with further impedance matching.

In conclusion, this project provided a thermal analysis of a Dense Dipole Array for the SKA Mid-Frequency Aperture Array. The temperature distribution of the DDA was determined in the extreme conditions of the Karoo and evaluated against performance metrics. A thermal solution was found to be necessary and an enclosure was developed and tested through simulation for this purpose. The enclosure was found to provide suitable protection for the DDA while considering the consequential effects on the electromagnetic performance. With further optimisation of impedance matching, the enclosure will enable the DDA to achieve desired performance in the Karoo.

7.2 Contribution

The following work from Chapters 3, 4, 5 & 6 lead to the primary contribution of a suitable thermal solution for the DDA such that it can operate effectively in the Karoo.

I A finite element model was developed and tested capable of accurately modelling the DDA under specified climate conditions.

II The temperature distribution of the DDA under the most extreme plausible conditions of the Karoo were determined. The resulting temperatures were analysed and found to exceed acceptable operating conditions.

III A proposed thermal solution was designed in the form of an enclosure based on certain requirements with the purpose of enabling the DDA to operate effectively in the Karoo.

IV The effect of wind on the DDA was assessed and an open enclosure was favoured to benefit from the natural cooling component.

V Possible cover materials were evaluated on their ability to provide adequate thermal protection without degrading antenna performance.

VI The enclosure was optimised such that the DDA will remain below the maximum temperature of 50°C to ensure acceptable operation and lifetime of the components.

VII The temperature distribution of the enclosed DDA under the extreme conditions of the Karoo were determined and the resulting temperatures were found to maintain the DDA below temperature limits and improve temperature stability for calibration.

VIII The effect of the cover and supports on the electromagnetic performance of the DDA were assessed and found to introduce some insertion losses but can potentially be mitigated with impedance matching.

7.3 Suggestions for Future Work

Enclosure Impedance Matching:
A key step in the development of an optimal enclosure that will need to be performed in future work involves tuning the DDA with the cover to obtain the best possible antenna performance. It was concluded in Chapter 6 that the cover could potentially stabilize antenna performance but requires impedance matching over the mid-frequency range to remove unwanted losses in the system [64], [67].

Optimising for Mass Production and Assembly:
As the enclosure design serves as a framework for what is required to improve the thermal conditions of the DDA to acceptable standards. Further design optimisations can be performed for mass production and assembly to accompany the thousands of arrays to be deployed.

Weather Proofing:
The semi-desert region of the Karoo will expose the array and enclosure to many environmental aspects such as dust, rain and wildlife. Possible future work could involve analysing the affects these could have on antenna performance and decreased lifetimes to determine the precautions necessary for avoidance.

Calibration Period:
One of the parameters evaluated during the thermal analysis was temperature stability as it was found that this could influence calibration and subsequently the period between calibrations. It would be beneficial to know the exact temperature change that would result in the deterioration of signal quality of the DDA to determine when the system would need to be recalibrated.

References

[1] (Aug. 2018). The ska project, [Online]. Available: https://www.skatelescope.org/the-ska-project/ (visited on 2018).

[2] D. Campbell and F. Lo, "The Square Kilometre Array," 2009. [Online]. Available: http://usskac.astro.cornell.edu/members/.

[3] (Aug. 2018). Location, [Online]. Available: https://www.ska.ac.za/about/location/ (visited on 2018).

[4] P. Hall, R. Schilizzi, P. Dewdney, and T. Lazio, "The Square Kilometer Array (SKA) Radio Telescope : Progress and Technical Directions," *Radio Science Bulletin*, 2008. [Online]. Available: http://www.skatelescope.org/publications/.

[5] J. Gilmore, "Design of a Dual-Polarized Dense Dipole Array for the SKA Mid-Frequency Aperture Array by," PhD thesis, Stellenbosch University, 2016.

[6] R. D. Ekers, A. J. Faulkner, P. J. Hall, J. L. Jonas, and K. I. Kellermann, "Memo 100 Preliminary Specifications for the Square Kilometre Array," 2007.

[7] M. Ruiter, W. Van Cappellen, E. Van Der Wal, M. Arts, R. Van Den Brink, and K. Visser, "Development of a Vivaldi Tile for the SKA Mid Frequency Aperture Array," *2016 10th European Conference on Antennas and Propagation, EuCAP 2016*, 2016. DOI: 10.1109/EuCAP.2016.7481742.

[8] J. G. Bij De Vaate, P. Benthem, R. Witvers, R. Van Den Brink, Y. Zhang, and S. A. Torchinsky, "Mid Frequency Aperture Array Technology Developments for the SKA," *Proceedings - ANTEM 2014: 2014 16th International Symposium on Antenna Technology and Applied Electromagnetics*, 2014.

[9] E. E. M. Woestenburg, L. Bakker, and M. V. Ivashina, "Experimental Results for the Sensitivity of a Low Noise Aperture Array Tile for the SKA," 2011. [Online]. Available: http://inspirehep.net/record/925657/files/arXiv%7B%5C%7D3A1108.5433.pdf.

[10] M. A. Garrett, "Radio Astronomy Transformed: Aperture arrays - Past, Present and Future," *IEEE AFRICON Conference*, Jun. 2013. [Online]. Available: https://arxiv.org/ftp/arxiv/papers/1211/1211.6455.pdf.

[11] J. G. De Vaate, S. A. Torchinsky, A. J. Faulkner, Y. Zhang, A. Gunst, P. Benthem, I. M. Van Bemmel, and G. Kenfack, "SKA Mid Frequency Aperture Arrays: Technology for the Ultimate Survey Machine," *2014 31th URSI General Assembly and Scientific Symposium, URSI GASS 2014*, 2014.

[12] S. J. Wijnholds and R. Jongerius, "Computing cost of sensitivity and survey speed for aperture array and phased array feed systems," *IEEE AFRICON Conference*, 2013.

[13] B. A. V. Ardenne, J. D. Bregman, W. A. V. Cappellen, G. W. Kant, J. Geralt, and B. D. Vaate, "Extending the Field of View With Phased Array Techniques : Results of European SKA Research," 2009.

[14] S. A. Torchinsky, A. O. H. Olofsson, B. Censier, A. Karastergiou, M. Serylak, P. Picard, P. Renaud, and C. Taffoureau, "Characterization of a dense aperture array for radio astronomy," 2016. [Online]. Available: http://arxiv.org/abs/1602.07976%7B%5C%%7D0Ahttp://dx.doi.org/10.1051/0004-6361/201526706.

[15] A. J. Faulkner, "Dense aperture arrays for the Square Kilometre Array," *2011 30th URSI General Assembly and Scientific Symposium, URSIGASS 2011*, 2011.

[16] I. M. van Bemmel, A. van Ardenne, J. G. bij de Vaate, A. J. Faulkner, and R. Morganti, "Mid-frequency Aperture Arrays: the Future of Radio Astronomy," *Resolving the Sky Radio Interferometry Past Present and Future RTS2012*, 2012. [Online]. Available: http://arxiv.org/abs/1208.6180.

[17] R. Braun and W. van Cappellen, "Aperture Arrays for the SKA: Dense or Sparse?," 2006. eprint: 0611160. [Online]. Available: http://arxiv.org/abs/astro-ph/0611160.

[18] M. Huynh, *An Overview of the Square Kilometre Array*.

[19] Y. Zhang and A. K. Brown, "Octagonal Ring Antenna for a Compact Dual-Polarized Aperture Array," *IEEE Transactions on Antennas and Propagation*, 2011.

[20] I. Tzanidis, J. P. Doane, K. Sertel, and J. L. Volakis, "Wheeler's current sheet concept and Munk's wideband arrays," *IEEE Antennas and Propagation Society, AP-S International Symposium (Digest)*, pp. 1–2, 2012.

[21] N. Wilke, "Quantization Effects in Beamforming in Dense Phased Arrays," no. December, 2017.

[22] F. P. Incropera, D. P. DeWitt, T. L. Bergman, and A. S. Lavine, *Fundamentals of Heat and Mass Transfer*, 6th ed. John Wiley & Sons, 2007.

[23] A. Zaidi, S. Rawal, and H. Abichandani, *Heat and Mass Transfer : Mechanical Engineering Handbook*, 2nd ed. Boca Raton: CRC Press LLC, 1999. [Online]. Available: http://k204.ru/books/English/Ch04.pdf.

[24] Y. A. Cengel and A. J. Ghajar, *Heat and Mass Transfer: Fundamentals and Applications*, 5th ed. Penn Plaza, New York, NY: McGraw-Hill Education, 2015.

[25] *midas NFX - Powerful, Fast and Affordable FEA Software for Mechanical Engineering*. [Online]. Available: http://www.midasnfx.com/.

[26] E. L. Gouri Dhatt, Gilbert Touzot, *Finite Element Method*, P. Breitkopf, Ed. Wiley, 2017.

[27] S. Nategh, "Thermal Analysis and Management of High-Performance Electrical Machines," PhD thesis, KTH School of Electrical Engineering, 2013. [Online]. Available: http://www.diva-portal.org/smash/record.jsf?pid=diva2:623376.

[28] Y. Chin, E. Nordlund, and D. Staton, "Thermal Analysis - Lumped-Circuit Model and Finite Element Analysis," *Sixth International Power Engineering Conference (IPEC)*, 2003. [Online]. Available: https://www.motor-design.com/wp-content/uploads/2016/12/ipec%7B%5C_%7D2003%7B%5C_%7Dtheraml%7B%5C_%7Dmodel.pdf.

[29] A. Bimana, "Wideband Low Noise Amplifier for Highly Sensitive SKA Receivers," Mar. 2018. [Online]. Available: https://repository.up.ac.za/bitstream/handle/2263/66212/Bimana%7B%5C_%7DWideband%7B%5C_%7D2018.pdf?sequence=1%7B%5C&%7DisAllowed=y.

[30] D. A. Botes, "Wideband, Low-Noise Amplifiers for the Mid-Range SKA," PhD thesis, Stellenbosch University, 2015.

[31] L. W. Couch, *Digital and Analog Communication Systems*, 8th ed. New Jersey, USA: Pearson, 2012. [Online]. Available: http://quality.hau.gr/pages/contact.htm.

[32] P. S. V. Hum, "Radio and Microwave Wireless Systems," 2017. [Online]. Available: http://www.waves.utoronto.ca/prof/svhum/ece422/notes/21-noise.pdf.

[33] H. Nyquist, "Thermal Agiation of Electric Charge in Conductors," *Physical Review*, 1928. [Online]. Available: http://123.physics.ucdavis.edu/johnson%7B%5C_%7Dfiles/nyquist%7B%5C_%7D1928.pdf.

[34] G. Vasilescu, *Electronic Noise and Interfering Signals*. Springer, 2017.

[35] D. Pozar, *Microwave Engineering*, 4th ed. John Wiley & Sons, Inc, 2005. [Online]. Available: http://scholar.google.com/scholar?hl=en%7B%5C&%7DbtnG=Search%7B%5C&%7Dq=intitle:No+Title%7B%5C#%7D0.

[36] D. Leeson, "Antenna and Receiver Noise," 2002.

[37] Keysight Technologies, "Fundamentals of RF and Microwave Noise Figure Measurements," *Application Note*, 2010.

[38] J. D. Pubsec, "The Influence of Temperature on Lifetime," 2013.

[39] P. Kruger, B. Visser, and D. Prinsloo, "Fully integrated LNA & Antenna for Ultra-Low Noise Figure Receivers," *European Microwave Week 2017: "A Prime Year for a Prime Event", EuMW 2017 - Conference Proceedings; 47th European Microwave Conference, EuMC 2017*, pp. 58–61, 2017.

[40] A. Bimana and S. Sinha, "Impact of SiGe HBT Parameters to the Performance of LNAs for Highly Sensitive SKA Receivers," *Proceedings of 23rd International Conference, RADIOELEKTRONIKA 2013*, 2013.

[41] M. Panahi, "LNA Considerations for Square Kilometre Array," 2012.

[42] S. J. Wijnholds, "Calibration of Mid-Frequency Aperture Array Stations Using Self-Holography," *Proceedings of the 2017 19th International Conference on Electromagnetics in Advanced Applications, ICEAA 2017*, 2017.

[43] A. C. Olivieri and G. M. Escandar, "Overview of SKA Calibration Challenges and Impact of Design Decisions," 2014. [Online]. Available: http://linkinghub.elsevier.com/retrieve/pii/B9780124104082000016.

[44] R. P. Armstrong, J. Hickish, K. Z. Adami, and M. E. Jones, "Polarisation Performance and Calibration of the Digital Beamforming System for 2-PAD," 2010.

[45] R. Bansal, *Strength of Materials*, 4th ed. Boston, USA: Laxmi Publications (P) LTD, 2009.

[46] Comsol, *Thermal Expansion and Thermal Stresses*, 2014. [Online]. Available: https://www.comsol.com/multiphysics/thermal-expansion-and-thermal-stresses.

[47] J. M. Gere, *Mechanics of Materials*, 6th ed. Thomas Learning, Inc., 2004.

[48] H. Nowak, "The Sky Temperature In Net Radiant Heat Loss Calculations From Low-Sloped Roofs," *Infrared Physics*, vol. 29, no. 2-4, pp. 231–232, 1989, ISSN: 00200891. DOI: 10.1016/0020-0891(89)90055-9.

[49] M. Luciuk, "Night Radiative Cooling, The Effect of Clouds and Relative Humidity," *Amateur Astronomers, Inc.*, 2013. [Online]. Available: http://www.asterism2.org/tutorials/tut37%20Radiative%20Cooling.pdf.

[50] *Thermistors AVX NJ28*. [Online]. Available: https://docs-emea.rs-online.com/webdocs/13ec/0900766b813ece34.pdf.

[51] A. Gunst, "AA Concept Descriptions," *WP-2-010.020.010-TD-001*, 2011.

[52] B. Woestenburg and B. Woestenburg, "Memo 98 Definition of Array Receiver Gain and Noise Temperature,"

[53] R. T. Schilizzi, P. E. F. Dewdney, and T. J. W. Lazio, "The Square Kilometre Array," *Proceedings of the IEEE*, 2008. [Online]. Available: http://proceedings.spiedigitallibrary.org/proceeding.aspx?doi=10.1117/12.786780.

[54] K. F. Warnick, M. V. Ivashina, R. Maaskant, and B. Woestenburg, "Unified Definitions of Efficiencies and System Noise Temperature for Receiving Antenna Arrays," *IEEE Transactions on Antennas and Propagation*, vol. 58, no. 6, pp. 2121–2125, 2010.

[55] P. Benthem, "MFAA Array Prototypes," no. April, 2014.

[56] M. Leathard, "SKA Mid-Frequency Antenna Array Thermal Analysis Phase 2 Report," *Thermal Analysis Phase 2 Report*, 2015.

[57] T. Otoshi, "Calculation of Antenna System Noise Temperatures at Different Ports — Revisited," *IPN Progress Report*, 2002.

[58] *Solar Radiation*. [Online]. Available: http://www.soda-pro.com/.

[59] *SKA Weather Data*. [Online]. Available: https://www.skatelescope.org/wp-content/uploads/2012/06/51%7B%5C_%7Dannexure-f-physicalcharacteristics.%7B%5C%%7D0Azip.

[60] M. Försth and A. Roos, "On the Importance of Spectrally Resolved Absorptivity Data in Fire Technology," *Fire Technology*, 2009.

[61] M. Sadiku, *Elements of Electromagnetics*, 5th ed. Oxford University Press, 2010.

[62] D. Satria, "Radome Analysis Techniques," no. August, 2016.

[63] E. Resource, *Antenna Radomes*. [Online]. Available: http://rfandwireless.com/antennas/radomes/.

[64] D. J. Kozakoff, *Analysis of Radome-Enclosed Antennas*, 2nd ed. Boston, London: Artech House, Inc, 2009.

[65] L. Griffiths, "A Fundamental and Technical Review of Radomes," *MPDigest*, 2008. [Online]. Available: http://www.onrampcomm.com/new/AdFiles/MFG%20Galileo%7B%5C_%7DMay08%20MPD.pdf.

[66] I. Anderson, "Measurements of 20-ghz transmission through a radome in rain," *Antennas and Propagation, IEEE Transactions*, vol. 23, pp. 619–622, Oct. 1975.

[67] J. Lienau, *Antenna Matching for Electronics Enclosures*. [Online]. Available: https://www.lsr.com/white-papers/antenna-matching-within-an-enclosure.